An Optofluidic Ring Resonator Platform for Rapid and Robust Sensing

Thesis by

Paula F. Popescu

In Partial Fulfillment of the Requirements

for the Degree of

Doctor of Philosophy

CALIFORNIA INSTITUTE OF TECHNOLOGY

Pasadena, California

2017

(Defended September 23, 2016)

Abstract

Ring resonators show great potential as sensitive optical detectors for studies of biomolecular interactions, drug screening, and point-of-care diagnostics. They are sensitive to minute changes in the refractive index of the surrounding medium, which enables them to detect and quantify sub-femtomolar concentrations of target molecules. This thesis investigates the advantages of an optofluidic ring resonator platform that employs a differential measurement scheme for reducing environmental noise due to temperature and pressure fluctuations. Through simulations and experiments, I determine the sensitivity of the platform to changes in the target analyte concentration and to environmental noise, and demonstrate the benefits of employing a second, reference, ring resonator.

A crucial step in achieving versatile biosensing platforms is the integration of the high sensitivity resonators into platforms with short assay times and robust chemical functionalization. I focus on the development of robust chemistry protocols for depositing linker silane layers for biomolecular interaction studies. Moreover, since the fluid handling scheme strongly influences the response time of the platform, I design and test two fluidic platforms integrated with elastomeric valves that show excellent response times. To further increase the response time of the sensing platform, I explore the effects of a patterned channel geometry on the enhancement of mass transport to the sensor in low Reynolds number flows.

Published Content and Contributions

D. Kim, P. Popescu, M. Harfouche, J. Sendowski, M.-E. Dimotsantou, R. C. Flagan, and A. Yariv, "On-chip integrated differential optical microring refractive index sensing platform based on a laminar flow scheme," *Opt. Lett.*, vol. 40, pp. 4106-4109, Sep 2015. doi:10.1364/OL.40.004106.

P. Popescu contributed by designing and fabricating the microfluidic chips, participated in the experimental setup, the preparation of the reagents and the collection and interpretation of data.

D. Kim, P. Popescu, M. Harfouche, J. Sendowski, M.-E. Dimotsantou, R. Flagan, and A. Yariv, "On-chip integrated differential optical microring biosensing platform based on a dual laminar flow scheme," *in CLEO: 2015*, p. STu4K.7, Optical Society of America, 2015. doi:10.1364/CLEO_SI.2015.STu4K.7.

P. Popescu contributed to the experimental setup and collection and interpretation of data.

To Brian

Acknowledgments

My graduate career at Caltech was a complex and formative journey, and I was fortunate to have the guidance and support of a number of people who have been instrumental in the successful completion of my project and degree.

First and foremost I want to thank my advisor, Prof. Richard Flagan, for his unwavering support and excellent mentorship. He was always available when I needed his input, and always eager to discuss and brainstorm ideas related to the project. He trusted me to take the project in the directions that I envisioned, but also guided me along the way. Under his supervision I have grown tremendously as a scientist and independent researcher. It's not an overstatement to say that I could not have asked for a better advisor and mentor.

Prof. Amnon Yariv, whom I consider my unofficial co-advisor, has been a great source of deep insights into optics, and has provided invaluable advice during my meetings with him. In addition, I have enjoyed the discussions during the group meeting lunch on many diverse topics including science, literature and linguistics.

Prof. Keith Schwab has been a mentor throughout my graduate career. I am very grateful for his support during difficult times in my career, which was crucial to my continued success.

I am grateful for the input and advice of Prof. Andrei Faraon during the committee meetings in the last years of my graduate life.

I would not have had the opportunity of working on this project without Prof. Scott Fraser's guidance. In addition, over the first few years of my graduate life, he has put me in contact with experts in the field, and provided many resources from his lab that helped me further my experiments.

I would also like to thank the Graduate Dean's Office, in particular Felicia Hunt, Natalie Gilmore, Doug Reese, and Joe Shepherd for their support and their help in navigating the intricacies of graduate life.

The work presented in this thesis is a continuation of the work began by Jacob Sendowski and Marilena Dimotsantou as part of a collaboration between the Flagan and Yariv groups, which joined optical and chemical expertise into an interdisciplinary project. Their work has been the foundation on which the current work is based. As part of the collaboration, I have worked closely with Dongwan Kim and Mark Harfouche, whose contributions and input have been vital to the success

of the project. I greatly value C.J. Yu's expertise in developing the coumarin chemistry protocols, and his input in the silane chemistry optimization.

I am grateful to the other members of the Flagan group, in particular to Johannes Leppa, Wilton Mui, Huajun Mai, Jill Craven, Natasha Hodas, and Mandy Grantz, who have been very friendly and created a wonderful work environment.

Thank you to Christy Jenstad, Connie Rodriguez and Eleonora Vorobieff for making life in the Applied Physics department run smoothly, and for being committed to student well-being.

Thank you to Andres Collazo for his help at the Beckman Imaging Center, and to Alireza Ghaffari for help using the microfluidics lab.

My life at Caltech would not have been the same without an amazing group of friends. Thank you to Ron Appel and Becky Calinsky for many fun times and pleasantries. The elbow house and its residents, Kevin Engel, Evan O'Connor, Milivoje Lukic, and Dan Betea, hold a special place in my heart. We have shared many fond memories and exciting adventures. Itamar Yaakov has been a caring and kind friend. I could always count on Vaclav Cvicek and Diana Negoescu for help and advice. Thank you to Mihai Florian for his encouraging words and generosity. I dearly cherish the friendship of Laura Book, Esfandiar Alizadeh, and Hesham Azizgolshani, who are very warm and big-hearted. Many thanks to Mhair Orchanian, Tim Morton, Vera Gluscevic, Tomasz Tyranowski, Bao Ha, Andrew Richards, Kari Hodge and Henry Kozachkov for the wonderful memories we have made during these years. I miss the orienteering trips I took with Malena and Augustin. Thank you Ayfer, Francisco and Kaloyan for not letting time and distance keep us apart.

I am deeply grateful to my parents, Sanda and Bob, for their unconditional love and selflessness, for always believing in me, for wanting what's best for me, and for making many sacrifices to see me succeed in my endeavors.

This thesis is dedicated to my fiance, Brian Willett, who has braved the distance for four years to be by my side, who has been very supportive and generous, and who has been my rock though the many challenges. I am grateful for your love every day.

Contents

List of Figures

List of Tables

Chapter 1

Introduction

Biosensors are versatile tools used for medical applications in clinical diagnostics, drug screening, and pathogen detection, as well as for fundamental science in studies of binding kinetics and epitope mapping. Affinity biosensors rely on the specific interaction between a biorecognition element such as an enzyme, antigen, or nucleic acid, and the analyte of interest. A signal transduction mechanism converts the biomolecular interaction into a readable and quantifiable signal. Depending on the nature of the transduction mechanism, most biosensors can be categorized as mechanical, electrical, or optical. This thesis presents the development of an optical ring resonator biosensor platform, an emergent optical biosensor technology, and explores designs and protocols for enabling it to simultaneously achieve low detection limits, fast assay times, and parallel sensing, a highly desirable combination of qualities for a biosensor. First we give a brief overview of biosensor platforms in general, and their biological applications, touching upon some of the advantages and drawbacks of each platform. We focus on optical biosensors, with emphasis on whispering gallery mode resonators. Detailed reviews on optical biosensors and microring resonators can be found in [1, 2, 3, 4, 5].

1.1 Overview of biosensing technologies

Biosensing technologies encompass a large number of distinctive platforms, each exploiting different properties of the analyte (mass, conductivity, index of refraction, light absorption), but they must be characterized and compared according to the same performance metrics. An ideal biosensing platform should possess the following characteristics: high sensitivity, low limit of detection, large dynamic range, high selectivity, multiplexing capabilities, ease of fluidic integration, portability, real-time detection, short response time, small reagent volume needed, low device-to-device variability, and low cost. Depending on the application, the relative importance and desirability of these metrics varies.

Biosensors that can measure minute concentrations of analytes in blood or serum, such as antibodies or cancer biomarkers, are highly desirable for early stage detection of diseases. For example, normal levels of the interleukin-6 antibody (IL-6) are at $6\,\mathrm{pg\,ml^{-1}}$ (300 fM); detecting an increase over that concentration could indicate the onset of squamous cell carcinoma of the head and neck (HNSCC) [6]. For accurate disease diagnosis, a biosensing device must include a multiplexed platform with an array of sensors, each selectively targeting a different analyte from complex media (blood, serum, or saliva). A highly selective array of sensors allows for monitoring of disease fingerprints, *i.e.*, simultaneous and quantifiable increases in a number of inflammatory or cancer biomarkers. Malhotra *et al.* argue that one must simultaneously monitor at least 5-10 disease biomarkers in order to obtain an accurate disease diagnosis [6]. Moreover, biosensors can be employed in single cell analysis by detecting cytosolic-level concentrations of cytokines from single cell lysis or cell secretion in microfluidic chambers. Arlett *et al.* give an overview of different biosensor technologies and their detection capabilities, and suggest the benchmark detection to be a concentration increase of $40\,\mathrm{fM\,min^{-1}}$, which is the secretion rate of tumor necrosis factor-α (TNF-α), a cancer biomarker, by monomyelectic cells [7]. The limit for biosensing is, ultimately, single molecule detection; this sensitivity would give insight into fundamental binding processes and kinetics, well beyond those possible with ensemble averages.

In addition to classifying biosensors in terms of their signal transduction scheme, they may be divided into sensors in which the target analyte or the receptor biorecognition element is either labeled or unlabeled. The label can be either a fluorescent or radioactive tag. Labeling the analyte may alter the interaction affinity and binding kinetics; it is also a time-consuming and laborious procedure. For radioactive labels, there is an added cost that arises from the generation of hazardous waste and handling of radioactive substances. Therefore, label-free detection schemes are preferred over labeled ones.

This thesis focuses on a label-free detection scheme based on integrated optical resonators. In the discussion that follows, we will first give an overview of mechanical and electrical biosensors, and devote the next section to optical resonators.

Mechanical biosensors rely on the detection of mechanical forces, surface stress or mechanical resonances to quantify the presence of an analyte. The most commonly used mechanical biosensors include microcantilevers (MCs), that may be operated either statically or dynamically, and quartz crystal microbalances (QCMs). MCs operated statically are used by monitoring the deflection of the beam as the analyte binds to the functionalized surface. The deflection of the beam can be recorded with either a piezoresistive readout or by reflecting a laser beam off its surface. MCs operated in a dynamic mode are driven at the resonant frequency of the beam, which changes as molecules bind to its surface. The quartz crystal microbalance (QCM) also measures the change in resonant frequency of a piezoelectric quartz crystal resonator associated with the addition of mass to the sensor. They

are part of a larger class of sensors based on surface acoustic waves (SAW). Both MCs and QCMs have detection limits in the picomolar range and have been commercialized.

Electrical biosensors include modified field effect transistors (FETs) that respond to biomolecular interactions that alter the electrical properties of a semiconductor nanowire that connects the source electrode (S) and the drain electrode (D) of the FET. A voltage applied to a gate electrode (G) influences the conductivity of the channel between the source and the drain. For biosensing, the source and drain electrodes are connected using either a semiconductor nanowire (NW) or carbon nanotubes (CNTs) functionalized with a biorecognition element. When charged molecules of the analyte bind to either the NW or to the CNTs, the resulting change in the conductivity of the channel provides a signal from which one can infer the concentration of the target molecule. A drawback of bionsensor FETs is the small size of the sensor, which results in a very small mass transport, and, thus, a lengthy assay time, sometimes on the order of days [7]. Moreover, FET-based biosensors are also difficult to integrate with ionic solutions and buffers, due to Debye screening, such as that which occurs when charged positive ions screen the negatively charged DNA strands [8].

1.1.1 Optical biosensors: Fluorescence and Refractive Index Detection

Optical biosensors function by monitoring the light-matter interaction, and can be categorized in terms of the optical properties of the analyte that they monitor for detection, such as: fluorescence intensity, refractive index, Raman scattering, or light absorption. Fluorescence detection is usually performed as a labeled assay in which a fluorophore has been covalently bound to the analyte. Incident radiation at a specific wavelength is absorbed by the fluorophore, exciting a singlet electronic state that then emits light at a longer wavelength. While fluorescence assays are very powerful, they do suffer a number of drawbacks. The attachment of the marker to the analyte adds complexity to sample preparation, and may influence the properties of the analyte by occluding an active binding site or changing the binding kinetics. Furthermore, fluorescence detection is an end-point detection scheme in that the binding kinetics are not recorded in real-time. Background fluorescence raises the threshold for detection and must be adressed with great care to obtain quantitive results. Lastly, the fluorophore can be destroyed due to long exposure times and high intensity of the radiation, a process termed "photobleaching." Despite these challenges, fluorescence experiments are widely used in high-throughput screening assays and molecular dynamics studies. The most established fluorescence assay is the enzyme-linked immunosorbent assay (ELISA). It can be used in direct, indirect, or "sandwich" formats. First, the antigen to be detected is immobilized on a surface, either by adsorption to the surface, or to a primary antibody previously attached to the plate. Next, the primary antibody, which is now labeled with a fluorophore, is introduced in solution, and binds to the antigen (direct assay). Alternatively, the primary antibody is not labeled, but provides a binding site for secondary labeled antibody (indirect and sandwich assay). The latter option increases the

specificity of the interaction.

Another category of optical biosensors monitors changes in the refractive index due to the presence of the analyte in the medium. Typically, organic molecules have a higher index of refraction than the surrounding medium, so they affect the optical mode of electromagnetic field. Among optical biosensors based on refractive index changes, the most established is the surface plasmon resonance (SPR) sensor, which was introduced in 1983 by Liedberg [9]. The technology was later further developed by researchers at Linköping University in Sweden and commercialized by BIAcore^{TM}, now acquired by GE [5]. It is based on the generation of a surface plasmon wave in a thin metal film, usually gold or silver. Surface plasmons are charge oscillations generated by the evanescent field of light as it undergoes total internal reflection at the interface with the metal. Resonance that occurs when the momentum of the incident light matches that of the plasmon wave, generates a surface wave. At resonance, a light beam reflected from the metal surface exhibits a minimum in intensity. When the refractive index of the exit dielectric medium changes due to binding of analyte to the metal, the momentum of the surface wave also changes, leading to a shift in the angle of incidence of the incoming light at which the light-beam momentum matches that of the plasmon wave. By monitoring the incident angle at resonance, the concentration of bound analyte to the metal surface can be inferred.

A novel optical biosensor, the photonic crystal, relies on a defect inside a periodic dielectric nanostructure that allows a single resonant frequency to propagate inside the structure. When the refractive index around the defect changes to the presence of the analyte, the resonant frequency changes as well, indicating the amount of bound analyte. Photonic crystals are usually achieved in either 1D or 2D.

Other high sensitivity refractive index sensors also rely on detecting shifts in resonances within interferometers, waveguides, optical fibers, and other devices.

Lastly, microcavity whispering gallery mode (WGM) resonators exploit the resonance condition established when a beam of light is confined by total internal reflection inside a circular structure. The evanescent field of the optical mode samples the index of refraction of the surrounding medium. When an analyte enters the evanescent field, it changes the propagation speed of the light, influencing the resonance condition which is detected as a minimum in the frequency transmission spectrum. This thesis focuses on one type of whispering gallery mode resonator.

1.1.2 Microcavity whispering gallery mode resonators

Although the principle of the detection is the same across WGM platforms, *i.e.*, monitoring the resonance frequency shift upon binding of the analyte due to its interaction with the evanescent field, their geometries differ. The most prominent technologies are: liquid-core ring resonators (LCORR), microsphere resonators, microtoroids, planar ring resonators, and disk resonators. LCORR res-

onators are thin capillaries, and they are easy to fabricate and compatible with fluid delivery. Microsphere resonators are also easy to fabricate, and achieve very high sensitivities, but they are hard to integrate into multiplexed platforms. Microtoroids can be fabricated and integrated easily, but they are delicate, and the light coupling between the fiber and the sensor is not robust. Planar ring and disk resonators offer the most robust and reproducible fabrication, compatible with silicon processing technology, are easily multiplexed, and can be easily integrated with a fluidic delivery system. In this work we will use planar ring resonators, since they are the most promising among WGM sensors.

1.2 Applications

A major application of biosensors is for the medical industry, in performing assays for clinical diagnosis and drug engineering. Moreover, they have applications in protein analysis, DNA hybridization assays, and detection of viruses, bacteria, and cells. In terms of fundamental research, they are employed in characterizing biomolecular interactions and extracting real-time binding kinetics information. Other areas include environmental monitoring and food testing for toxins and pathogens.

Protein analysis is based on the high affinity binding of antibodies to antigens, or of engineered aptamers to target molecules. The latter technique allows for engineering receptors for an unlimited number of target analytes by selectively and predictably folding short DNA sequences. The synthesis of aptamers is very reproducible, and they are less prone to denaturation than proteins; this makes them excellent tools in biorecognition [10]. One major application of protein analysis is for cancer diagnosis through the detection of cancer and inflammation biomarkers in serum. For example, two breast cancer biomarkers, CA15-3 and HER2, have been detected in blood serum by different groups [11, 12]. Washburn *et al.* detected a colorectal cancer biomarker, carcinoembryonic antigen (CEA) [13]. It was followed by multiplexed detection of five protein biomarkers, among which three cancer biomarkers: tumor necrosis factor-α (TNF-α), prostate specific antigen (PSA), and CEA, as well as two inflammation markers: α-fetoprotein (AFP) and interleukin-8 (IL-8), paving the way for fingerprint biomarker assays [14]. Recently, they detected up to eight cancer biomarkers simultaneously [15]. Moreover, detection of pathogen biomarkers against the Ebola virus, Marburg virus, and dengue virus have been reported [16]. Another set of protein detection assays are aimed at studying kinetic binding rates, such as the streptavidin-biotin interaction [17]

Target DNA strands are detected using DNA hybridization assays. The target DNA binds to complementary DNA oligonucleotide probes that are immobilized on the sensor. Suter *et al.* used an LCORR sensor to detect target DNA consisting of $25-100$ base pairs, and in a concentration range of $10\,\mathrm{pM}$ to $10\,\mu\mathrm{M}$. They also detected single-nucleotide polymorphisms (SNPs), which are base mismatches consisting of $1-5$ nucleotides, and the degree of DNA methylation [18, 19]. Vollmer

et. al used a 200 µm silica microsphere to detect 27-base nucleotides and a 1 nucleotide mismatch in an 11-base target [20]. Ramachandran *et al.* used 100 µm diameter ring resonators made of Hydex^{TM} glass to detect 24-base target DNA of 500 nM concentration [21]. Qavi *et al.* used SOI ring resonators of 30 µm diameter to detect DNA concentrations as low 1.95 nM and the presence of SNPs by monitoring kinetic desorption rates [22]. Later, they detected miRNA in a concentration range from 1.95 nM to 2 µM[23].

In terms of virus, bacterial, or cell detection, Arnold *et al.* detected the MS2 RNA virus with a 20 nm diameter of a concentration of 5 pM [24]. Zhu *et al.* detected filamentous M13 bacteriophage with a detection limit of 2.3×10^3 pfu ml^{-1} against anti-M13 antibody [25]. And Vollmer *et al.* detected single Influenza A virus of radius 50 nm from a concentration of 10 fM [26]. Sloan *et al.* investigated the interaction between proteins and the cell membrane using phospholipid bilayer nanodiscs [27]

1.3 Thesis Structure

In this thesis we focus on the development of a biosensing platform consisting of ring resonator biosensors integrated with microfluidics. Ring resonators are an emerging technology with multiplexing capabilities, since due to their small size they can be easily integrated at high densities on chip, and their fabrication is compatible with established nanotechnology processes. In terms of development, we focus on three areas: achieving a low detection limit by removing environmental noise with a differential measurement scheme, fast response time by optimizing the fluidic delivery system and introducing a new channel design, and multiplexing capabilities using photochemistry protocols. In Chapter 2, we focus on the characterization of ring resonators. We present different established platforms used by other groups and performance metrics of similar systems, and show simulations of sensitivies of our ring resonator geometry. In terms of detection limits, we will show fabricated high-Q resonators, and investigate the effect of environmental noise on their performance. Then, we introduce the dual-laminar flow platform, and, through simulations and experiments, quantify its benefits in reducing the noise in the system. In Chapter 3 we focus on the design and optimization of the new microfluidic platform and characterize the response time of the sensors, in an attempt to improve the assay time. In Chapter 4 we explore different chemistry protocols with two major goals. The first half focuses on the conditions required for the deposition of a monolayer of the linker layer, which enables attachment of a number of sensor molecules and, thereby, the study of different biomolecular interactions. In the second half, we explore a new chemistry aimed at photopatterning the sensor and passivating the rest of the channel that would not only allow for multiplexed detection, and achieve high selectivity of binding, but also enhance the mass transport to the sensor. In Chapter 5 we introduce a new channel design aimed at enhancing the mass transport to the sensor,

and show how geometrical parameters influence its effect on the response time. Lastly, Chapter 6 offers possible future directions, and design improvements.

Bibliography

[1] X. Fan, I. M. White, S. I. Shopova, H. Zhu, J. D. Suter, and Y. Sun, "Sensitive optical biosensors for unlabeled targets: A review," *Analytica Chimica Acta*, vol. 620, no. 12, pp. 8 – 26, 2008.

[2] H. Zhu, J. D. Suter, and X. Fan, *Optical Guided-wave Chemical and Biosensors II*, ch. Label-Free Optical Ring Resonator Bio/Chemical Sensors, pp. 259–279. Springer Berlin Heidelberg, 2010.

[3] J. T. Kindt and R. C. Bailey, "Biomolecular analysis with microring resonators: applications in multiplexed diagnostics and interaction screening," *Current Opinion in Chemical Biology*, vol. 17, no. 5, pp. 818 – 826, 2013.

[4] Y. Sun and X. Fan, "Optical ring resonators for biochemical and chemical sensing," *Analytical and Bioanalytical Chemistry*, vol. 399, no. 1, pp. 205–211, 2011.

[5] A. P. F. Turner, "Biosensors–sense and sensitivity," *Science*, vol. 290, no. 5495, pp. 1315–1317, 2000.

[6] R. Malhotra, V. Patel, J. P. Vaqu, J. S. Gutkind, and J. F. Rusling, "Ultrasensitive electrochemical immunosensor for oral cancer biomarker IL-6 using carbon nanotube forest electrodes and multilabel amplification," *Analytical Chemistry*, vol. 82, no. 8, pp. 3118–3123, 2010.

[7] J. L. Arlett, E. B. Myers, and M. L. Roukes, "Comparative advantages of mechanical biosensors," *Nature Nanotechnology*, vol. 6, pp. 203 – 215, 2011.

[8] E. Stern, R. Wagner, F. J. Sigworth, R. Breaker, T. M. Fahmy, and M. A. Reed, "Importance of the Debye screening length on nanowire field effect transistor sensors," *Nano Letters*, vol. 7, no. 11, pp. 3405–3409, 2007.

[9] B. Liedberg, C. Nylander, and I. Lunstrm, "Surface plasmon resonance for gas detection and biosensing," *Sensors and Actuators*, vol. 4, pp. 299 – 304, 1983.

[10] W. Zhou, P.-J. Jimmy Huang, J. Ding, and J. Liu, "Aptamer-based biosensors for biomedical diagnostics," *Analyst*, vol. 139, pp. 2627–2640, 2014.

[11] H. Zhu, P. S. Dale, C. W. Caldwell, and X. Fan, "Rapid and label-free detection of breast cancer biomarker CA15-3 in clinical human serum samples with optofluidic ring resonator sensors," *Analytical Chemistry*, vol. 81, no. 24, pp. 9858–9865, 2009.

[12] J. T. Gohring, P. S. Dale, and X. Fan, "Detection of HER2 breast cancer biomarker using the opto-fluidic ring resonator biosensor," *Sensors and Actuators B: Chemical*, vol. 146, no. 1, pp. 226 – 230, 2010.

[13] A. L. Washburn, L. C. Gunn, and R. C. Bailey, "Label-free quantitation of a cancer biomarker in complex media using silicon photonic microring resonators," *Analytical Chemistry*, vol. 81, no. 22, pp. 9499–9506, 2009.

[14] A. L. Washburn, M. S. Luchansky, A. L. Bowman, and R. C. Bailey, "Quantitative, label-free detection of five protein biomarkers using multiplexed arrays of silicon photonic microring resonators," *Analytical Chemistry*, vol. 82, no. 1, pp. 69–72, 2010.

[15] A. L. Washburn, W. W. Shia, K. A. Lenkeit, S.-H. Lee, and R. C. Bailey, "Multiplexed cancer biomarker detection using chip-integrated silicon photonic sensor arrays," *Analyst*, pp. –, 2016.

[16] I. A. Estrada, R. W. Burlingame, A. P. Wang, K. Chawla, T. Grove, J. Wang, S. O. Southern, M. Iqbal, L. C. Gunn, and M. A. Gleeson, "Multiplex detection of pathogen biomarkers in human blood, serum, and saliva using silicon photonic microring resonators," *Proc. SPIE*, vol. 9490, pp. 94900E–94900E–14, 2015.

[17] C. E. Soteropulos, H. K. Hunt, and A. M. Armani, "Determination of binding kinetics using whispering gallery mode microcavities," *Applied Physics Letters*, vol. 99, no. 10, 2011.

[18] J. D. Suter, I. M. White, H. Zhu, H. Shi, C. W. Caldwell, and X. Fan, "Label-free quantitative DNA detection using the liquid core optical ring resonator," *Biosensors and Bioelectronics*, vol. 23, no. 7, pp. 1003 – 1009, 2008.

[19] J. D. Suter, D. J. Howard, C. W. Caldwell, H. Shi, and X. Fan, "Label-free DNA methylation analysis using the optofluidic ring resonator sensor," *Proc. SPIE*, vol. 7322, pp. 732208–732208–8, 2009.

[20] F. Vollmer, S. Arnold, D. Braun, I. Teraoka, and A. Libchaber, "Multiplexed DNA quantification by spectroscopic shift of two microsphere cavities," *Biophysical Journal*, vol. 85, no. 3, pp. 1974 – 1979, 2003.

[21] A. Ramachandran, S. Wang, J. Clarke, S. Ja, D. Goad, L. Wald, E. Flood, E. Knobbe, J. Hryniewicz, S. Chu, D. Gill, W. Chen, O. King, and B. Little, "A universal biosensing platform based on optical micro-ring resonators," *Biosensors and Bioelectronics*, vol. 23, no. 7, pp. 939 – 944, 2008.

[22] A. J. Qavi, T. M. Mysz, and R. C. Bailey, "Isothermal discrimination of single-nucleotide polymorphisms via real-time kinetic desorption and label-free detection of DNA using silicon

photonic microring resonator arrays," *Analytical Chemistry*, vol. 83, no. 17, pp. 6827–6833, 2011.

[23] A. Qavi and R. Bailey, "Multiplexed detection and label-free quantitation of microRNAs using arrays of silicon photonic microring resonators," *Angewandte Chemie International Edition*, vol. 49, no. 27, pp. 4608–4611, 2010.

[24] S. Arnold, R. Ramjit, D. Keng, V. Kolchenko, and I. Teraoka, "Microparticle photophysics illuminates viral bio-sensing," *Faraday Discuss.*, vol. 137, pp. 65–83, 2008.

[25] H. Zhu, I. M. White, J. D. Suter, M. Zourob, and X. Fan, "Opto-fluidic micro-ring resonator for sensitive label-free viral detection," *Analyst*, vol. 133, pp. 356–360, 2008.

[26] F. Vollmer, S. Arnold, and D. Keng, "Single virus detection from the reactive shift of a whispering-gallery mode," *Proceedings of the National Academy of Sciences*, vol. 105, no. 52, pp. 20701–20704, 2008.

[27] C. D. K. Sloan, M. T. Marty, S. G. Sligar, and R. C. Bailey, "Interfacing lipid bilayer nanodiscs and silicon photonic sensor arrays for multiplexed proteinlipid and proteinmembrane protein interaction screening," *Analytical Chemistry*, vol. 85, no. 5, pp. 2970–2976, 2013.

Chapter 2

Differential sensing and noise considerations

2.1 Basics of ring resonators

As discussed in the previous chapter, ring resonators can be employed as sensitive chemical sensors to quantitatively detect the presence of very low concentrations of analyte and to measure affinity binding kinetics. A ring resonator consists of a looped waveguide, to which the circulating light is confined via total internal reflection. The light is coupled into the ring from an adjacent bus waveguide through its evanescent field. A resonance occurs when the effective path of the looped waveguide is an integer number of wavelengths, leading to constructive interference of the circulating wave with itself. The resonance condition reads:

$$M\lambda_{\text{res}} = (2\pi R)n_{\text{eff}},$$

where λ_{res} is the wavelength of light in air, M is the azimuthal mode number, R is the average radius of the ring, and n_{eff} is the effective index of refraction of the propagating mode.

A few important figures of merit related to the operation of the ring resonators are:

- **The quality factor (Q-factor)** of a resonator is related to the sharpness of the resonance, and is a measure of the optical energy losses in the resonator. In the case of an un-driven resonator oscillating at its resonant frequency ω_0, the Q-factor is defined as:

$$Q = \omega_0 \frac{U(t)}{-dU(t)/dt},$$

where $U(t)$ is the energy stored in the resonator and $-dU(t)/dt$ is the rate of energy loss.

Solving for $U(t)$, we derive:

$$U(t) = U_0 \exp(-\omega_0 t/Q),$$

so the energy in the resonator decays exponentially with a time constant $\tau = Q/\omega_0$. The characteristic time τ is known as the photon lifetime. Thus, Q represents the number of oscillations undegone by a photon in the ring resonator before it is lost to the surrounding medium. The higher the Q-factor, the longer the lifetime of the photon, which leads to an enhanced interaction of the light with the surrounding medium, and, thus, to an increased effective cavity length. By Fourier transforming from the time domain to the frequency domain, we derive the spectral response of the resonator:

$$L(\omega) = \frac{1}{\pi} \frac{(\omega_0/(2Q))^2}{(\omega - \omega_0)^2 + (\omega_0/(2Q))^2},$$

which is a Lorentzian lineshape centered around ω_0 with linewidth (FWHM) $\Delta\omega = \omega_0/Q$. Thus, the Q-factor can be interpreted as the ratio of the central resonant frequency to the linewidth:

$$Q = \frac{\omega_0}{\Delta\omega}.$$

The higher the Q-factor, the sharper the resonance linewidth. For a lossless resonator, Q would be infinite.

The overall Q-factor of a resonator depends on the various loss mechanisms of the system. Its main components are intrinsic, Q_{int}, and extrinsic, Q_{ext}. Q_{int} depends on the losses inside the ring, which can be attributed to either material absorption Q_{abs} in the core or cladding, surface scattering Q_{scat} due to surface roughness and contamination, or radiation Q_{rad} due to bend losses. Q_{ext} measures losses due to the coupling to the bus waveguide. Overall:

$$\frac{1}{Q} = \frac{1}{Q_{\text{int}}} + \frac{1}{Q_{\text{ext}}} = \left(\frac{1}{Q_{\text{abs}}} + \frac{1}{Q_{\text{scat}}} + \frac{1}{Q_{\text{rad}}}\right) + \frac{1}{Q_{\text{ext}}}.$$

- **The free spectral range (FSR)** of the ring represents the frequency spacing between two adjacent resonances:

$$\text{FSR} = \frac{\lambda^2}{2\pi R n_{\text{g}}},$$

where n_{g} is the group index of the mode, and is inversely proportional to the group velocity v_{g}: $n_g = c/v_{\text{g}} = (\partial n_{\text{eff}}/\partial\omega) \times \omega + n_{\text{eff}}$. The laser tuning range should be slightly larger than the FSR of the ring if we want to find as least one and no more than two resonances in the transmission spectrum.

A few design parameters of the ring resonator that influence its performance are:

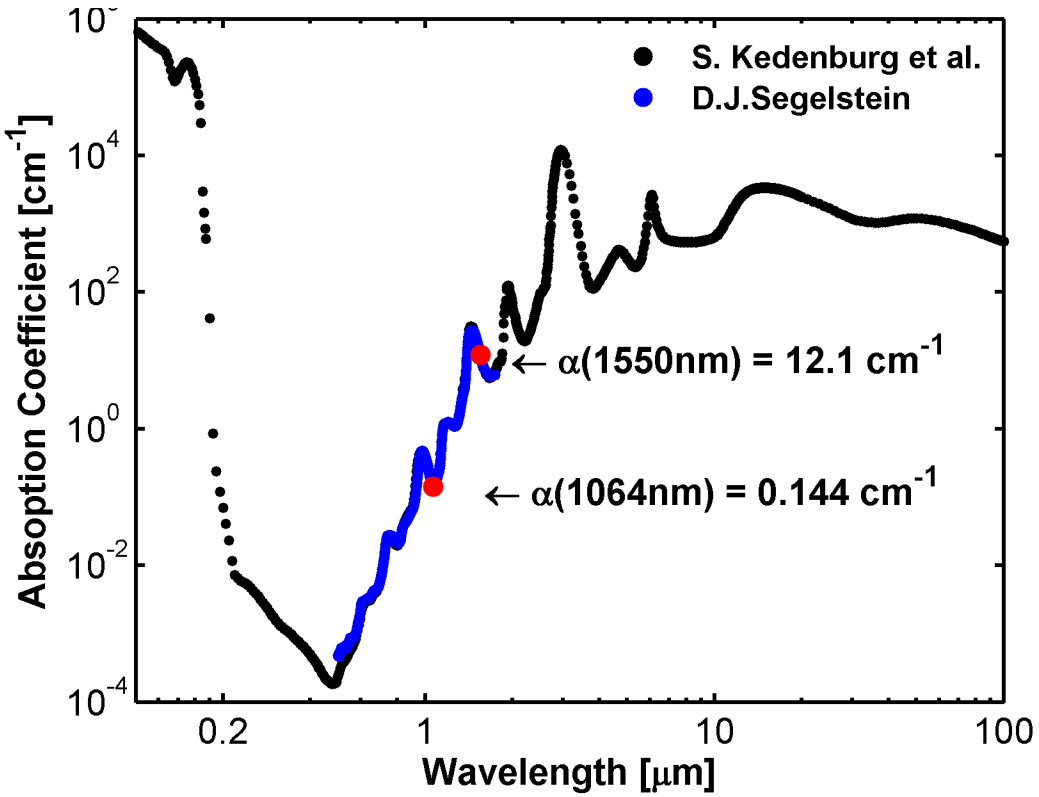

Figure 2.1: Water absorption coefficient at various wavelengths of light. The data from Segelstein [1] covers a wider range, but the data from Kedenburg *et al.* [2] is denser in the range of interest. The two sets of data agree fairly well, giving a coefficient of absorption about two orders of magnitude larger at 1550 nm than at 1064 nm.

- **Wavelength of operation**. Most groups operate at telecom wavelengths of $\lambda = 1550\,\text{nm}$, but, as seen in Figure 2.1, water absorption is very high in this region, and dominates the degradation of the Q-factor. Therefore, we chose to operate at $\lambda = 1064\,\text{nm}$, where the absorption coefficient of water is two orders of magnitude smaller. The absorption coefficient of water at 1550 nm is $\alpha = 12\,\text{cm}^{-1}$, whereas at 1064 nm, it is $\alpha = 0.144\,\text{cm}^{-1}$.

- **Material**. The choice of material influences the profile and confinement of the mode and thus its interaction with the surrounding medium. Most groups use silicon (Si) as a material for their resonators because of its ease of fabrication, and because of its high index of refraction, $n_{\text{Si}} = 3.5$, which results in high optical confinement in the waveguide. However, Si has a band gap of 1.11 eV, which leads to increased material absorption at wavelengths below 1100 nm. As shown above, water absorption at wavelengths higher than 1100 nm is very large. An alternate material is silicon nitride (Si_3N_4), a CMOS-compatible material, with a band gap of 5 eV. It has an absorption spectrum that is transparent in a wavelength range of 300 nm-6 µm. Furthermore, silicon nitride is a dielectric, so it does not suffer free-carrier absorption, and has low two-photon absorption.

- **Mode polarization**. A waveguide can support TE (transverse electric) or TM (transverse magnetic) modes. The TE modes have no electric-field component in the axial direction, whereas TM modes have no electric-field component in the radial direction. The electric-field of TM modes has little overlap with the sidewalls and therefore less scattering losses than the TE modes. The confinement of the TM mode is also smaller than the confinement of the TE modes, which leads to increased sensitivity. However, since the TM mode penetrates farther into the surrounding medium, absorption in water can degrade the Q-factor.

- **Geometry parameters** The main geometrical parameter of the ring is its radius r. A small radius will introduce bend losses which increase radiation and lower the overall Q. At the same time, a larger radius will increase the interaction of the mode with the side walls, and increase scattering losses. Various geometries have been used in order to increase the overlap of the mode with the analyte of interest. Some groups employ slot resonators, which allow the mode within the slot to interact with the solution of interest. Other groups have employed porous Si as the resonator material, which allows the particles/molecules of interest to enter the pores and interact with the mode. However, the addition of the extra surfaces of the pores can lower the Q-factor through scattering losses.

The performance metrics commonly used to characterize the sensor are:

- **The sensitivity (S)**, represents the change in resonant frequency per change of index of refraction of the bulk solution. It is determined by the light-matter interaction, and depends on the fraction of the optical mode that interacts with the analyte. There is a trade-off between increased sensitivity and high Q-factor; the more the mode is pushed outward, the better the sensitivity, but the higher the absorption losses within the surrounding medium.

- **The limit of detection (LOD)** represents the smallest change that can be discriminated. It is defined as:

$$\mathrm{LOD} = \frac{3\sigma}{S},$$

  where S is the sensitivity and σ is the standard deviation of the baseline signal.

There have been a multitude of experiments and designs of WGM resonators. Some of the geometries employed and their performance metrics are shown in Table 2.1.

As a result of the above considerations, our choice of material for the ring resonators is silicon nitride, and the radius of the ring resonator is $r = 70\,\mu\mathrm{m}$. The chosen radius is the largest possible radius given the e-beam patterning system, since we want the ring to be contained inside one e-beam write field to avoid stitching issues. Furthermore, by having a large radius we minimize bend losses in the ring. However, the added circumference may deteriorate the Q-factor due to scattering losses, but this represents a smaller effect than the bend losses. The material choice is low-stress LPCVD

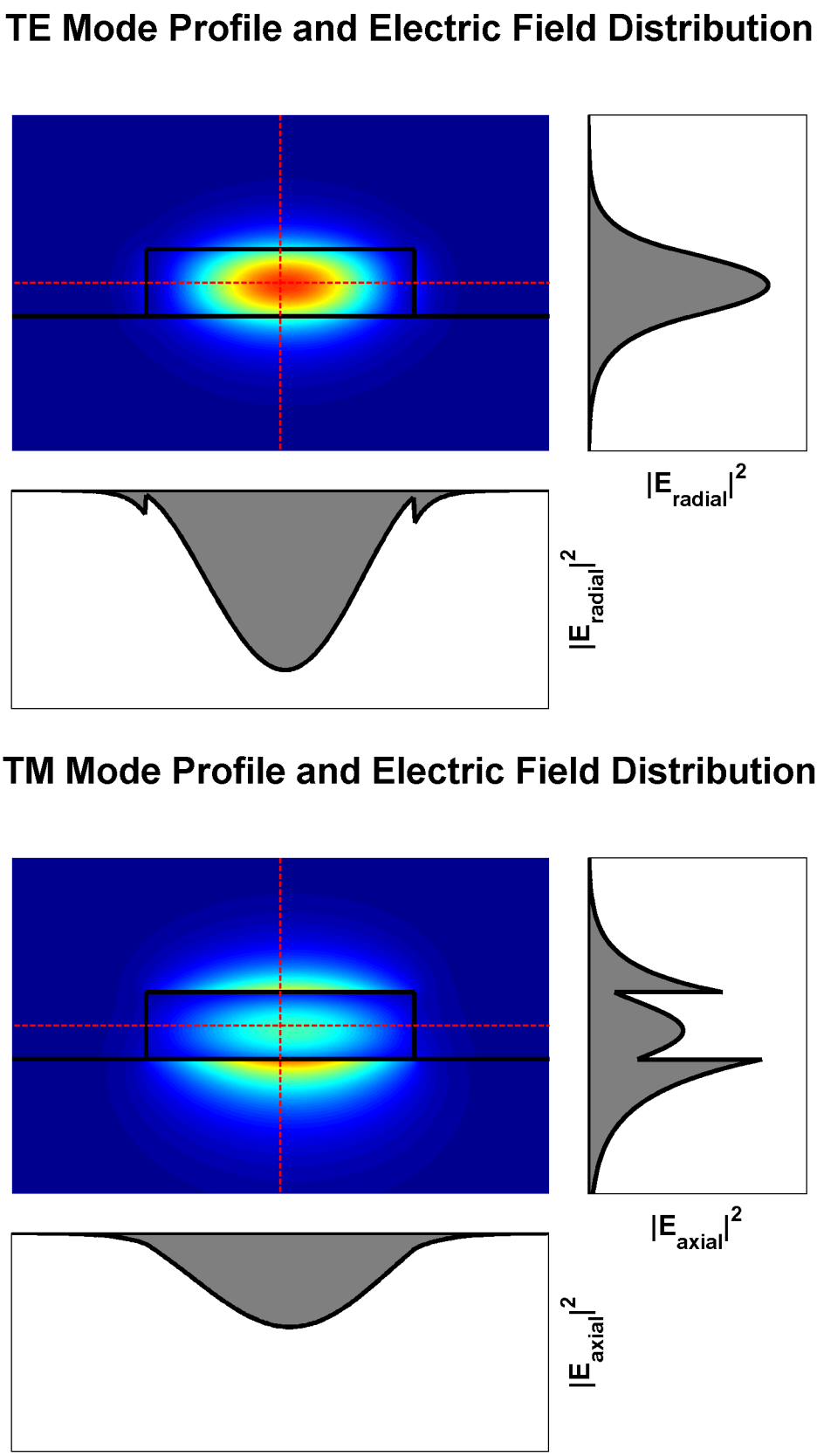

Figure 2.2: a) Mode profile of ring resonator for TE mode in water. b) Mode profile for TM mode in water.

Radius	Q (aqueous)	Material	Bulk refractive index sensitivity	LOD (RIU)	LOD (other)	Wavelength	Reference
15 µm	4,300	SOI	163 nm/RIU	7.6×10^{-7}	60 fM	1550 nm	Iqbal et al. [3]
13 µm ×10 µm racetrack slot	-	SOI	298 nm/RIU	4.2×10^{-5}	-	1550 nm	Claes et al. [4]
5 µm racetrack	20,000	SOI	70 nm/RIU	10^{-5}	-	1550 nm	Vos et. al [5]
70 µm slot	1,800	Si_3N_4	212 nm/RIU	2.3×10^{-4}	-	1260-1370 nm	Barrios et. al [6]
22-28 µm	25,000	SOI	135 nm/RIU	-	20 pM	-	D.-X.Xu [7]
45 µm	20,000	polystyrene	-	10^{-7}	250pg/mm^2	1550 nm	Chao et. al [8]
60 µm	12,000	Hydex	-	1.8×10^{-5}	-	1550 nm	Yalcin et. al [9]
10 µm, 25 µm	4,000	porous Si	380 nm/RIU	1.8×10^{-5}	3 nM nucleic acid	1500-1630 nm	Rodriquex et. al [10]
30 µm	75,000	SiN	91 nm/RIU	-	-	965-995 nm	Goykhman et. al [11]

Table 2.1: Review of other ring resonator platforms.

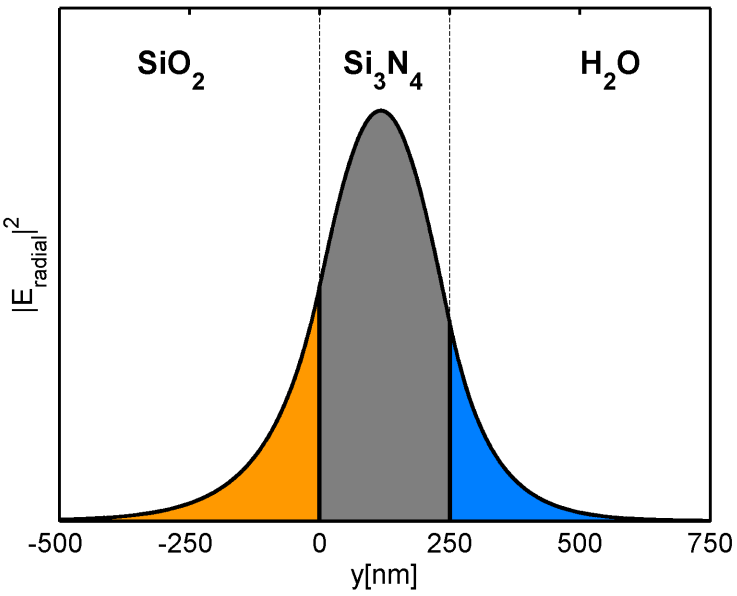

Figure 2.3: Mode profile along a vertical section through the center of resonator. The different colors indicate the different media through which the mode propagates. By fitting a decaying exponential to the tail of the evanescent field inside water, we obtain a decay constant of 160 nm.

stoichiometric Si_3N_4 (Rogue Valley Microdevices, Medford, OR) on top of a thermally grown oxide layer. The height of the Si_3N_4 is $250\,\text{nm} \pm 5\%$, and the height of the SiO_2 is $6\,\mu\text{m} \pm 5\%$. The nitride is deposited by chemical vapor deposition using dicholorosilane (SiH_2Cl_2) and ammonia (NH_3) in a horizontal vacuum furnace at a temperature of 800 °C. The refractive index at $\lambda = 632\,\text{nm}$ is 2.00 ± 0.05. The substrate is a bare P/Boron doped, $\langle 100 \rangle$ silicon wafer. The mode profiles in the ring are simulated and displayed in Figure 2.2. The simulated FSR of the ring was determined to be FSR = 343 GHz in water, which is comparable to our laser scanning range of 400 GHz.

The electromagnetic energy confined to the ring exhibits an evanescent tail that interacts with the surrounding medium of the ring (see Figure 2.3). The evanescent tail probes the index of refraction of the surrounding medium; variations in the upper cladding affect the resonance frequency of the ring. If we introduce a solution with an unknown index of refraction, we can monitor the change in resonance frequency and derive the actual concentration of solute. The resonator responsivity is calibrated by exposure to known concentrations of the same solute. Blind experiments confirm the validity of the calibration steps. Similarly, a target molecule that binds to the ring resonator affects the index of refraction of the upper cladding and produces a quantifiable resonance shift. Models of the binding kinetics in conjunction with calibration steps enable us to determine the bulk concentration of the target molecule.

The fabrication of the rings is detailed elsewhere [12]. In our experiments, we have fabricated

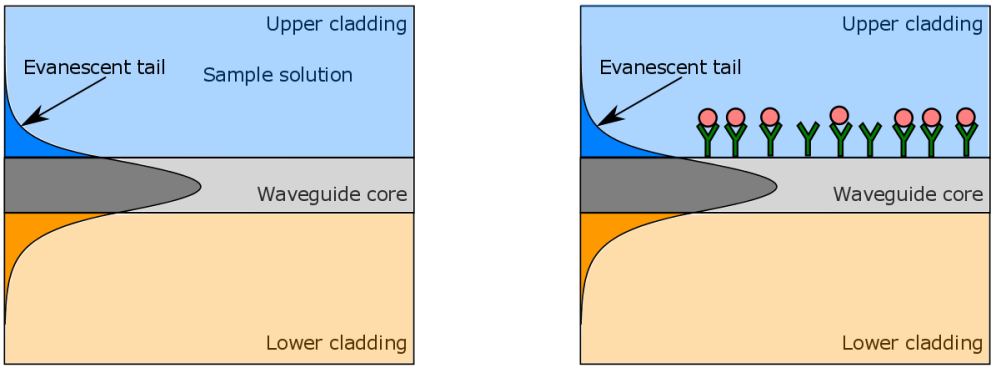

Figure 2.4: a) The evanescent tail of the mode interacts with a bulk solution b) The evanescent tail of the mode interacts with a surface organic layer.

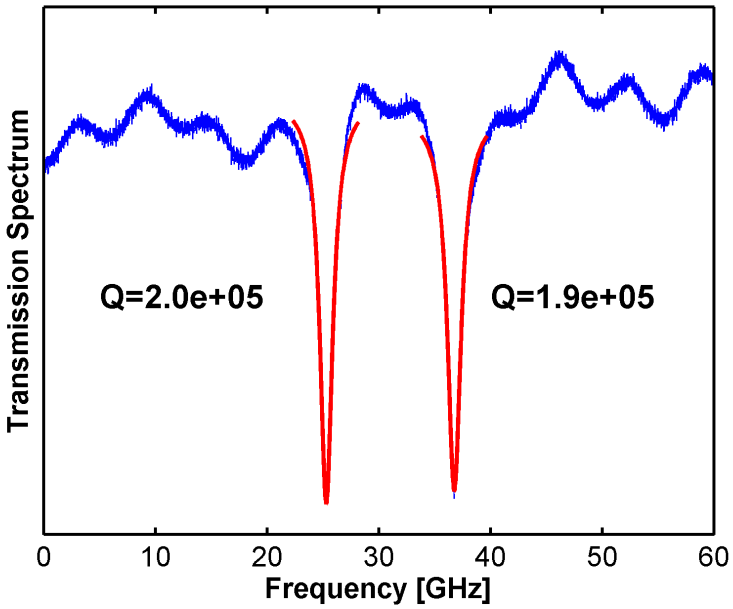

Figure 2.5: Recorded Q-factors of two fabricated rings coupled to the same waveguide.

both ring and disk resonators. The disks have higher Q-factors because of the lack of the interior boundary wall which reduces scattering losses. However, the spectrum of the disk is crowded by multiple resonances, which complicates tracking of individual resonances. Therefore, we employ ring resonators in our experiments. The fabrication yields high Q-factors, on the order of 10^5 in water. In Figure 2.5 we show Q-factors of two resonators that are coupled to the same waveguide. Both resonators have $Q \approx 2 \times 10^5$, and the resonances are spaced by 12 GHz. The spurious oscillations in the signal are due to Fabry-Pérot interference in the waveguide. Figure 2.6 shows SEM pictures of one ring resonator and the coupling region between the waveguide and the resonator.

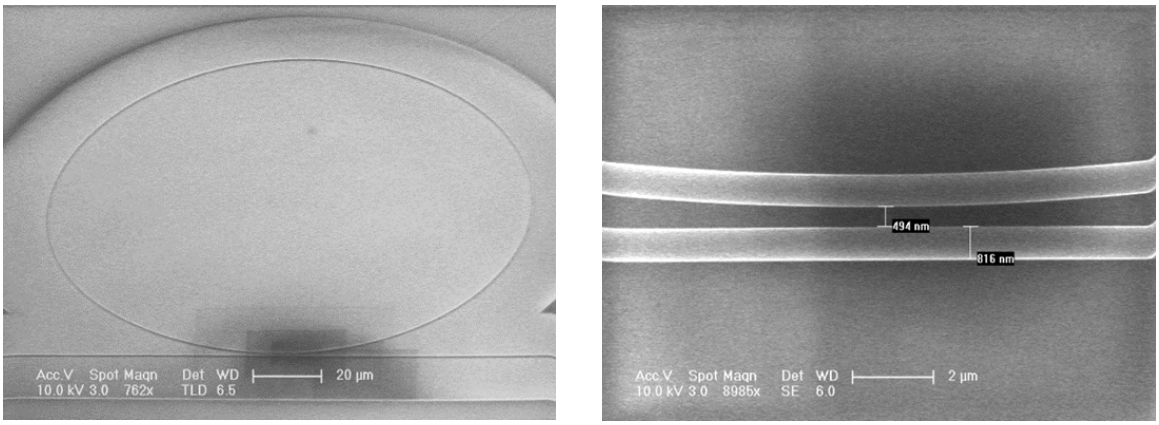

Figure 2.6: a) SEM picture of the ring resonator geometry b) SEM picture of the coupling region between the bus waveguide and the ring resonator. Pictures courtesy of Dongwan Kim.

2.2 Response to bulk and surface chemistry: simulations and experiment

To quantify the performance of our resonators, we determine the resonance shift due to changes in the bulk index of refraction of the upper cladding, and to the deposition of a thin layer of organic material on top of the resonator. We estimate the magnitude of these shifts using COMSOL Multiplysics^{TM}. The finite element method (FEM) simulations are based on the weak formulation of the Maxwell equations, and make use of the axial symmetry of the ring resonators, following a method developed by Oxborrow [13, 14]. Briefly, the Helmholtz equation

$$\nabla \times (\frac{1}{\epsilon} \nabla \times \mathbf{H}) = \left(\frac{\omega}{c}\right)^2 \mathbf{H}$$

is solved for the **H**-field, given an initial guess of the azimuthal mode number M. If the resulting resonant frequency is within a 400 GHz window of the nominal wavelength of 1064 nm, the solution has been found. Due to the simulated 343 GHz FSR of the ring, we expect to find at least one such resonance in our laser scanning range. If no such frequency is encountered, the guess for M is incorrect, and we rerun the simulation with an updated value for M.

2.2.1 Salt titrations

We first assess the performance of our sensors by determining their sensitivity to changes in the bulk index of refraction of the upper cladding. We simulate the response to solutions of sodium chloride (NaCl), whose bulk index of refraction depends on the concentration of the solute. More precisely, a 1% change in concentration corresponds to a change of 0.00171 RIU. Therefore, the index of refraction of a solution of NaCl in H_2O is $n = 0.00171 \times c + 1.324$, with c the concentration

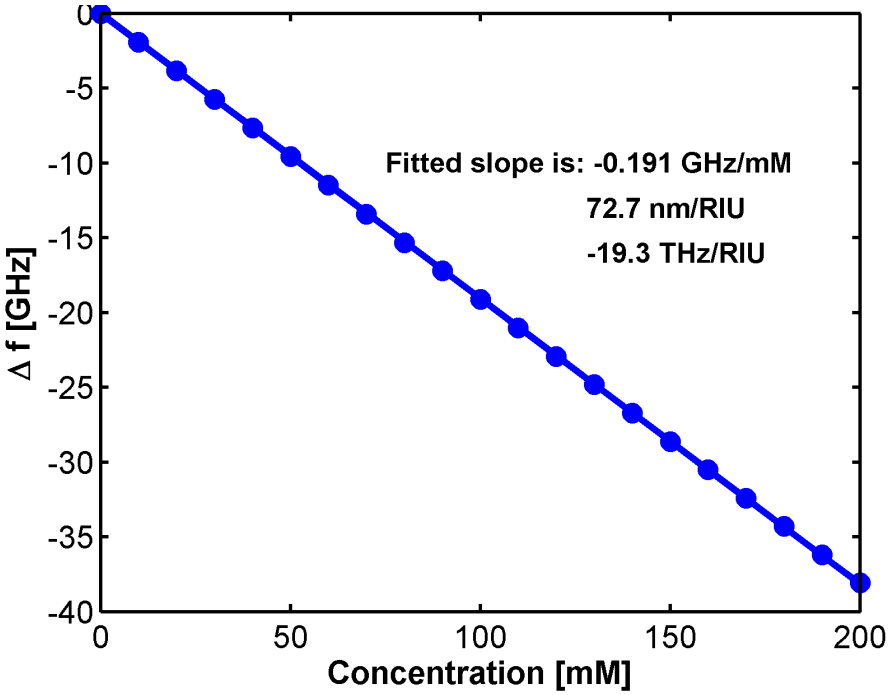

Figure 2.7: a) Change in resonant frequency as a function of salt concentration, for a ring resonator with waveguide height of $h = 250\,\text{nm}$ and ring width of $w = 1\,\mu\text{m}$.

expressed as mass percentage (the mass of the solute over the total mass of the solution) [15, 16]. This relationship was determined at 1550 nm and temperatures of 18 °C, 25 °C and 45 °C; we assume it true at 1064 nm as well.

Initially, FEM simulations determined the expected resonance shift for concentrations of NaCl up to 200 mM. We set the upper cladding index to be the index of refraction of water $n_{H_2O} = 1.324$, and determine the azimuthal mode number M that results in a resonance wavelength within the scanning range of our laser. With the previously determined M, we change the index of refraction of the upper cladding layer with varying concentrations of NaCl, and track the resonance wavelength. We record the resulting resonance frequency, and plot the change in resonance frequency as a function of the molarity of the salt solution (see Figure 2.7). Linear regression reveals a sensitivity to bulk refractive index of $72.7\,\text{nm}\,\text{RIU}^{-1}$, or, alternatively, $-19.3\,\text{THz}\,\text{RIU}^{-1}$.

2.2.2 Organic layer

Most biosensing experiments investigate the binding of organic molecules to the resonator, or to other organic molecules already attached to the resonator. Since the evanescent tail of the mode extends 160 nm into the upper cladding layer, both surface effects and bulk effects contribute to the resonance frequency shift. However, as the field intensity decays exponentially, most of the contribution to the frequency shift is due to surface sensing. As the organic molecules bind to the

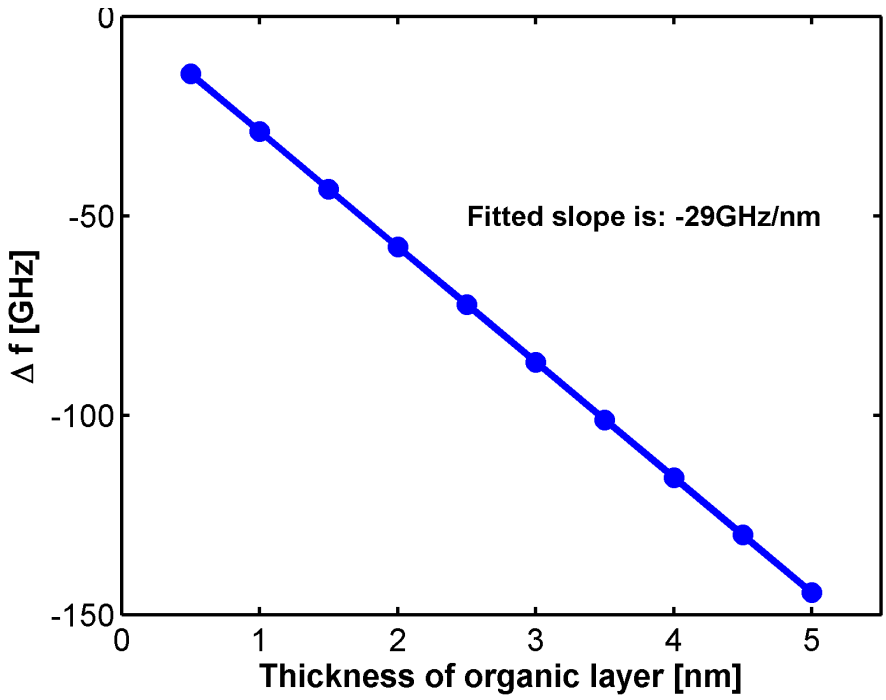

Figure 2.8: Change in resonant frequency as a function of the thickness of the organic layer.

resonator, the thickness and density of the organic layer changes the effective index of the mode. The organic molecules have an index of refraction ($n \approx 1.45$) that is higher than the index of refraction of the water molecules they displaced ($n \approx 1.33$).

Starting from the equation $M\lambda = 2\pi R n_{\text{eff}}$, and assuming small perturbations, the wavelength shift can be expressed as:

$$\Delta\lambda = 2\pi R \frac{\partial n_{\text{eff}}}{\partial n_{\text{upper}}} \Delta n_{\text{upper}} = 2\pi R \Gamma_{\text{upper}} \Delta n_{\text{upper}}.$$

The term Γ_{upper} is known as the confinement factor, and represents the fraction of the optical field intensity of the mode that is located in the upper cladding. Confinement factors for the lower cladding, Γ_{lower}, and for the core, Γ_{core}, are similarly defined. The confinement factor for the organic layer has the form:

$$\Gamma_{\text{org}} = \frac{\int_{\text{org}} n_{\text{org}} |\mathbf{E}(\mathbf{r})|^2 d^3r}{n_{\text{eff}} \int |\mathbf{E}(\mathbf{r})|^2 d^3r}. \tag{2.1}$$

We use perturbation theory to determine Γ_{org}, assuming that the deposition of the thin organic layer does not affect the magnitude and distribution of the electric field. COMSOL simulations provide the mode profile assuming a water upper cladding, from which we extract the electric field in a thickness d at the top and sides of the resonator, and calculate Γ_{org} using Eq.(2.1). The deposition of the thin organic layer of index of refraction $n_{\text{org}} = 1.45$ produces a change in the effective index

n_{eff} of $\Delta n_{\text{eff}} = \Gamma_{\text{org}} \Delta n_{\text{upper}}$. Writing the resonance condition in terms of frequency f,

$$M\left(\frac{c}{f}\right) = (2\pi R) n_{\text{eff}},$$

the frequency shift due to a small change in the index of refraction of the upper cladding, n_{upper}, becomes

$$\Delta f = \frac{-cM\Gamma_{\text{org}}}{2\pi R n_{\text{eff}}^2} \Delta n_{\text{upper}}.$$

Figure 2.8 shows the variation in the frequency shift with thickness of the deposited organic layer; the resulting sensitivity is $29\,\text{GHz}\,\text{nm}^{-1}$.

2.3 Noise sources

2.3.1 Temperature

Thermal noise is the prevalent noise source. One approach to reduce noise due to macroscopic temperature variations is to design an athermal device that allows the thermal effects in the different cladding and core media to cancel each other; this degree of control is difficult to maintain over a large range of upper cladding indexes. The response of the sensor to changes in temperature can be determined from the resonance condition $m\lambda = 2\pi R n_{\text{eff}}$, *i.e.*,

$$\frac{\partial \lambda}{\partial T} = \frac{2\pi}{m}\left(\frac{\partial R}{\partial T} n_{\text{eff}} + R\frac{\partial n_{\text{eff}}}{\partial T}\right) = \frac{2\pi R}{m}\left(\alpha n_{\text{eff}} + \frac{\partial n_{\text{eff}}}{\partial T}\right) = \lambda\left(\alpha + \frac{1}{n_{\text{eff}}}\frac{\partial n_{\text{eff}}}{\partial T}\right),$$

where $\alpha = (\partial R/\partial T)/R$ is the coefficient of thermal expansion of Si_3N_4, $\alpha = 3.27 \times 10^{-6}/^{\circ}\text{C}$. The change $\partial n_{\text{eff}}/\partial T$ can be further expanded to consider the roles of the different media:

$$\frac{\partial n_{\text{eff}}}{\partial T} = \left(\frac{\partial n}{\partial T}\right)_{\text{core}} \Gamma_{\text{core}} + \left(\frac{\partial n}{\partial T}\right)_{\text{lower}} \Gamma_{\text{lower}} + \left(\frac{\partial n}{\partial T}\right)_{\text{upper}} \Gamma_{\text{upper}},$$

$$\frac{\partial n_{\text{eff}}}{\partial T} = \text{TOC}_{\text{core}}\Gamma_{\text{core}} + \text{TOC}_{\text{lower}}\Gamma_{\text{lower}} + \text{TOC}_{\text{upper}}\Gamma_{\text{upper}},$$

where we encounter, as before, the confinement factors Γ that represent the fraction of the modal energy inside each medium:

$$\Gamma_{\text{layer}} = \frac{\int_{\text{layer}} n(r)|\mathbf{E}(\mathbf{r})|^2 d^3r}{n_{\text{eff}} \int |\mathbf{E}(\mathbf{r})| d^3r}.$$

The values used for the indexes of refraction and the thermo-optic coefficients (TOCs) of different materials are summarized in Table 2.2.

Table 2.3 summarizes the estimated confinement factors and the resulting sensitivities to temperature changes in ethanol, water, and air. Due to the large negative TOC of ethanol, the temperature

Material	n	TOC [°C^{-1}]
Ethanol	1.355	-4×10^{-4}
Water	1.324	-8×10^{-5}
Air	1	1×10^{-6}
Silicon nitride	1.986	2.51×10^{-5}
Silicon dioxide	1.45	0.96×10^{-5}

Table 2.2: Indexes of refraction and thermo-optic coefficients for the materials employed.

Upper cladding material	Γ_{upper}	Γ_{core}	Γ_{lower}	M	n_{eff}	$\Delta f/\Delta T$
Ethanol	0.13	0.72	0.15	674	1.630	4.5 GHz/°C
Water	0.12	0.72	0.16	672	1.623	-2.7 GHz/°C
Air	0.06	0.75	0.19	659	1.594	-4.6 GHz/°C

Table 2.3: Calculated values of the confinement factors for three upper cladding media and the resulting temperature sensitivities.

sensitivity in ethanol is positive, $\Delta f/\Delta T = 4.5\,\text{GHz/°C}$. The TOC of water is also negative, but it is smaller than that of ethanol; hence, the overall temperature sensitivity for water is negative, $\Delta f/\Delta T = -2.7\,\text{GHz/°C}$. Lastly, air has a slightly positive TOC, so its temperature sensitivity is more negative than water, $\Delta f/\Delta T = -4.6\,\text{GHz/°C}$. Experimental calibrations of the temperature response of the resonator in all three media will be discussed later in the chapter.

2.3.2 Pressure

Pressure variations affect the response of the sensors by mechanically altering the geometry of the ring. Indeed, Zhao *et al.* use arrays of ring resonators fabricated on deformable diaphragms as sensitive pressure transducers [17]. Changes in the ring shape due to mechanical forces alter the optical mode profile, producing resonance frequency shifts. In our platform, the fluid flow can deform the chip substrate, which has been thinned to enable accurate cleaving along the crystal planes. Later in this chapter we will show experimental pressure calibrations.

2.4 Dual resonator platform

Ring resonators are very sensitive transducers, but, as described above, they are also easily affected by environmental noise. A simple and effective way to remove the ambient noise (also known as common-mode noise) is to perform a differential measurement by introducing a second, reference resonator. Some groups are already using this differential measurement scheme in a geometry in which the reference resonator is covered with a cladding material, usually a polymer (see Table 2.4 for details on polymer type and thickness).

Covering the reference resonator has a number of drawbacks. First, the reference resonator will not be able to fully account for noise generated by the pressure and temperature variations in the

Cladding material	Thickness	Reference
CYTOP	1.1 µm	Iqbal et al. [3]
SU-8	2 µm	Xu et al. [7]
TEOS	530 nm	Gylfason et al.[18]

Table 2.4: Materials used for covering the reference resonator.

analyte stream since it is not in thermal and mechanical contact with the liquid. Second, the extra fabrication steps in depositing the cladding layer and etching a window over the sensing resonator can greatly reduce the fabrication yield. An optimization study has to be carried out to determine the optimal thickness of the cladding layer in order to minimize insertion losses. Third, the flow to the sensing resonator may be influenced by the 1 µm-2 µm thick polymer cladding, reducing mass transfer of the analyte to the sensor. Lastly, some groups report degradation of the cladding with time, in particular SU-8, as it absorbs water over time [7].

To eliminate these drawbacks, reduce the noise floor, and simplify the device fabrication, we introduce a platform in which the reference resonator and the sensing resonator share a common microfluidic channel, through which both are exposed to the fluid flow. Due to the small dimensions of the channel, the flow is viscous, so convection dominates over diffusion. This enables us to flow two streams, one with the chemical of interest, the other with a reference buffer, side-by-side without mixing. Thus, the sensing resonator is exposed to the solution of interest, while the reference resonator is immersed in the reference buffer. This allows both the pressure and temperature of the fluid to equilibrate, enabling the reference resonator to account for those noise sources as well.

2.4.1 Concentration and temperature equilibration

First, we must prove that including the two resonators in the same channel does not induce mixing of the streams that would foul our analyte. For a concentration c_0 at one inlet, and a concentration $c = 0$ at the buffer inlet, COMSOL simulations predict concentration and temperature variations in the diffusion zone shown in Figure 2.9.

Because convection dominates over diffusion for large solute molecules, the molecules are swept downstream before they can diffuse to the resonators. The diffusion length $\delta_c = 2\sqrt{D_c t}$ represents a characteristic length over which the analyte has propagated in time t. Assuming an average velocity in the channel of $v_{\text{avg}} = 1\,\text{mm}\,\text{s}^{-1}$, with the resonators located $L = 1\,\text{mm}$ downstream from the beginning of the common channel, the diffusion length will be $\delta_c \approx 20\,\mu\text{m}$ for a solute with diffusivity $D_c = 10^{-10}\text{m}^2\,\text{s}^{-1}$. Because the resonators are separated by 800 µm, mixing between the two streams is, indeed, negligible.

Like species diffusion, the temperature diffusion length grows as $\delta_t = 2\sqrt{D_t t}$, where D_t is the thermal diffusivity. However, thermal diffusivity is much higher than species diffusivity, D_t =

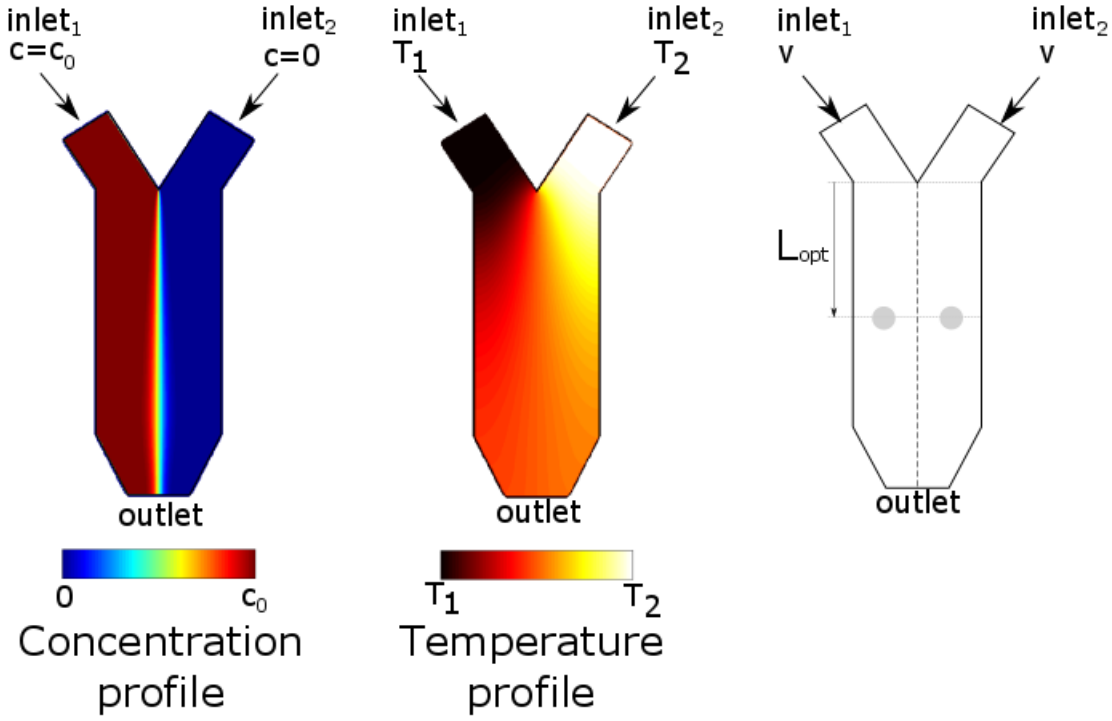

Figure 2.9: Equilibration of concentration and temperature inside the channel

$1.43 \times 10^{-7} \mathrm{m^2\,s^{-1}}$ for water at 25 °C. For a location $L = 1\,\mathrm{mm}$ downstream, the thermal diffusion length becomes $\delta_{\mathrm{th}} \approx 750\,\mu\mathrm{m}$. Thus, the two streams equilibrate thermally, without species mixing.

2.4.2 Sensitivity to geometric parameters

Even when performed with great care, the fabrication of the resonator will lead to deviations from the ideal design parameters. Here we examine the influence of these variations on the response of the resonator, paying particular attention to the effects of small changes in the waveguide height and ring width of the resonator. These variations in the geometrical parameters of the sensing and reference ring lead to different responses to temperature, pressure and concentration changes. On one hand, such variations are desirable because the transmission spectrum will exhibit two separate resonances, simplifying identification and tracking of the two signals since they do not overlap. On the other hand, the responses of the two resonators will differ, as their differential signal will not exactly cancel. Because the two resonators are in close proximity, these fabrication variations should be fairly small.

To investigate the effect of the ring geometry, we perform simulations in which we vary the height

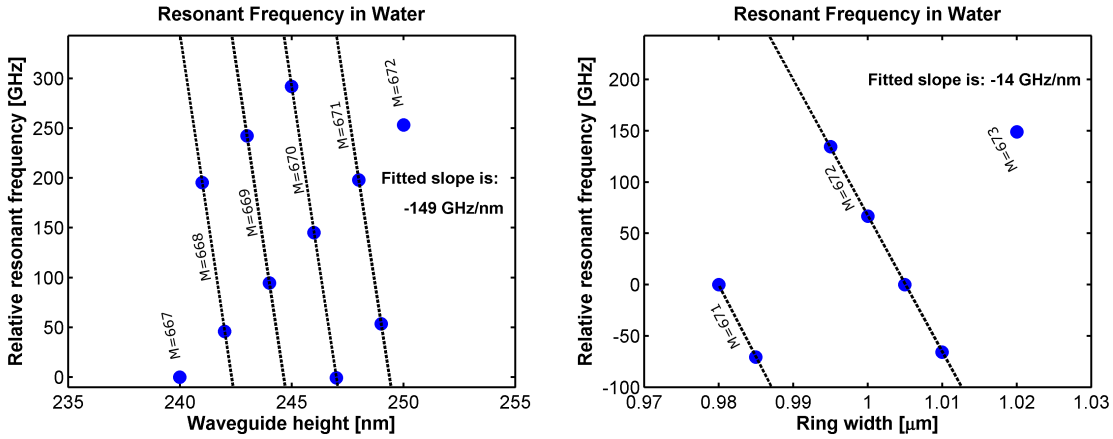

Figure 2.10: a) Resonant frequency as a function of waveguide height b) Resonant frequency as a function of ring width.

of the ring from 240 nm to 250 nm in steps of 1 nm. We also vary the width of the ring from 0.98 µm to 1.02 µm in steps of 10 nm. The radius of 70 µm of the ring was fixed while varying the width. Figure 2.10 shows the predicted variation in resonance frequency in water for small changes around a base geometry of height 250 nm and width 1 µm. The changes in resonant frequency have a slope of 149 GHz/nm for changes in the height of the resonator, and 14 GHz/nm for changes in the radius of the resonator. The azimuthal mode M is constant along the dotted lines in the figure, and increases by 1 for adjacent lines. As a consequence, we cannot determine if the two resonators have the same M.

Since one cannot determine M from the transmission spectrum, one must question whether the differences in the sensing and reference responses influence the sensitivity of the ring resonator platform. We have previously estimated the bulk sensitivity of our base geometry to be 72.7 nm RIU^{-1}. Figure 2.11 shows that despite variation in the geometrical parameters and the correspondingly

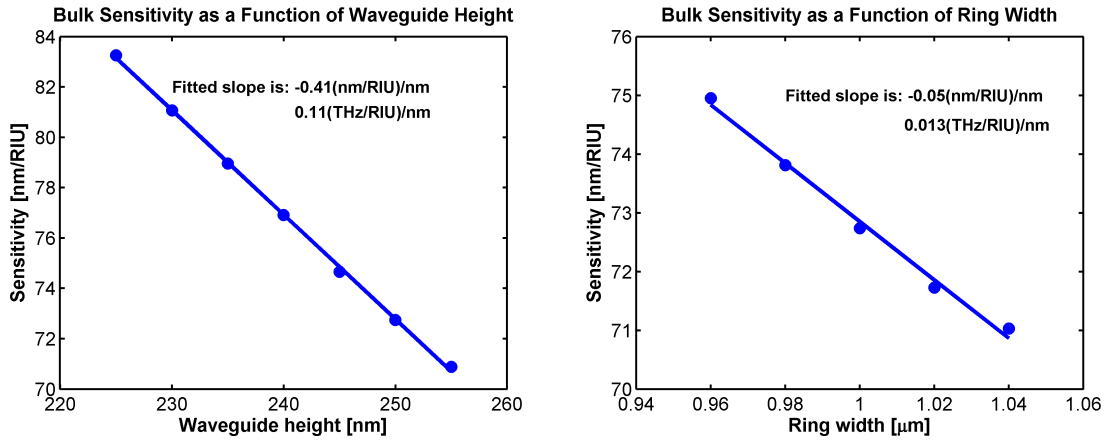

Figure 2.11: a) Sensitivity to bulk index of refraction changes as a function of ring height b) Sensitivity to bulk index of refraction changes as a function of ring width.

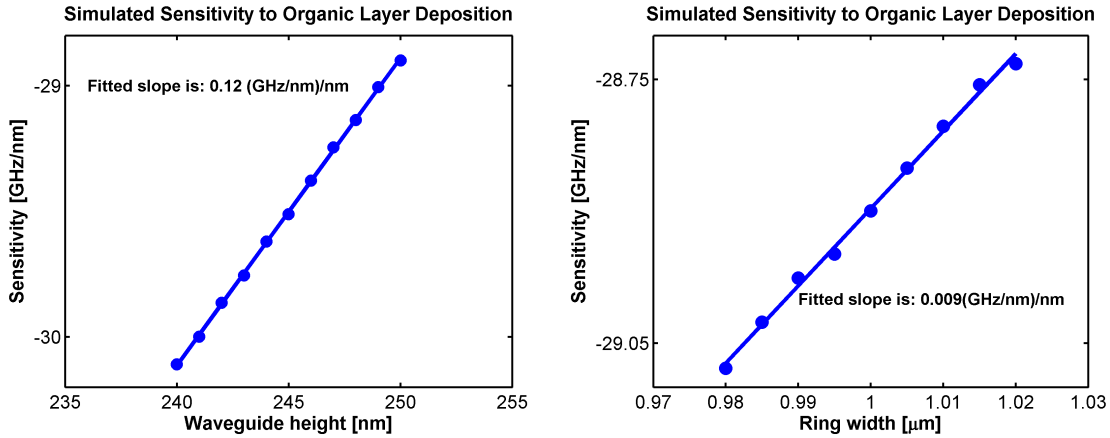

Figure 2.12: a) Sensitivity to surface sensing as a function of ring height b) Sensitivity to surface sensing of as a function of ring width.

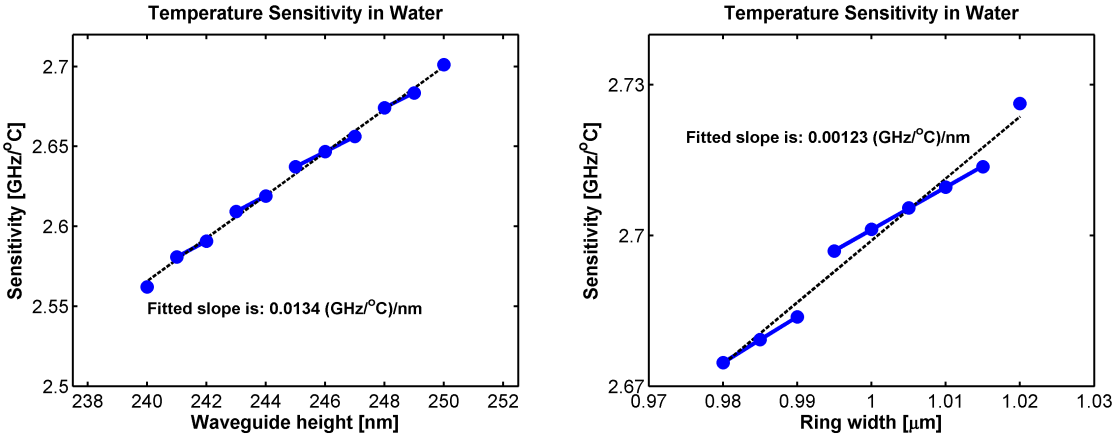

Figure 2.13: a) Temperature sensitivity as a function of waveguide height b) Temperature sensitivity as a function of ring width.

different M values, the sensitivity still changes linearly with resonator height and width. Setting an upper bound on the geometry variation of two adjacent rings of 5 nm for the height and 10 nm for the width, we derive an upper bound on the sensitivity variation for bulk refractive indexes of $2\,\mathrm{nm\,RIU^{-1}}$ and $0.5\,\mathrm{nm\,RIU^{-1}}$, respectively.

A similar analysis for the response to a layer of organic thickness, shown in Figure 2.12, yielded upper bounds of $0.6\,\mathrm{GHz\,nm^{-1}}$ and $0.09\,\mathrm{GHz\,nm^{-1}}$. The temperature response is well described by linear fits of sensitivity to changes in geometric parameters, as shown in Figure 2.13. The derived upper bounds are $0.06\,\mathrm{GHz\,°C^{-1}}$ and $0.01\,\mathrm{GHz\,°C^{-1}}$.

The above simulations confirm that small changes in the geometry due to fabrication variations will lead to similar responses in bulk and organic sensing, as well as temperature response.

2.4.3 Experimental setup

The setup consists of a 1064nm vertical-cavity surface-emitting (VCSEL) based optoelectronic linearly swept frequency laser that scans a frequency range of 400 GHz in a time span of 2 ms. The linear frequency sweep simplifies the identification and tracking of the resonant frequencies, and its high scan speed allows for high time resolution measurements. For a more detailed description of the laser, see [12]. The laser is coupled into the resonator chip from free space optics, and the output beam is aligned to a photodetector connected to an oscilloscope (Figure 2.14). The resonant frequencies are identified by fitting two Lorentzian lineshapes to the transmission spectrum. The resonator chip itself is comprised of the silicon nitride wafer, in which the ring resonators are etched, and a polydimethylsiloxane (PDMS) chip on top, with defined flow channels for liquid delivery. The flow platform has four inlets from which we can select two by using elastomeric valves, each being delivered to the reference and sensing resonator in the common flow channel, and obey laminar flow conditions. We will describe the flow design and mode of operation of the microfluidics in more detail in Chapter 3. The chip is attached to a copper block using adhesive transfer tape. The copper block contains a thermistor that records the temperature of the stage and a Peltier thermo-electric cooler through which the temperature of the stage is computer-controlled and monitored.

To exemplify the achievement of laminar flow, we introduce two colored dyes in the common channel. In Figure 2.15 we show the separation of the two streams.

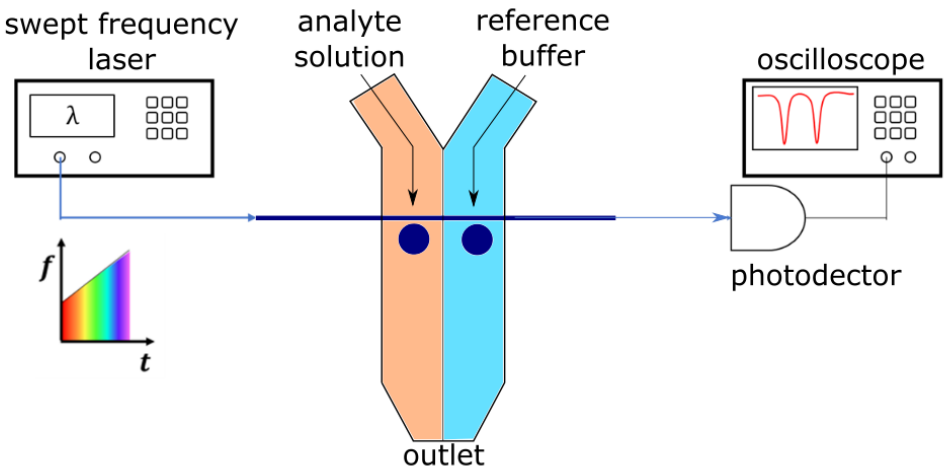

Figure 2.14: A swept frequency laser interrogates the resonant frequencies of the two ring resonators.

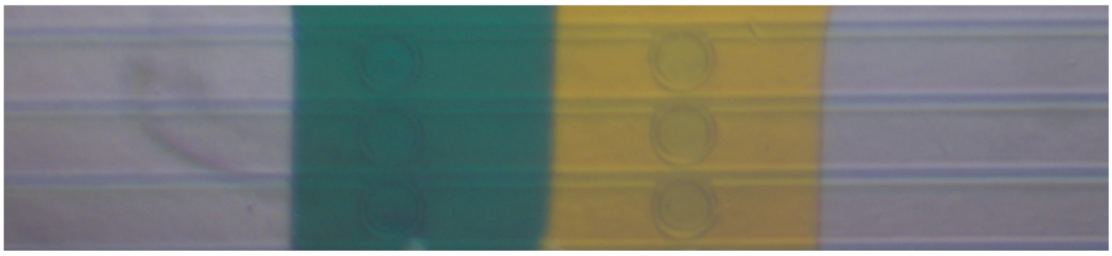

Figure 2.15: Exemplification of the co-laminar flow with green and yellow dyes.

2.4.4 Experimental results

2.4.4.1 Bulk refractive index experiments

To demonstrate the sensing ability of our platform and determine its response to bulk refractive index changes, we perform sensing experiments with a range of concentrations of sodium chloride (NaCl), with the temperature of the chip fixed at $T = 26\,^{\circ}\mathrm{C}$. Briefly, solutions of DI water are introduced from two inlets over the sensing and reference resonators to establish a baseline. Then, a solution of NaCl is introduced from one of the inlets over the sensing resonator. The last step is to reestablish the baseline, by flowing DI water over the sensing resonator. Differential shifts for concentrations of 2.5 mM, 5 mM, 10 mM, and 40 mM are displayed in Figure 2.16. Between five and ten cycles of the same NaCl concentration are recorded. We determine a bulk index sensitivity of $72.6 \pm 0.3\mathrm{nm\,RIU^{-1}}$, or, alternatively, $19.2 \pm 0.1\mathrm{THz\,RIU^{-1}}$. These values are in excellent agreement with our simulated values of $72.7\,\mathrm{nm\,RIU^{-1}}$ and $-19.3\,\mathrm{THz\,RIU^{-1}}$.

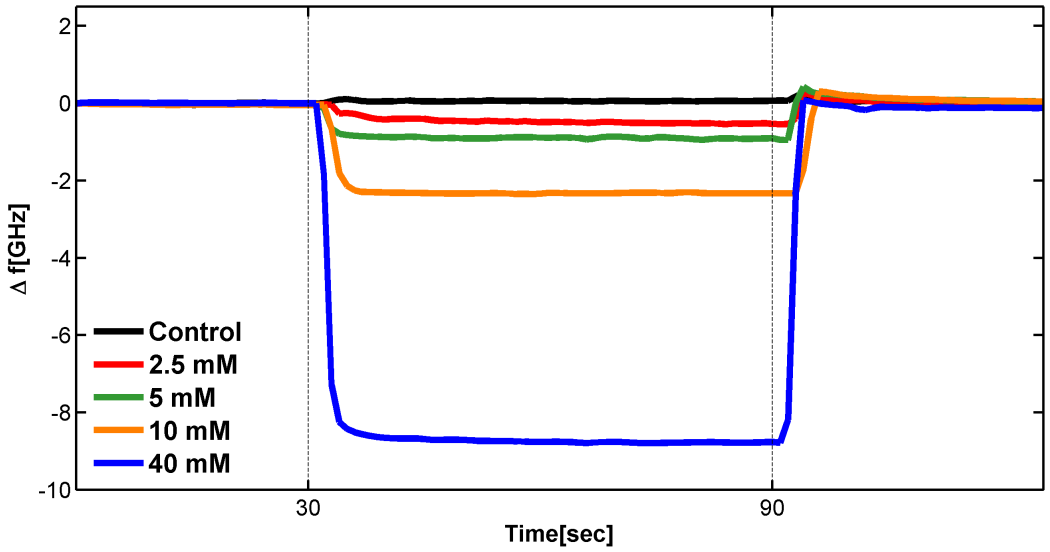

Figure 2.16: a) Bulk sensing data showing the differential response of the resonators to different concentrations of NaCl.

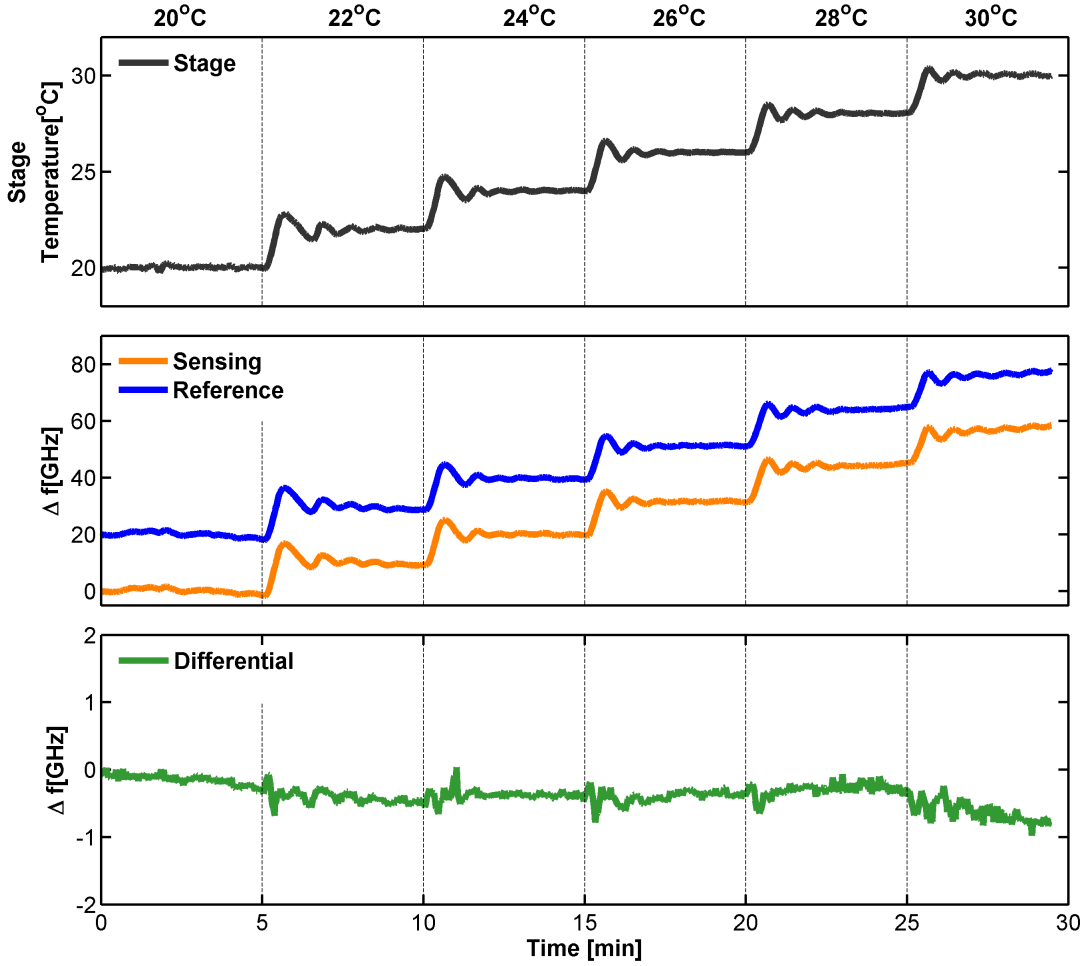

Figure 2.17: Temperature calibrations in ethanol. The first subplot shows the actual temperature of the stage as recorded by the thermocouple. The second subplot shows the response of the sensing and reference resonators. The reference resonator response has been shifted upwards by 20 GHz for ease of visualization. The third subplot shows the differential signal. Note that the scale for the differential signal is 20 times smaller than that for the individual responses.

2.4.4.2 Temperature calibration experiments

The temperature of the stage was controlled and monitored using a temperature controller (Newport, LDC-3724). The temperature was changed in increments of $\Delta t = 2\,^{\circ}\mathrm{C}$, after which the new temperature was maintained for 5 min or 6 min, to allow the resonator response to stabilize. Oscillations in both the temperature and resonator responses result from slow feedback in the temperature stabilization.

Beginning with a solution of ethanol, the temperature was varied from 20 °C to 30 °C in 2 °C steps, for a temperature window of 10 °C and total experiment duration of 30 min. The results are shown in Figure 2.17. The individual resonator responses follow the stage temperature increase,

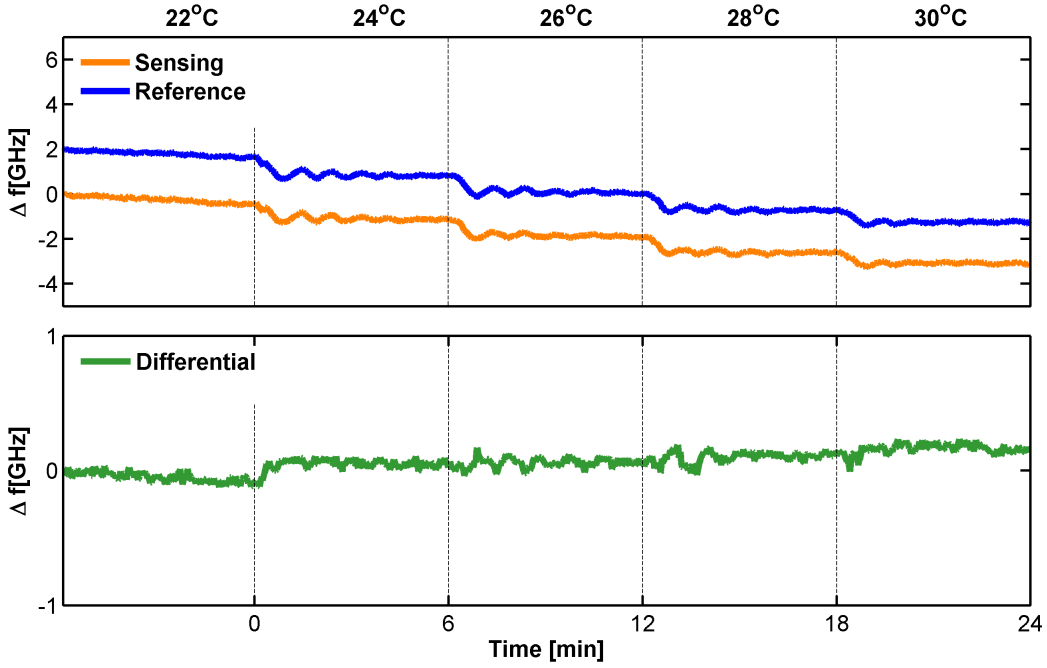

Figure 2.18: Temperature calibrations in water. The first subplot shows the response of the sensing and reference resonators. The reference resonator response has been shifted upwards by 2 GHz for ease of visualization. The second subplot shows the differential signal, on a scale 6 times smaller.

and show similar trends, whereas the differential signal is mostly insensitive to the temperature fluctuations. The standard deviation of the differential signal is $\sigma = 183\,\text{MHz}$. Least squares fitting of the individual response to the stage temperature, T_s, reveals the temperature sensitivity of each resonator, R_i, to the form:

$$R_i \approx a_i \times T_s + b_i,$$

which yields $a_1 = a_2 = 6.1\,\text{GHz}/^\circ\text{C}$ for both resonators in ethanol. These values are higher than the simulated value in the previous section of $4.5\,\text{GHz}/^\circ\text{C}$.

Two temperature calibration experiments were also performed in water. In the first experiment, shown in Figure 2.18, the temperature was ramped up and down between 26 °C and 30 °C. We again fit the recorded stage temperature to each resonator response and we extract sensitivities of $a_1 = a_2 = -0.5\,\text{GHz}/^\circ\text{C}$. The standard deviation of the differential signal is $\sigma = 175\,\text{MHz}$. A second experiment in water involves ramping the temperature from 22 °C to 32 °C, with similar results, shown in Figure 2.19. The extracted sensitivity is $a_1 = a_2 = -0.6\,\text{GHz}/^\circ\text{C}$. The simulated values for the temperature sensitivity in water are $-2.7\,\text{GHz}/^\circ\text{C}$, larger than the measured ones.

Lastly, an experiment in air, in which the temperature was ramped up and down between 26 °C and 30 °C, yielded the temperature sensitivities in air of $a_1 = -3.7\,\text{GHz}/^\circ\text{C}$ and $a_2 = -3.9\,\text{GHz}/^\circ\text{C}$.

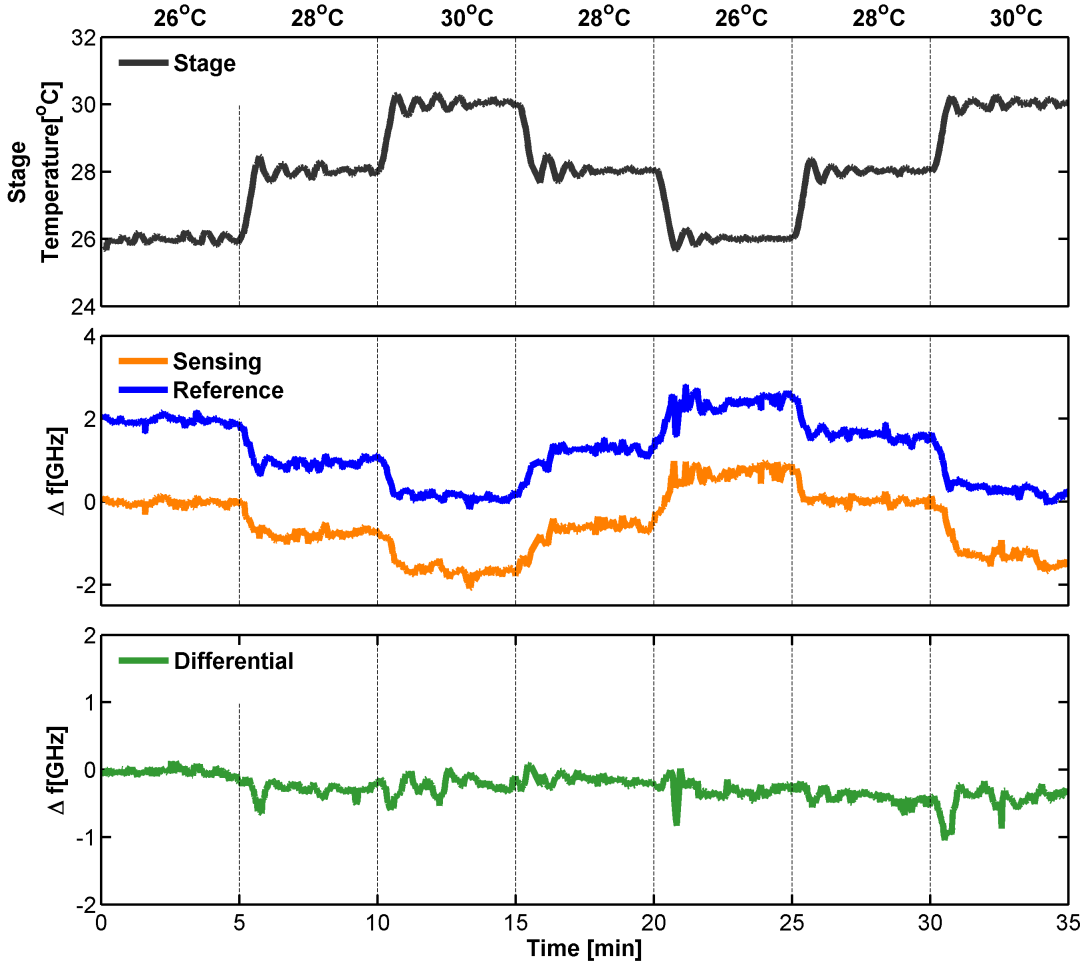

Figure 2.19: Temperature calibrations in water. The first subplot shows the stage temperature cycles. The second subplot shows the response of the sensing and reference resonators. The reference resonator response has been shifted upwards by 2 GHz. The third subplot shows the differential signal.

The measurement temperature sensitivities are not in agreement with the simulated values. A possible explanation is that the recorded stage temperature is not an accurate estimate of the temperature at the resonator since the introduced fluids are at room temperature, and they could lower the temperature experienced by the resonator. Despite this disagreement, the overarching conclusion is that the differential signal is insensitive to temperature variations in the three media, proving the viability and sensing capabilities of our platform.

The effect of temperature changes on the bulk sensing experiments was probed by sampling solutions of NaCl of concentrations 20 mM, 40 mM, 80 mM, and 160 mM into the dual laminar flow platform as the temperature of the stage was ramped up from 22 °C to 32 °C in steps of 2 °C. For each temperature, a sensing cycle is measured. Figure 2.20 shows the individual and differential

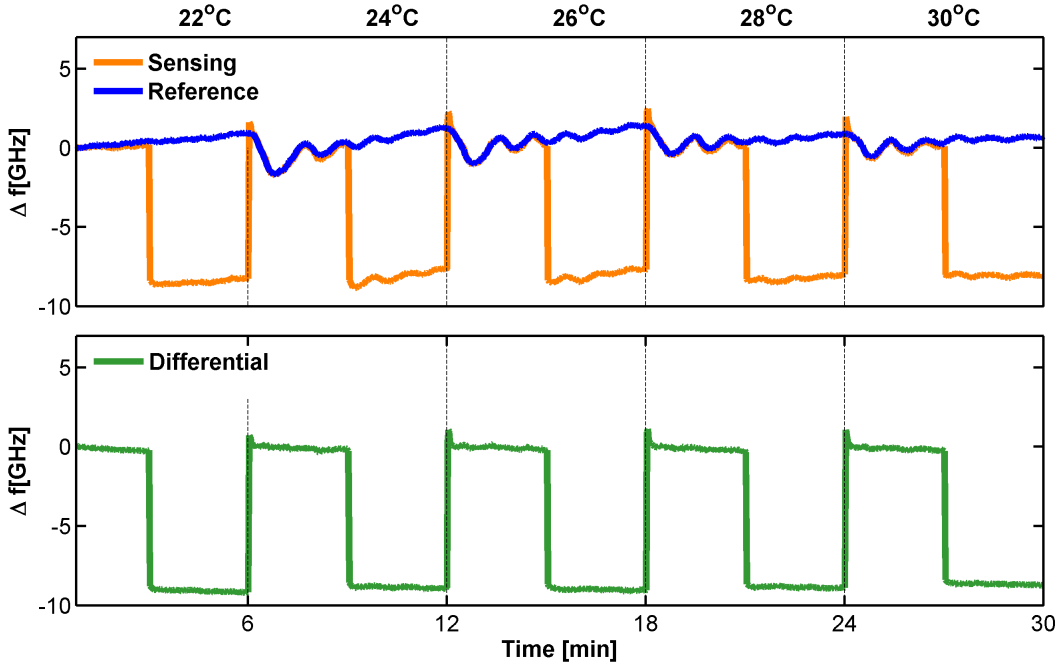

Figure 2.20: Resonator response to cycles of 40 mM NaCl in a temperature varying environment. Temperature shifts affect the individual resonator responses, but not the differential signal.

responses to a concentration of 40 mM of NaCl. The temperature variations are apparent in the individual resonator responses, but not the in differential signal. From similar experiments involving the four concentrations mentioned above, we extract a bulk sensitivity of $62.4 \pm 0.9\text{nm}\,\text{RIU}^{-1}$, or, alternatively, $17.0 \pm 0.2\text{THz}\,\text{RIU}^{-1}$. The standard deviation of the baseline signal is $\sigma_{\text{baseline}} = 80\,\text{MHz}$, which leads to a limit of detection $\text{LOD} = 3\sigma_{\text{baseline}}/S = 1.4 \times 10^{-5}\text{RIU}$.

2.4.4.3 Presssure calibration experiments

We investigate the response of the resonators to changes in the inlet pressure in steps of 14 kPa (2 psi) from 28 kPa (4 psi) to 56 kPa (8 psi). Each resonance shifts in response to the pressure change, but the differential signal shows minimal drift. We note the long-term transient of both resonators, which we will discuss in detail in Chapter 3. Overall the pressure shifts get reduced by an order of magnitude in the dual-laminar flow platform, as shown in Figure 2.21.

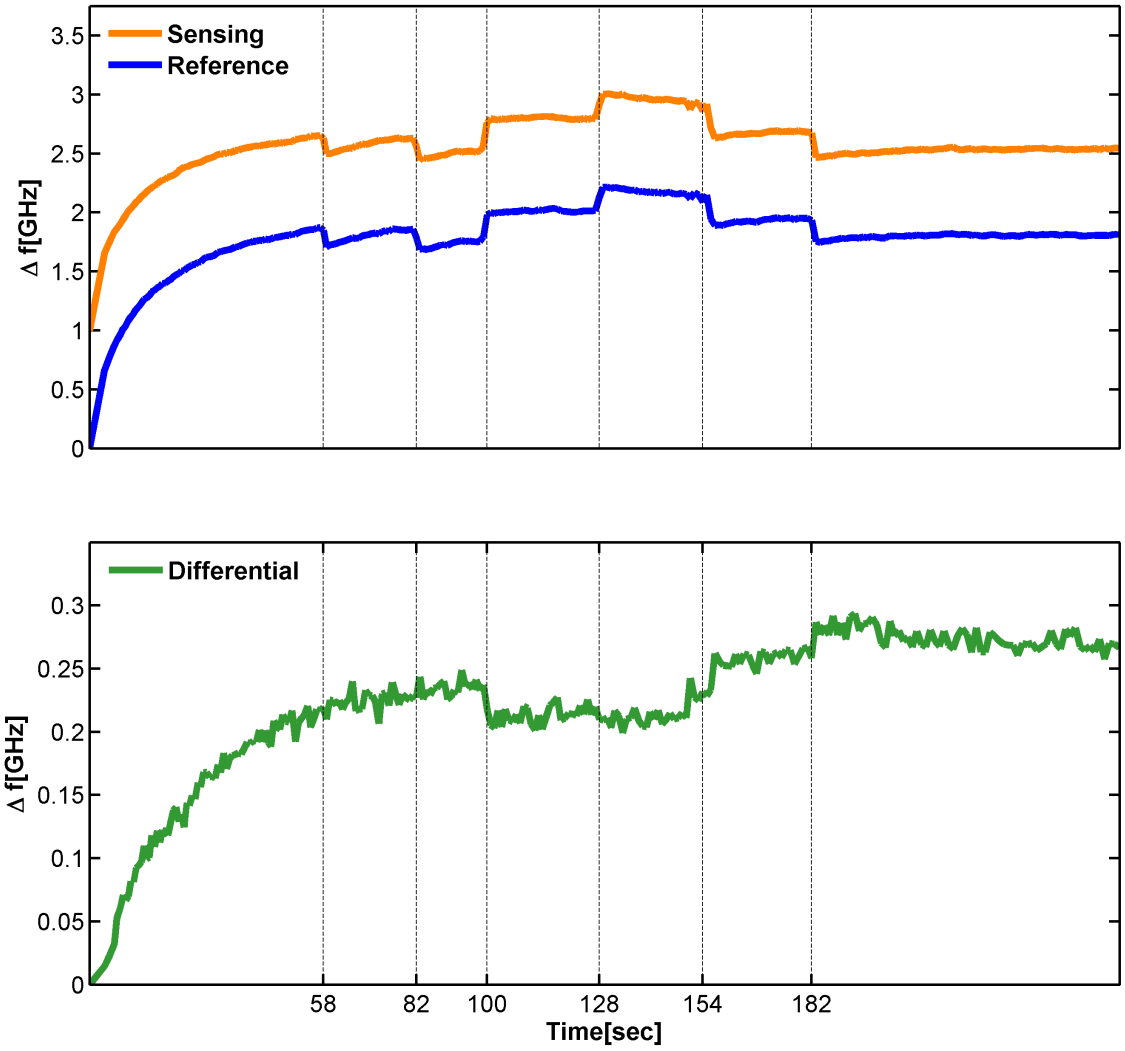

Figure 2.21: Resonator response to changes in inlet pressure in increments of Δp=14 kPa (2 psi).

2.4.5 Noise characterization using Allan variance

Allan deviation is a tool used for assessing the stability of oscillators. We propose using Allan deviation data to determine the integration time of the frequency signal which leads to the lowest noise in the system. If the integration time is too long, the signal is dominated by noise due to random walk processes. If the integration time is too short, the signal is dominated by white noise. By examining the Allan deviation, we will be able to identify the types of noises present on our platform, and derive an optimal signal integration time.

The modified Allan variance is defined as:

$$\sigma_y^2(n\tau) = \frac{1}{2}\left\langle \left[\frac{1}{n} \sum_{i=0}^{n-1} (f_{i+n} - f_i) \right]^2 \right\rangle,$$

where τ is the time interval between successive sample points, n is the number of samples averaged, and f_i the response of the resonator at time $i\tau$.

We plot the Allan deviation for integration times from 10 s to 30 min, corresponding to typical durations for an experiment. For the results to be statistically significant, data were collected for at least 4 h, a factor of 8 higher than our maximum integration time. To compare the noise in our dual laminar platform to that in a platform in which the reference resonator is covered, we fabricated devices in which the reference resonator is covered by a 6 µm layer of SU-8 (shown in Figure 2.22).

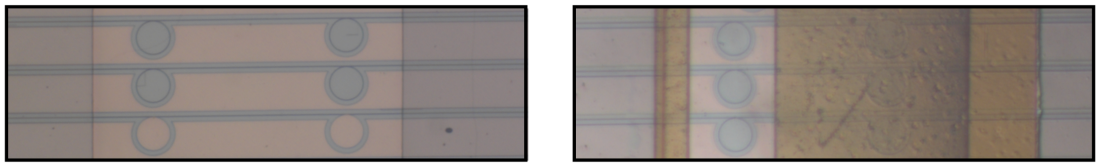

Figure 2.22: a) Dual-flow platform. b) Covered reference ring platform.

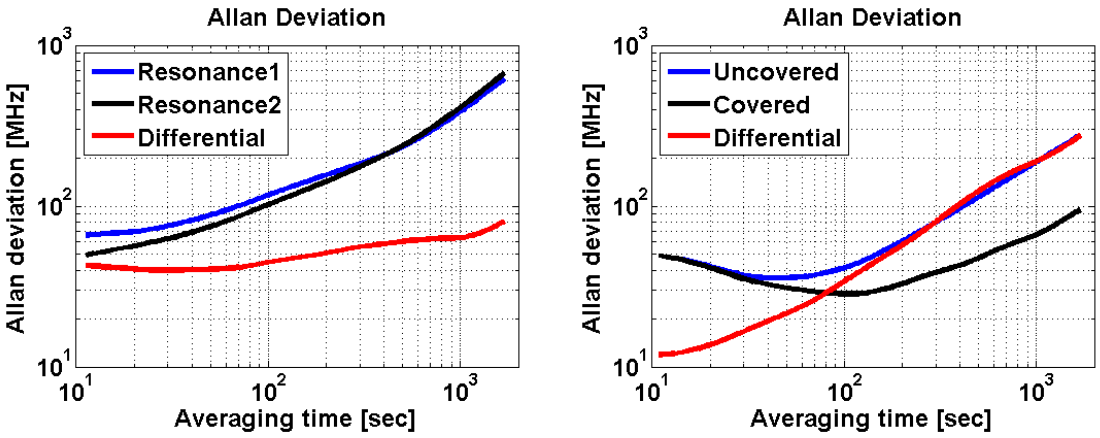

Figure 2.23: a) Allan deviation in dual flow platform. b) Allan deviation in covered platform.

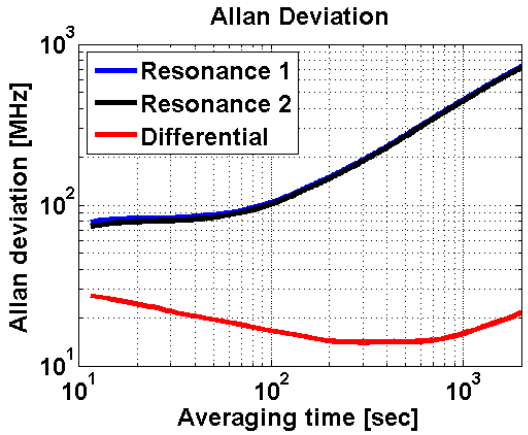

Figure 2.24: a) Allan deviation in air.

Figure 2.23 shows Allan deviation plots for each individual resonator, and for the differential signal, in both the laminar flow platform and the covered resonator platform. Experiments were performed with water flowing inside the channel. The individual resonators have similar noise curves in the dual laminar flow platform, and their differential signal is fairly steady, not exceeding 80 MHz for the entire time integration range. The noise in the differential signal is much lower than in the individual resonators. In contrast, the noise curves for the sensing resonator, which is exposed to the flow, and the covered resonator in the covered platform begin diverging after 30 s. The Allan deviation is lower in the covered resonator than the sensing resonator, because the covered resonator is not exposed to the temperature and pressure fluctuations of the fluid flow. As a result, the noise in the differential signal in the covered platform increases rapidly. After 20 s the Allan deviation of the differential signal is similar to that of the sensing resonator, masking the benefits of using a reference resonator. We conclude that resonators exposed to the fluid flow exhibit higher noise levels than covered resonators, but, by employing a differential measurement scheme, the overall noise in the system is greatly reduced. Figure 2.24 shows the Allan deviation in air in the laminar flow platform. As before, the individual resonator noise curves are very similar, and the Allan deviation for the differential signal is reduced. The overall noise in the platform exposed to air is smaller than in the same platform exposed to water flow, and does not exceed 20 MHz.

Bibliography

[1] D. J. Segelstein, "The complex refractive index of water," Master's thesis, University of Missouri-Kansas City, 1981.

[2] S. Kedenburg, M. Vieweg, T. Gissibl, and H. Giessen, "Linear refractive index and absorption measurements of nonlinear optical liquids in the visible and near-infrared spectral region," *Opt. Mater. Express*, vol. 2, pp. 1588–1611, Nov 2012.

[3] M. Iqbal, M. A. Gleeson, B. Spaugh, F. Tybor, W. G. Gunn, M. Hochberg, T. Baehr-Jones, R. C. Bailey, and L. C. Gunn, "Label-free biosensor arrays based on silicon ring resonators and high-speed optical scanning instrumentation," *IEEE Journal of Selected Topics in Quantum Electronics*, vol. 16, pp. 654–661, May 2010.

[4] T. Claes, J. G. Molera, K. D. Vos, E. Schacht, R. Baets, and P. Bienstman, "Label-free biosensing with a slot-waveguide-based ring resonator in silicon on insulator," *IEEE Photonics Journal*, vol. 1, pp. 197–204, Sept 2009.

[5] K. D. Vos, I. Bartolozzi, E. Schacht, P. Bienstman, and R. Baets, "Silicon-on-insulator microring resonator for sensitive and label-free biosensing," *Opt. Express*, vol. 15, pp. 7610–7615, Jun 2007.

[6] C. A. Barrios, K. B. Gylfason, B. Sánchez, A. Griol, H. Sohlström, M. Holgado, and R. Casquel, "Slot-waveguide biochemical sensor," *Opt. Lett.*, vol. 32, pp. 3080–3082, Nov 2007.

[7] D.-X. Xu, M. Vachon, A. Densmore, R. Ma, A. Delâge, S. Janz, J. Lapointe, Y. Li, G. Lopinski, D. Zhang, Q. Y. Liu, P. Cheben, and J. H. Schmid, "Label-free biosensor array based on silicon-on-insulator ring resonators addressed using a wdm approach," *Opt. Lett.*, vol. 35, no. 16, pp. 2771–2773, 2010.

[8] C.-Y. Chao, W. Fung, and L. J. Guo, "Polymer microring resonators for biochemical sensing applications," *IEEE Journal of Selected Topics in Quantum Electronics*, vol. 12, pp. 134–142, Jan 2006.

[9] A. Yalcin, K. C. Popat, J. C. Aldridge, T. A. Desai, J. Hryniewicz, N. Chbouki, B. E. Little, O. King, V. Van, S. Chu, D. Gill, M. Anthes-Washburn, M. S. Unlu, and B. B. Goldberg, "Optical sensing of biomolecules using microring resonators," *IEEE Journal of Selected Topics in Quantum Electronics*, vol. 12, pp. 148–155, Jan 2006.

[10] G. A. Rodriguez, S. Hu, and S. M. Weiss, "Porous silicon ring resonator for compact, high sensitivity biosensing applications," *Opt. Express*, vol. 23, pp. 7111–7119, Mar 2015.

[11] I. Goykhman, B. Desiatov, and U. Levy, "Ultrathin silicon nitride microring resonator for biophotonic applications at 970 nm wavelength," *Applied Physics Letters*, vol. 97, no. 8, 2010.

[12] J. B. Sendowski, *On-chip integrated label-free optical biosensing*. PhD thesis, California Institute of Technology, 2013.

[13] M. Oxborrow, "How to simulate the whispering-gallery modes of dielectric microresonators in FEMLAB/COMSOL," in *Lasers and Applications in Science and Engineering*, pp. 64520J–64520J, International Society for Optics and Photonics, 2007.

[14] M. Oxborrow, "Traceable 2-D finite-element simulation of the whispering-gallery modes of axisymmetric electromagnetic resonators," *Microwave Theory and Techniques, IEEE Transactions on*, vol. 55, no. 6, pp. 1209–1218, 2007.

[15] J. R. Zhao, X. G. Huang, and J. H. Chen, "A Fresnel-reflection-based fiber sensor for simultaneous measurement of liquid concentration and temperature," *Journal of Applied Physics*, vol. 106, no. 8, 2009.

[16] H. Su and X. G. Huang, "Fresnel-reflection-based fiber sensor for on-line measurement of solute concentration in solutions," *Sensors and Actuators B: Chemical*, vol. 126, no. 2, pp. 579 – 582, 2007.

[17] X. Zhao, J. M. Tsai, H. Cai, X. M. Ji, J. Zhou, M. H. Bao, Y. P. Huang, D. L. Kwong, and A. Q. Liu, "A nano-opto-mechanical pressure sensor via ring resonator," *Opt. Express*, vol. 20, pp. 8535–8542, Apr 2012.

[18] K. B. Gylfason, C. F. Carlborg, A. Kaźmierczak, F. Dortu, H. Sohlström, L. Vivien, C. A. Barrios, W. van der Wijngaart, and G. Stemme, "On-chip temperature compensation in an integrated slot-waveguide ring resonator refractive index sensor array," *Opt. Express*, vol. 18, pp. 3226–3237, Feb 2010.

Chapter 3

On-chip valve technology for reducing response time

This chapter presents and characterizes a design for the fluidic network that delivers the solutions to the resonators, with a focus on reducing the response time of the platform. The channels that encapsulate the ring resonators are made of polydimethylsiloxane (PDMS), an elastomer that has been widely used in microfluidics because it is easily moldable, low-cost, gas-permeable and transparent. Most importantly, PDMS is excellent for rapid prototyping of new designs and has the advantage that elastic valves can be manufactured using a bi-layer design [1, 2]. Other materials from which fluidic chips are fabricated include polymethylmethacrylate (PMMA) and Mylar plastic, but, due to their rigidity, they cannot support on-chip valves, and their fabrication is complex. Designs of the fluidic network require careful choices of the dimensions of the channel, the driving force of the flow, and the method of switching the flow that is delivered to the resonator between a buffer and the analyte of interest. The switching method strongly influences the response time of the system. The range of volumetric flow rates and channel dimensions are summarized in Table 3.1.

Syringe pumps that can operate in either the infusion or the withdrawal mode are commonly used to drive the flow to the resonator chip. In our first experiments, we also used programmable syringe pumps together with a three-way solenoid valve to drive the flow to the resonators, and to switch the fluid streams, as shown in Figure 3.1. Briefly, either one of the two top syringes can drive the flow over the sensing resonator, depending on the setting of the three-way solenoid valve. A third syringe pump containing buffer solution drives the flow over the reference resonator.

In the previous chapter we measured the resonator response to several salt concentrations and determined the sensitivity of the resonators to changes in the index of refraction of the upper cladding. Here we examine the resonator response transient and explore approaches to reducing the response time, using a single salt concentration. Figure 3.2 shows the differential response of

Material	Channel dimensions	Flow rates	Switching Mechanism	Reference
Mylar	175 µm × 500 µm	5, 10, 30 µl min^{-1}	robotic arm for plate aspiration	Iqbal et al [3]
PDMS	20 µm × 200 µm	10 µl min^{-1}	in-line injector valves	Gylfason et al. [4]
PDMS	50 µm × 200 µm	5 µl min^{-1}	-	DeVos et al [5]
PDMS	-	10 µl min^{-1}	manual	Grist et al [6]

Table 3.1: Various geometries of the fluidic channels and flow characteristics employed by different groups.

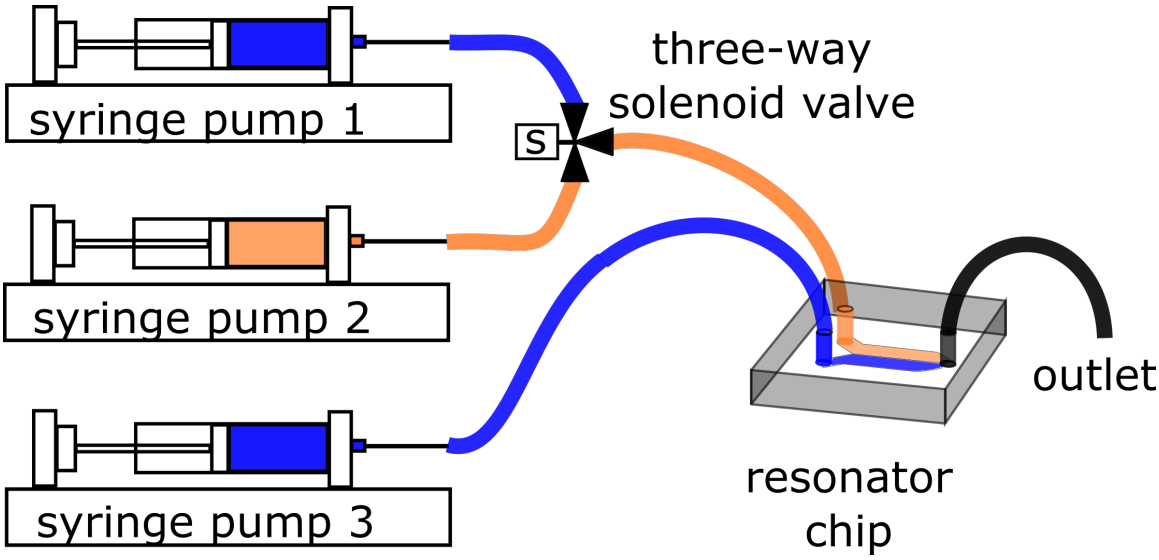

Figure 3.1: Initial setup that includes syringe pumps and a three-way solenoid valve to control the flow to the resonator chip. Two syringe pumps containing the buffer (blue) and the analyte of interest (orange) are connected to the three-way solenoid valve, which is computer-controlled. We can switch the flow from either of the first two syringe pumps and direct it to the sensing resonator. A third syringe pump with buffer (blue) is continuously flowing to the reference resonator.

the dual-laminar flow platform when a 172 mM NaCl solution is introduced using the syringe pump setup. First, we flow deionized (DI) water over both the sensing and reference resonators for 15 min to establish the baseline signal. Then, we switch the flow at the three-way solenoid valve from water to salt. Two characteristics of the response to the switch are apparent in Figure 3.2: first, there is a delay between the time the switch occurs at the three-way solenoid valve and that when a change in the resonator response is first detected. This delay time of $t_{\text{delay}} \approx 10$ min results from the transport time inside the connecting tubing lines. Second, a transient response is observed before the signal saturates, owing to mixing in the Tygon tubing and in the dead volume of the solenoid valve, and to the finite rate of diffusional mass transport to the boundary of the channel. Even after flowing the salt solution for 60 min, the response barely reaches its saturation level. If we fit the response curve to a decaying exponential, we obtain a transient decay time of $t_{\text{transient}} \approx 8$ min. After 60 min of

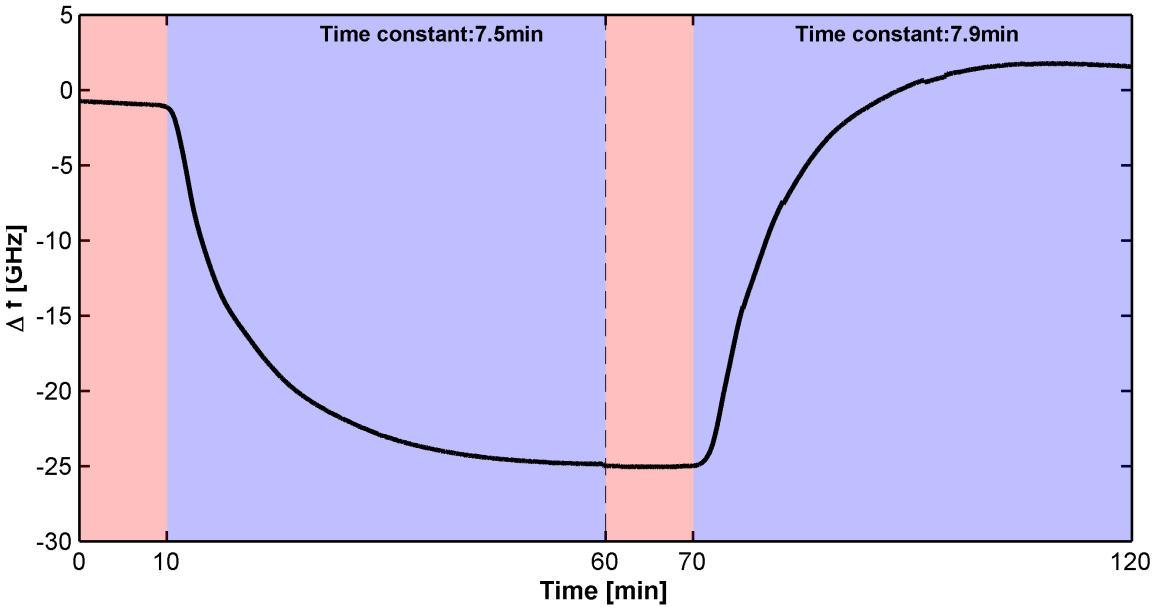

Figure 3.2: Salt sensing using solenoid and syringe pumps. The areas shaded in red represent the delay between the switch of the flow at the three-way solenoid valve and the presence of a change in the resonator response. The areas shaded in blue represent the transient phase of the response.

flowing salt, we re-establish the baseline by switching the sensing flow to water. We notice a similar t_{delay} and a $t_{\text{transient}}$ in re-establishing the baseline. A theoretical model that predicts the observed behavior of the response in this setup is presented at the end of the chapter.

Due to these delays and transient times, a bulk sensing experiment aimed at measuring a given concentration requires a few hours of data collection. To reduce the response time, we must reduce the dead volume in the flow system. To that end, we introduce a microfluidic platform in which the switching of the flows happens immediately upstream of the common resonator channel, on the same chip as the rings. This is achieved by using two-layer microfluidic chips with integrated elastomeric valves. Briefly, the elastomeric valves are channels in the top PDMS layer that expand when pressurized, restricting the flow in any channel in the bottom layer directly below and perpendicular to the valve. The top of bottom channel is rounded in the crossing zone to allow a complete seal. The top layer is referred to as the "control layer", whereas the bottom layer is referred to as the "flow layer." The thickness of the membrane between the two perpendicular channels is critical to the function of the valve. If the membrane is too thin, it will break under the fluid pressure, but if it is too thick, it will not deform enough to completely seal the flow channel. The choice of which control channel is pressurized can be determined using the manifold setup shown in Figure 3.3

The fabrication of the bi-layer PDMS chips with valves is described in the Appendix. Briefly, SU-8 molds are fabricated by photolithography from transparencies, with the rounded channel areas at the crossings fabricated from AZ50XT photoresist that are produced by annealing at 180 °C to

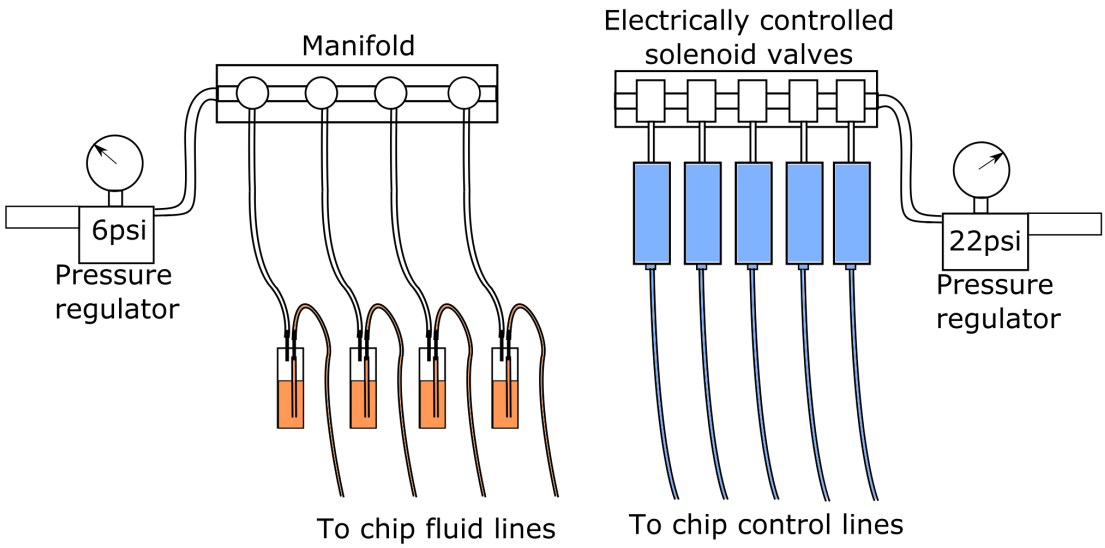

Figure 3.3: A schematic diagram of the fluidic control of the solutions delivered to the PDMS chip. Two regulators control the pressures for the control and flow layer. The control layer tubing is connected to a solenoid manifold that turns the valve for each control channel on or off.

reflow the polymer with a smooth fillet. However, in the first design used, a slight backflow into the adjacent channels was observed (see Figure 3.4). Therefore, our second microfluidic design has valves right at the T-junction of two channels. The final design, shown in Figure 3.5, has four inlets that are pressurized at $p = 34\,\text{kPa}$ (5 psi) and that are loaded with different solutions. Inlets 1 and 2 are designed to flow over the sensing resonator, while inlets 3 and 4 pass over the reference resonator. A common outlet channel also includes a valve that both improves fluidic control, and facilitates the removal of bubbles that are stuck inside the device. Since PDMS is air permeable, we eliminate bubbles by closing the outlet valve and pressurizing the channel. In a matter of minutes, the air diffuses through the PDMS. Bubbles are particularly harmful since they distort the laminar flow and can contaminate the reference resonator, especially during organic layer deposition. Incorporating a bubble removal mechanism is essential since they are unavoidable when loading the solutions into the chip for the first time. Each inlet has a corresponding valve that either allows or restricts the flow in that inlet. Typical pressures for the control valves are 137-165 kPa (20-24 psi).

3.1 Response time with on-chip valves

Figure 3.6 illustrates the three stages of a typical experiment: (i) setting up the baseline; (ii) introducing the analyte over the sensing ring; and (iii) re-establishing the baseline. The reference buffer is loaded to inlets 1, 3, and 4, while the analyte is loaded into inlet 2. The baseline is

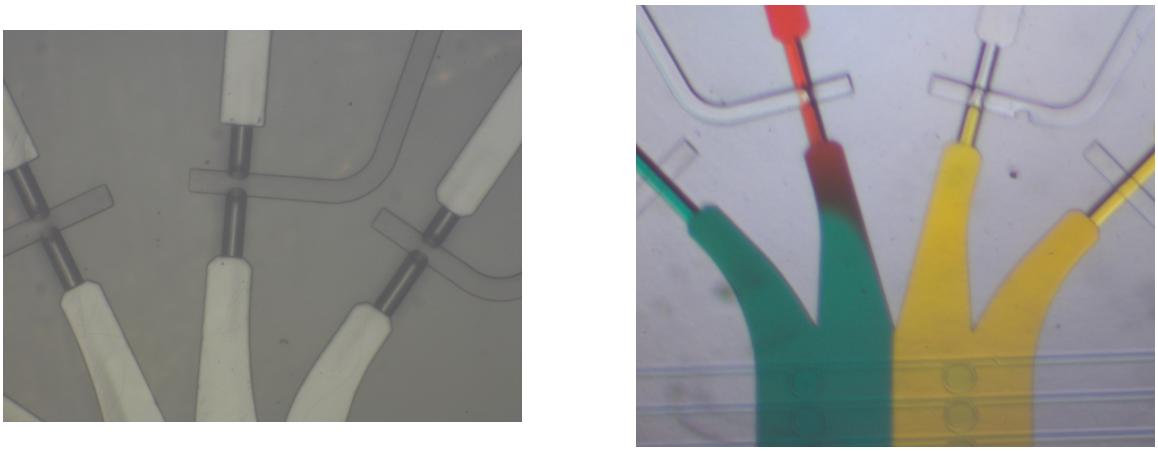

Figure 3.4: a) Closed control valves for three out of the four inlets. b) Backflow into adjacent channels.

established by flowing DI water from inlet 1 for the sensing ring and from either inlet 3 or inlet 4 for the reference ring. In the configuration shown in Figure 3.6, the initial baseline is determined using flow from inlets 1 and 4, while inlets 2 and 3 are closed. In the next step, the flow to the sensing resonator is switched from inlet 1 to inlet 2, which introduces the analyte of interest. In terms of the reference flow, we can continue using the buffer flow from inlet 3, or we can introduce buffer solution from inlet 4. We will later show that there are differences in the response signal of the resonators depending on the choice of inlets for the buffer flow. The individual responses of the rings as well as their differential signal response to a concentration of salt of 40 mM is presented in the same figure to exemplify a typical experiment. The response of the platform to a concentration of 160 mM NaCl is shown in Figure 3.7. The total duration of the experiment is 120 s, a factor of 60 shorter than the 120 min experiment time in the syringe pump/three-way valve platform, shown in Figure 3.2. The delay time $t_{\text{delay}} \approx 1\,\text{s}$ and $t_{\text{transient}} \approx 7\,\text{s}$. The large improvement in sensing time is due to the on-chip flow switching design.

The flow inside the elastomeric chip is influenced by the channel geometry parameters, and the pressure that drives the fluid flow. Fluidic networks obey the Hagen-Poiseuille equation, a relation similar to Ohm's law for electrical circuits: $Q = \Delta P/R$, where ΔP is the pressure difference across the channel, Q is the volumetric flow rate, and R is the fluidic resistance of the channel. The resistance is defined as:

$$R = \frac{128\eta L}{\pi D_h^4},$$

where η is the dynamic viscosity of the liquid, L is the length of the channel and D_h is the hydraulic diameter of the channel. The hydraulic diameter is given by $D_h = 4A/P$, where A represents the wetted area of the channel and P the wetted perimeter. For a cylindrical channel, the hydraulic diameter D_h is the same as the pipe diameter, and for a rectangular channel of width w and height

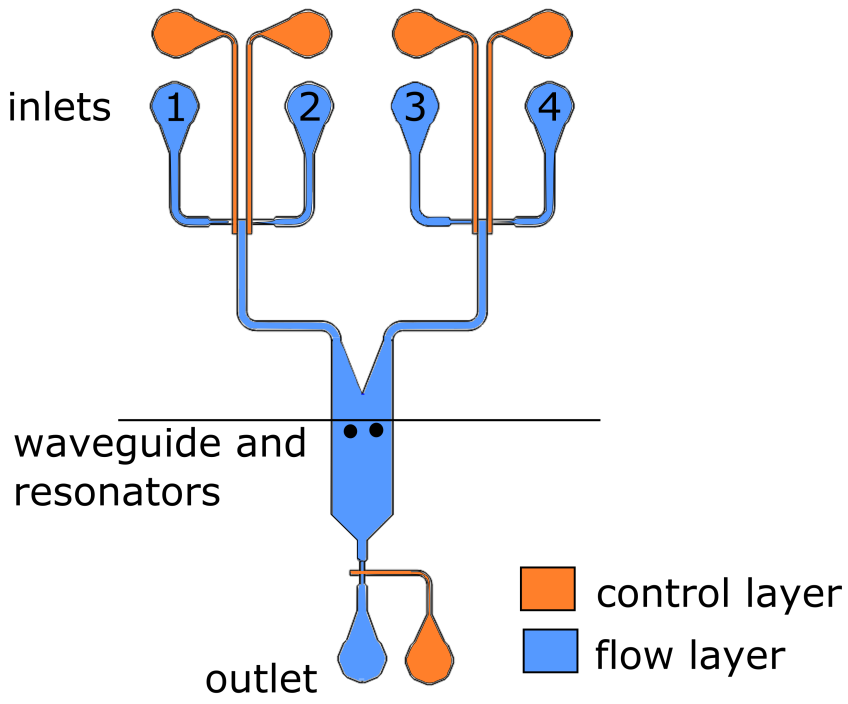

Figure 3.5: Schematic of the two-layer microfluidic chip. The control layer (in orange), is situated on top of the flow layer (in blue). The four inlets of the flow layer are labeled from 1-4. We can introduce a solution at either one, and either allow or restrict the flow using the corresponding control layer channel and associated valve.

h, and in the limit of $w \gg h$, $D_h \approx 2h$. In the fluidic circuit, shown in Figure 3.3, we identify the following flow elements: Tygon tubing leading to the chip, the chip itself, and Tygon tubing leading to the waste reservoir. We will calculate all resistances in the circuit in order to determine their relative importance and the character of the flow. The Tygon tubing has an inner diameter of $d = 0.02\text{in} = 508\,\mu\text{m}$. The resistance for a $L = 1\,\text{m}$ length of Tygon tubing is:

$$R_{\text{Tygon}} = 6 \times 10^{11} \frac{\text{Pa}}{\text{m}^3\,\text{s}^{-1}}.$$

Next, we determine the resistance of the flow lines in the elastomeric chip. The channel geometry is complex, so instead of theoretical calculations, we simulate the flow inside the chip in COMSOL Multiplysics$^{\text{TM}}$ (with a height of $h = 20\,\mu\text{m}$ for a channel), and perform a parameter sweep on the pressure difference between the inlet and the outlet, recording the resulting volumetric flow rate. The channel resistance determined by fitting the simulation results over all pressure values

$$R_{\text{channel}} = 1.2 \times 10^{14} \frac{\text{Pa}}{\text{m}^3\,\text{s}^{-1}},$$

is two orders of magnitude higher than the Tygon tubing resistance. Since the two resistances are

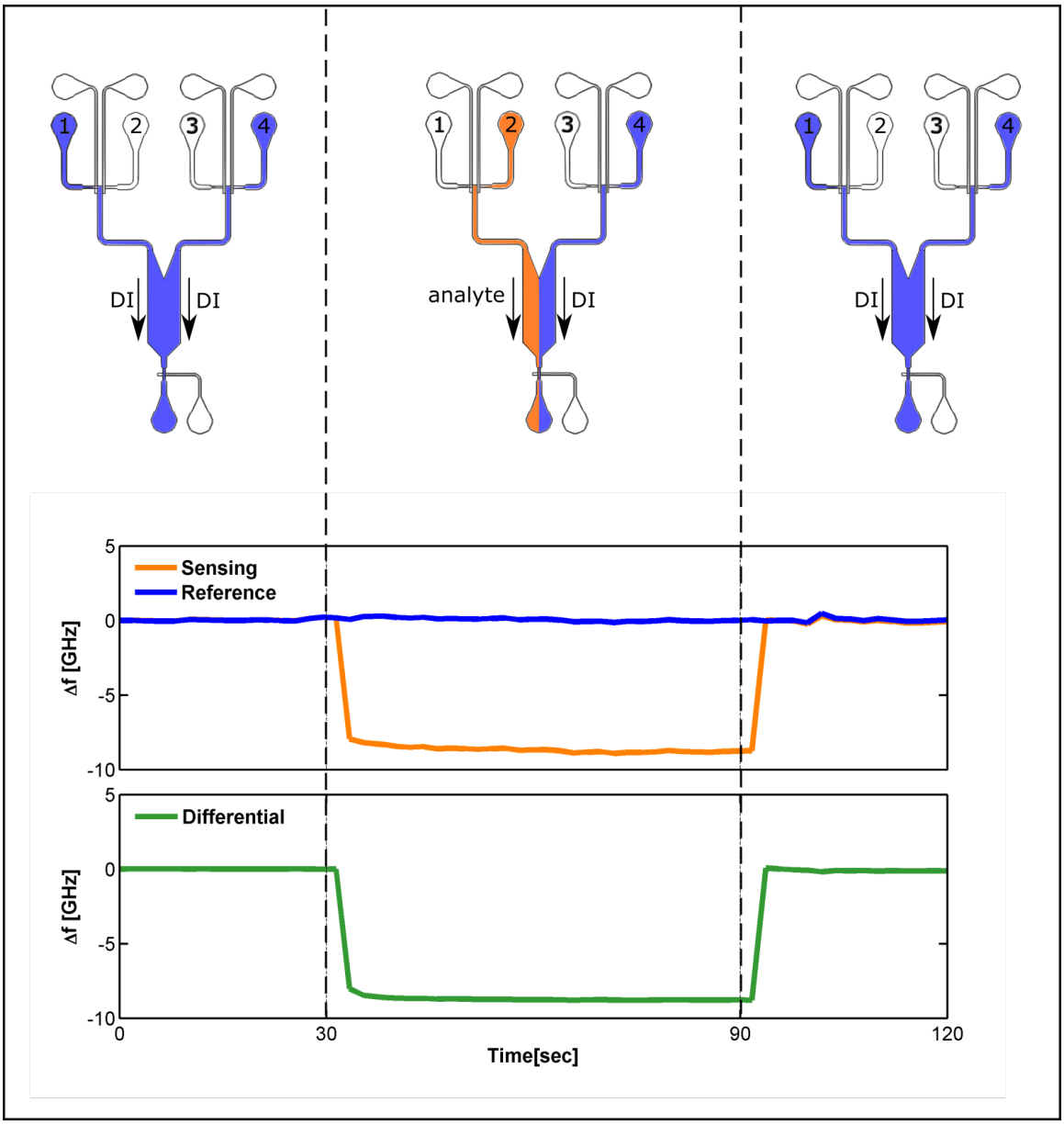

Figure 3.6: A typical sensing experiment involves three steps: setting up the baseline, introducing the analyte and re-establishing to the baseline.

connected in series, the equivalent hydrodynamic resistance is their sum: $R = R_{\text{Tygon}} + R_{\text{channel}}$. However, we can ignore effect of the resistance of the Tygon tubing since the channel resistance dominates. The volumetric flow rate in the fluidic network is, thus,

$$Q = \frac{\Delta P}{R} = 17\mu\text{l}\,\text{min}^{-1}.$$

The width of the channel is $W = 640\,\mu\text{m}$ and the height $H = 20\,\mu\text{m}$, so the average velocity in the proximity of the resonators is $v_{\text{ave}} = Q/(HW) = 22\text{mm}\,\text{s}^{-1}$. For a complete picture of the flow

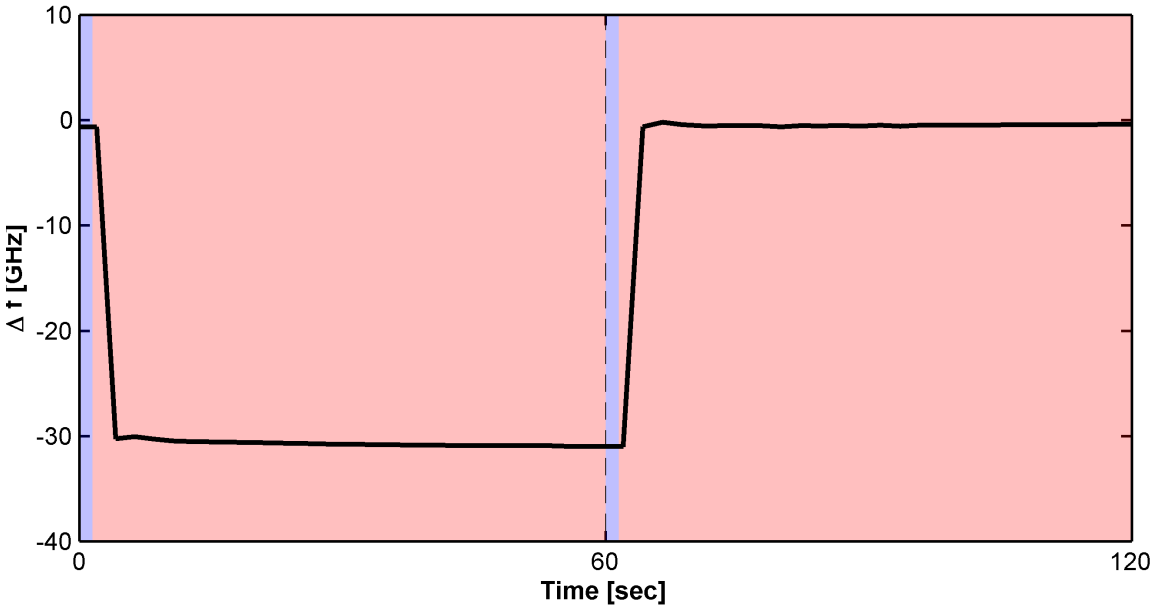

Figure 3.7: On-chip valve platform response to a concentration of 160 mM of NaCl.

Material	Resistance R	v_{ave}	Re	Pe
Tygon	6×10^{11}Pa/m^3 s^{-1}	1.4 mm s^{-1}	0.7	444
Channel	1.2×10^{14}Pa/m^3 s^{-1}	22 mm s^{-1}	0.9	550

Table 3.2: Flow characteristics in the on-chip switching platform.

inside the Tygon tubing and chip, we will calculate the Reynolds number and the Péclet number. The Reynolds number,

$$\mathrm{Re} = \frac{\rho v_{\mathrm{ave}} D_h}{\eta},$$

indicates the contribution of the inertial to viscous forces. The calculated Reynolds numbers are $\mathrm{Re}_{\mathrm{Tygon}} = 0.7$ and $\mathrm{Re}_{\mathrm{channel}} = 0.9$, indicating that the system operates in the laminar flow regime. The Péclet number,

$$\mathrm{Pe} = \frac{v_{\mathrm{ave}} D_h}{D},$$

represents the contribution of convection versus diffusion. For NaCl, the diffusivity $D_{\mathrm{NaCl}} = 1.5 \times 10^{-9}\mathrm{m}^2\,\mathrm{s}^{-1}$ [7], and $\mathrm{Pe}_{\mathrm{Tygon}} = 444$ and $\mathrm{Pe}_{\mathrm{channel}} = 550$, indicating that convection dominates over diffusion. The flow characteristics in both the Tygon tubing and microfluidic channel are summarized in Table 3.2.

3.2 Control experiments

To test that the response of the sensors is only sensitive to concentration changes, we study the response of the platform when we introduce DI water from inlet 2 instead of the analyte. Because

there are no concentration changes after the switch, we do not expect to detect any changes in the resonator response. However, we notice a periodic shift in the response correlated to the time of the inlet switching. The shift is on the order of a few GHz, and depends on the choice of inlets. Figure 3.8 shows transients when the inlets are switched from 1 and 4 to 2 and 3. Both resonators exhibit the transients, as does their differential signal. In Figure 3.9, the switching occurs from inlets 1 and 4 to 2 and 4. No switching transient is observed in the response of the resonator exposed to the continuous inlet 4 flow, but a long-term drift is apparent. The differential signal also exhibits a long-term drift superimposed to switching transients. The switching transients vary from chip to chip; they must be taken into account during post-processing of the data, and we do this by employing a matched-filter approach.

Since PDMS is an elastic material that deflects under stress, the applied pressure of the fluid flow may deform the microfluidic channel. Since the fluidic resistance of the channel scales as the height cubed, changes in the the channel height will results in large changes of pressure and flow rate. For example, syringe pumps have been shown to induce pressure oscillations in elastic channels due to mechanical oscillations driven by the stepper motor periodicity [8].

Deformations of shallow microfluidic channels have been studied by Gervais et. al [9]. They found that, for a given pressure drop, flow rates are much higher in deformed channels than rigid channels, and that flow rates and pressures do not vary linearly in these geometries. They suggest that the effects on flow rates should be considered when the dimensionless quantity $(\Delta PW)/(EH) \gg 0$, where ΔP is the magnitude of the pressure drop, E is the elastic Young modulus of PDMS, and H and W are the channel height and width. The elastic modulus of PDMS depends on the base:curing

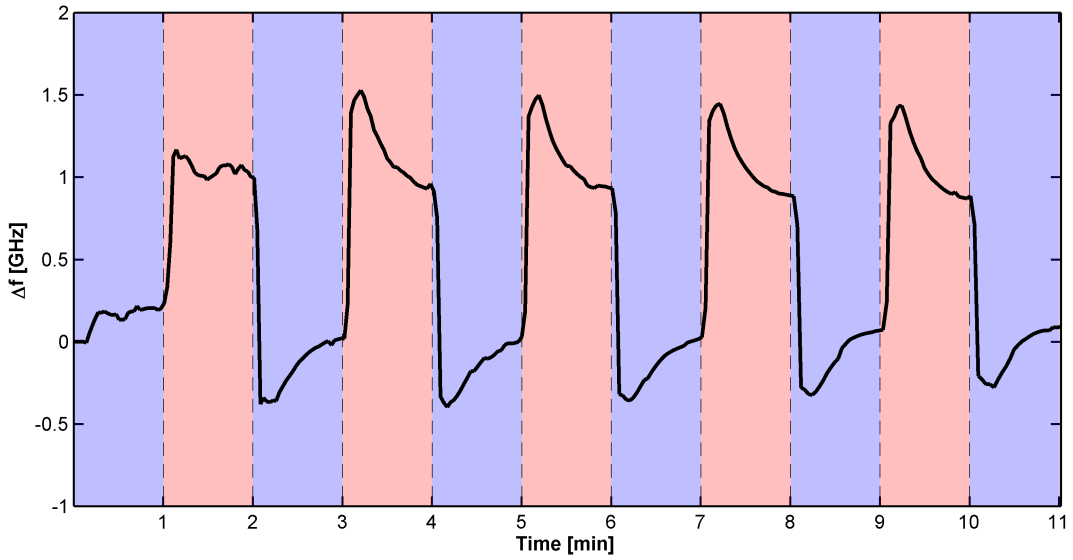

Figure 3.8: Differential resonator response as inlets with buffer switch from inlets 1 and 4 to inlets 2 and 3.

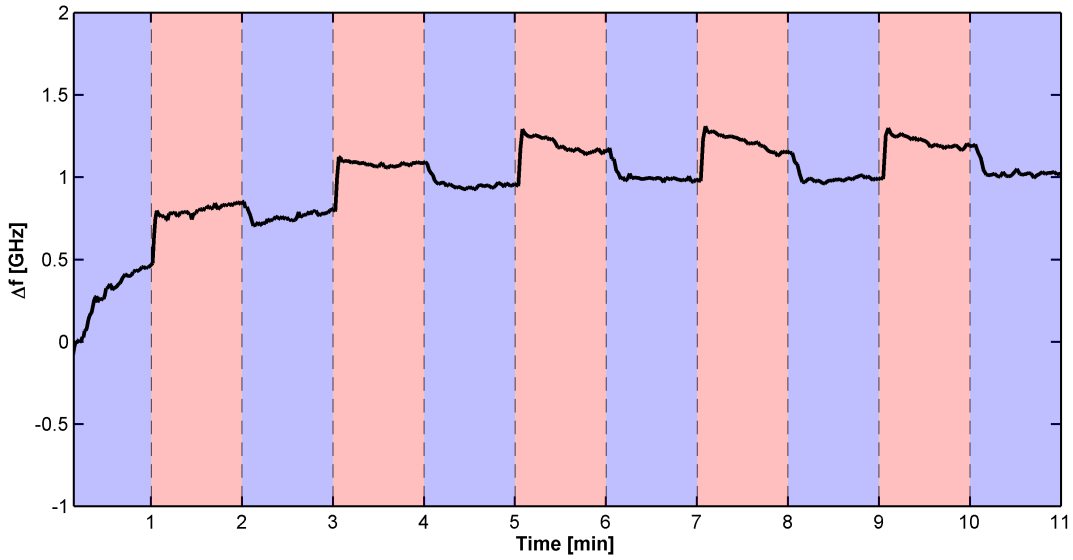

Figure 3.9: Differential resonator response as inlets with buffer switch from inlets 1 and 4 to inlets 2 and 4.

agent ratio, as well as on the temperature and time used for curing [10, 11]. We approximate $E \approx 1\,\text{MPa}$, for our conditions. For our system, $(\Delta PW)/(EH) = 2.2$ in our system, so the channel deformation and flow rate non-linearities must be considered.

3.3 Two-chip platform

In an attempt to reduce the switching transients described above, and to address constrains related to the surface functionalization chemistry that will be discussed in the next chapter, we introduce a two-chip platform, shown in Figure 3.10. One chip with elastomeric valves will perform the inlet switching (the control chip), while the second chip will have a single channel that encapsulates the two resonators (the resonator chip). One advantage of this platform is that by removing the valves from the chip, we reduce the footprint of the device; this makes it possible to increase the number of devices on a given chip area. Furthermore, we remove the height channel constraints related to the height of the valves (which should be below 20 µm to properly close), and reduce mechanical strain due to the valve closure. The disadvantage is that the response time will increase due to the increased volume in the flow channels. To illustrate the resulting response time increase due, Figure 3.11 shows the response to a step change in salt concentration between 0 and 160 mM and back. The signal shown represents the differential signal between the reference and sensing resonators. The data displays a delay time $t_{\text{delay}} \approx 100$ sec, and a transient time $t_{\text{transient}} \approx 30\,\text{s}$. We flow salt for a duration of 5 min, and then revert to the buffer for another 5 min, resulting in a total experiment duration of 10 min. We further notice that the signal saturates, which was not the case

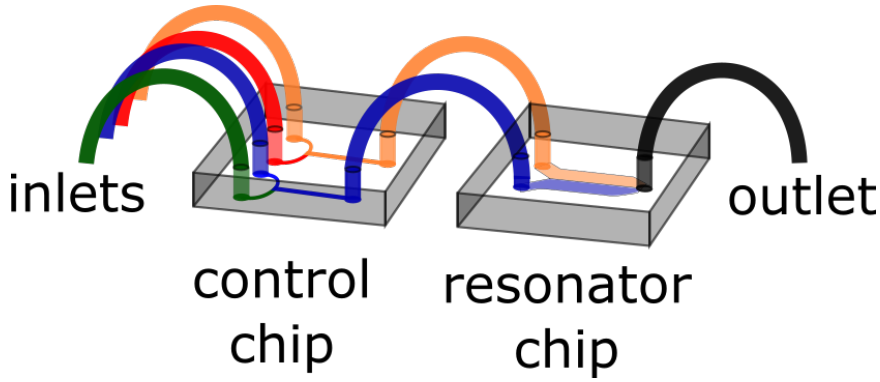

Figure 3.10: Two chip platform

for the solenoid data. Despite the fact that the two-chip platform is not as rapid as the on-chip valve platform, our sensing time is very good for experimental purposes.

The resistances of the flow elements of the two-chip platform are estimated by the methods described above to be $R_{\text{ctrl}} = 1.25 \times 10^{14} \text{Pa/m}^3\,\text{s}^{-1}$ for the control chip and $R_{\text{res}} = 1.5 \times 10^{12} \text{Pa/m}^3\,\text{s}^{-1}$ for the resonator channel. The control channel resistance is two orders of magnitude larger than any other resistance in the fluidic circuit, so the primary pressure drop will be across it. The resulting volumetric flow rate is

$$Q = \frac{\Delta P}{R} = 16.5 \mu\text{l}\,\text{min}^{-1}.$$

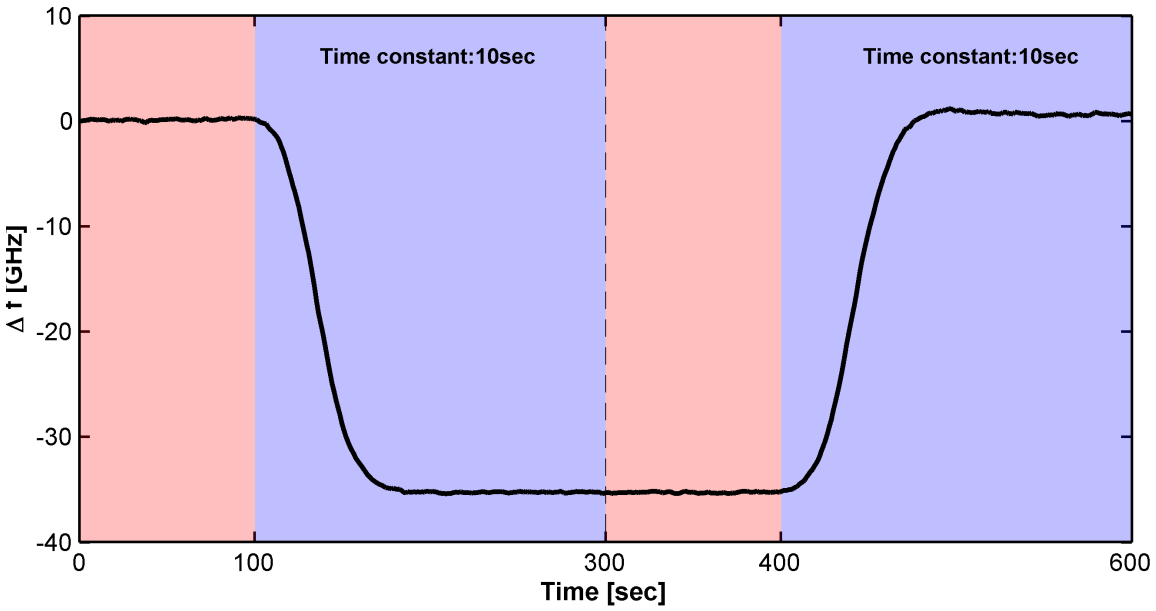

Figure 3.11: Response time in two-chip platform.

The average velocity in the resonator chip is, thus,

$$v_{\text{ave}} = \frac{Q}{hw} = 11\text{mm}\,\text{s}^{-1}.$$

The flow rate in the resonator channel in the two-chip platform is similar to the flow rate in the on-chip valve platform, while the average velocity in the channel is half of that for the on-chip valve platform.

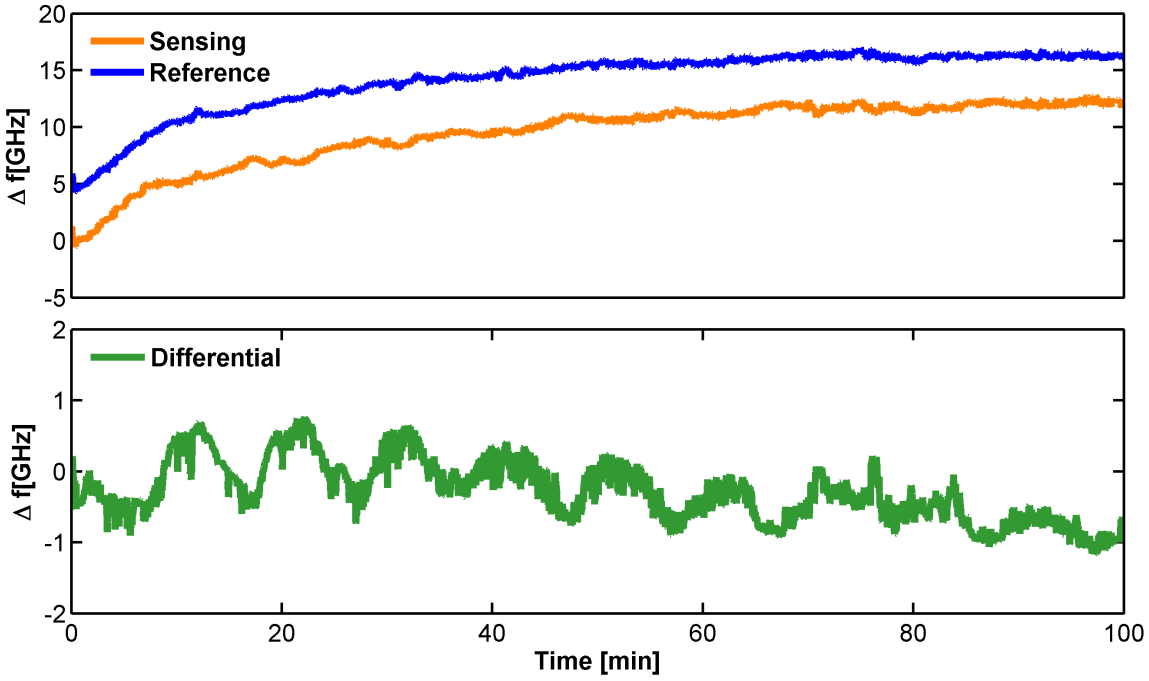

Figure 3.12: Switching transients in the two-chip platform.

Figure 3.12 shows the switching transients in the two-chip platform. The individual resonator responses exhibit large drifts, but the differential signal is fairly stable. Although not eliminated, the switching transients in the two-chip platform develop over longer time scales.

We note an interesting issue with the two-chip platform. Because the resistance of the resonator chip is much smaller than the total resistance of the fluidic network, the pressure drop across it is fairly low. Bubbles were observed at the inlets of the resonator chip; the bubbles were not introduced with the flow, but instead, they were generated inside the chip. By increasing the pressure both at the inlet and the outlet of the fluidic network by 28 kPa (2 psi), bubble formation was eliminated. This increase in absolute pressure (without an increase in relative pressure) is enough to eliminate bubbles in water.

3.4 Other considerations related to PDMS

Fabricating microfluidic devices using PDMS is a quick, low-cost and robust method that is ideal for rapid prototyping. However, when detecting small concentration of molecules, PDMS has a few disadvantages. The first is that it is elastic, which implies that, when a pressure is applied to drive the flow, the PDMS deforms and the transient stresses do not affect the two resonators in the same way. The second drawback is that PDMS absorbs small molecules, outgases uncrosslinked oligomers, and swells when exposed to organic solvents. To address this issue, we perform a solvent extraction step that consists of the following steps: boiling the PDMS chips in water for 1 hr, immersing them in diethyl ether for 24 hrs, immersing them in ethanol for 24 hrs, and finally immersing them in boiling water for another hour. This procedure removes the oligomers, and also swells the PDMS to the point it no longer swells in the presence of organic coumpounds. Other methods that might be applied to eliminate these effect include using sol-gel chemistry to coat the PDMS with a glass layer [12], or depositing a fluoropolymer CYTOP on the PDMS.

3.5 Mass transport models for the fluidic platforms

The transient resonator response after the analyte is introduced in the fluidic network is a consequence of the transport time needed for the solute to reach the resonators from either the three-way valve in the case of the syringe pump setup (Figure 3.1), or from the control chip in the case of the two-chip platform (Figure 3.5). Both methods introduce delays in the sensor response. These delays can be understood with simple mass transport models.

We first model the transport of solute in the two-chip platform, where the transient response is due to the transport in the Tygon tubing from the control chip to the resonator chip. The flow inside the tubing is a steady laminar flow through a cylindrical pipe. First, we consider the transport of a small slug of solute in the tube, a problem that was investigated by G.I. Taylor. The shear flow will affect the effective diffusion of the species, yielding an overall dispersion coefficient. Solving the convection-diffusion equation in a coordinate system that moves with the average fluid velocity v_{ave}, and assuming that radial concentration gradients are smoothed out, G.I. Taylor derived an average concentration at a distance z downstream and a time t after the injection of the slug:

$$c_{slug}(z,t) = \frac{M_A}{\sqrt{4D_{dis}t}} \exp\left(\frac{-(z - z_0 - v_{ave}t)^2}{4D_{dis}t}\right),$$

where z_0 is the location of the slug at $t = 0$, v_{ave} the average flow velocity in the channel, M_A the total mass of the slug, and D_{dis} the dispersion coefficient $D_{dis} = D \times (Pe^2/192)$. To obtain the concentration for a semi-infinite wall of concentration c_0 that is transported by the fluid, we

integrate z_0 from $-\infty$ to 0:

$$c_{ave}(z,t) = \int_{-\infty}^{0} c_{slug}(z,t)dz_0 = \frac{1}{2}c_0 \operatorname{erfc}\left(\frac{z - tv_{ave}}{2\sqrt{D_{dis}t}}\right)$$
$$= \frac{1}{2}c_0 \operatorname{erfc}\left(\frac{\tilde{z}}{d_{dis}}\right),$$

where we have defined $\tilde{z} = z - v_{ave}t$ to be the coordinate in the moving reference frame, and $d_{dis} = 2\sqrt{D_{dis}t}$ the dispersion length. The Taylor dispersion model is valid when the radial diffusion timescale is smaller than the axial convection time scale; thus, for a range of Peclet numbers that obey the relation:

$$\frac{64d_{dis}}{D_h} \gg Pe \gg 14.$$

From Table 3.2, the Peclet number in our system is $Pe \approx 450$, so the right side of the inequality is obeyed. The left side of the inequality becomes:

$$128\sqrt{D_{dis}t}/D_h \gg 450 \Rightarrow t \gg 2\text{s},$$

using that $D_h = 508\,\mu\text{m}$ for the Tygon tubing. The duration of the experiments is 5 min and 60 min, respectively, so the inequality holds and the Taylor dispersion model can be applied to our data. From the same table, we know that $v_{ave} = 1.4\,\text{mm}\,\text{s}^{-1}$ and we approximate the Tygon tubing length between the two chips to be $z \approx 200\,\text{mm}$. Since the diffusivity of salt is $D_{NaCl} = 1.6 \times 10^{-9}\text{m}^2\,\text{s}^{-1}$, we derive a dispersion coefficient D_{dis}:

$$D_{dis} = D\frac{Pe^2}{192} = 1.7 \times 10^{-6}\text{m}^2\,\text{s}^{-1}.$$

A least squares fit of the model to the data yields $D_{dis} = 1.8 \times 10^{-6}\text{m}^2\,\text{s}^{-1}$, which is in excellent agreement with our prediction. In Figure 3.13 we plot the theoretical model and the experimental response of the resonators to the introduction of two concentrations of salt using the two-chip platform.

We have neglected the transport inside the chip, because it is a very fast response, and we have also not modeled the transport inside the on-chip valve platform, for the same reason.

In the case of the syringe-pump setup, in addition to the Taylor dispersion inside the Tygon tubing, we must include in the model the mixing that occurs inside the three-way solenoid valve. The valve acts as a continuous stirred tank reactor, with a residence time inside the reactor $\tau = V/Q$, where Q is the flow rate and V is the volume of the solenoid chamber. The valve has an internal volume of $V = 111\,\mu\text{l}$, and for a $Q = 20\,\mu\text{l}\,\text{min}^{-1}$, we obtain $\tau \approx 5.5\,\text{min}$. The resulting concentration at the output of the solenoid is a decaying exponential of the form $c = c_0(1 - \exp(-t/\tau))$. To obtain

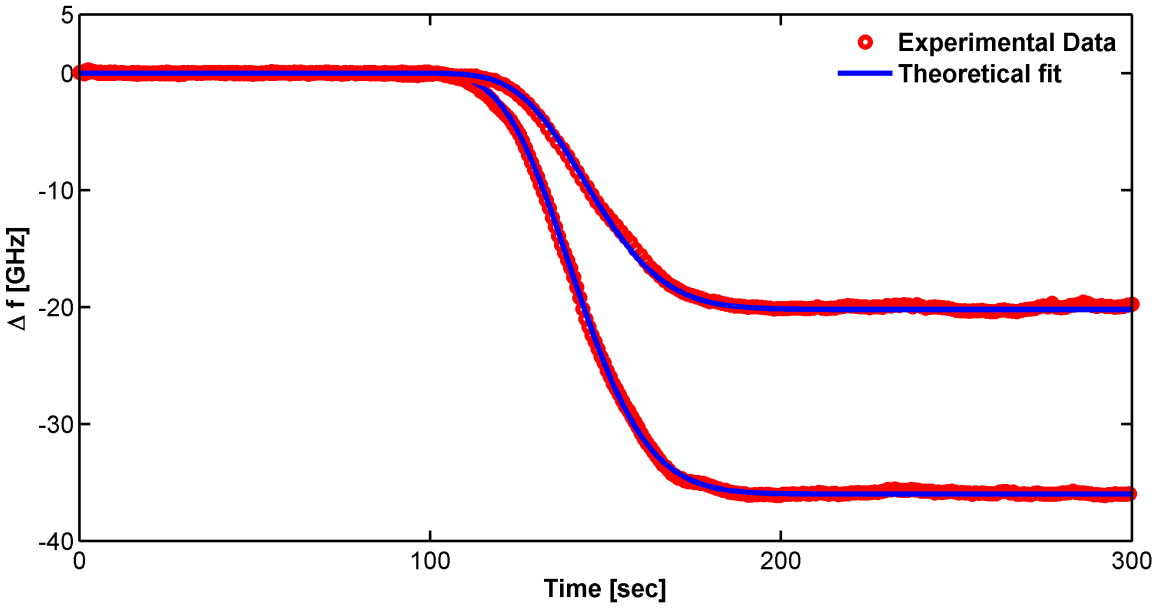

Figure 3.13: Experimental data (in red) for the two-chip platform response to concentrations of salt of 80mM and 160mM (the larger response is for the larger concentration). Theoretical curves based on the Taylor dispersion model (in blue) match the experimental data very well.

the concentration profile at a position z and time t from the outlet of the three-way solenoid valve:

$$\begin{aligned} c_{ave}(z,t) &= \int_{-\infty}^{0} (1-\exp(\frac{z0}{v_{ave}\tau}))c_{slug}(z,t)dz_0 \\ &= \frac{1}{2}c_0 \operatorname{erfc}\left(\frac{z-tu_{ave}}{2\sqrt{D_{dis}t}}\right) - \frac{1}{2}c_0 \exp\left(\frac{D_{dis}t+\tau v_{ave}(z-v_{ave}t)}{\tau^2 v_{ave}^2}\right)\operatorname{erfc}\left(\frac{z-tu_{ave}}{2\sqrt{D_{dis}t}}+\frac{\sqrt{D_{dis}t}}{\tau v_{ave}}\right) \\ &= \frac{1}{2}c_0 \operatorname{erfc}\left(\frac{\tilde{z}}{d_{dis}}\right) - \frac{1}{2}c_0 \exp\left(\frac{d_{dis}^2}{4\tau^2 v_{ave}^2}+\frac{\tilde{z}}{\tau v_{ave}}\right)\operatorname{erfc}\left(\frac{\tilde{z}}{d_{dis}}+\frac{d_{dis}}{2\tau v_{ave}}\right), \end{aligned}$$

where, as before, $d_{dis} = 2\sqrt{D_{dis}t}$ is the dispersion length, and $\tilde{z}$ is the coordinate in the moving reference frame. We used the same values for $v_{ave} = 1.4\,\mathrm{mm}$ and $D_{dis} = 1.8\,\mathrm{m}^2\,\mathrm{s}^{-1}$ and derive the values of $\tau = 450\mathrm{s}$ and $z = 0.9\mathrm{m}$ by least square fitting. The data and the fit are displayed in Figure 3.14. A slight slope that is due to the elasticity of the elements was included in the fit.

Both models explain the data and capture their distinct signatures. The resonator response in the two-chip platform has the characteristic symmetrical shape of the error function, whereas the three-way solenoid model has an initial quick rise, followed by a decaying exponential profile due to the mixing inside the three-way solenoid valve. Moreover, our estimated parameters agree with those derived from the least square fitting to the proposed models.

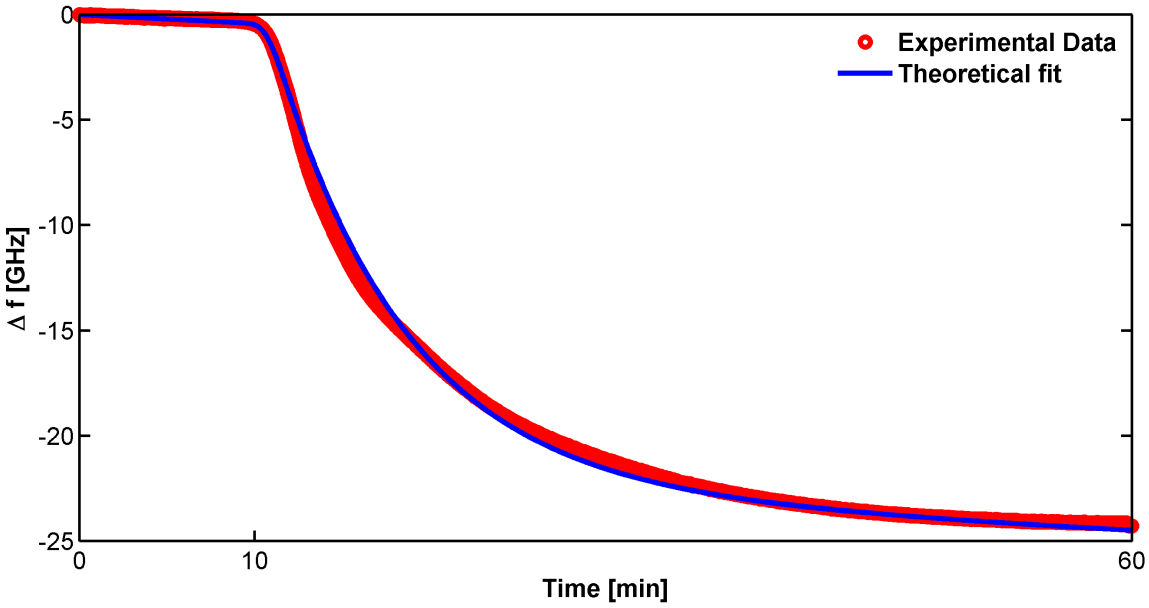

Figure 3.14: Experimental data (in red) for the solenoid setup response to a concentration of salt. The theoretical fit based on the Taylor dispersion model coupled to a continuous stirred tank reactor (in blue) matches very well the experimental data.

Bibliography

[1] M. A. Unger, H.-P. Chou, T. Thorsen, A. Scherer, and S. R. Quake, "Monolithic microfabricated valves and pumps by multilayer soft lithography," *Science*, vol. 288, no. 5463, pp. 113–116, 2000.

[2] D. C. Duffy, J. C. McDonald, O. J. A. Schueller, , and G. M. Whitesides*, "Rapid prototyping of microfluidic systems in poly(dimethylsiloxane)," *Analytical Chemistry*, vol. 70, no. 23, pp. 4974–4984, 1998.

[3] M. Iqbal, M. A. Gleeson, B. Spaugh, F. Tybor, W. G. Gunn, M. Hochberg, T. Baehr-Jones, R. C. Bailey, and L. C. Gunn, "Label-free biosensor arrays based on silicon ring resonators and high-speed optical scanning instrumentation," *IEEE Journal of Selected Topics in Quantum Electronics*, vol. 16, pp. 654–661, May 2010.

[4] C. F. Carlborg, K. B. Gylfason, A. Kazmierczak, F. Dortu, M. J. Banuls Polo, A. Maquieira Catala, G. M. Kresbach, H. Sohlstrom, T. Moh, L. Vivien, J. Popplewell, G. Ronan, C. A. Barrios, G. Stemme, and W. van der Wijngaart, "A packaged optical slot-waveguide ring resonator sensor array for multiplex label-free assays in labs-on-chips," *Lab Chip*, vol. 10, pp. 281–290, 2010.

[5] K. De Vos, J. Girones, T. Claes, Y. De Koninck, S. Popelka, E. Schacht, R. Baets, and P. Bi-

enstman, "Multiplexed antibody detection with an array of silicon-on-insulator microring resonators," *IEEE Photonics Journal*, vol. 1, no. 4, pp. 225–235, 2009.

[6] S. M. Grist, S. A. Schmidt, J. Flueckiger, V. Donzella, W. Shi, S. T. Fard, J. T. Kirk, D. M. Ratner, K. C. Cheung, and L. Chrostowski, "Silicon photonic micro-disk resonators for label-free biosensing," *Opt. Express*, vol. 21, pp. 7994–8006, Apr 2013.

[7] R. Robinson and R. Stokes, *Electrolyte Solutions: The Measurement and Interpretation of Conductance, Chemical Potential and Diffusion in Solutions of Simple Electrolytes, by R. A. Robinson and R. H. Stokes*. Butterworths [1965, reprinted 1970], 1965.

[8] W. Zeng, I. Jacobi, D. J. Beck, S. Li, and H. A. Stone, "Characterization of syringe-pump-driven induced pressure fluctuations in elastic microchannels," *Lab Chip*, vol. 15, pp. 1110–1115, 2015.

[9] T. Gervais, J. El-Ali, A. Gunther, and K. F. Jensen, "Flow-induced deformation of shallow microfluidic channels," *Lab Chip*, vol. 6, pp. 500–507, 2006.

[10] Z. Wang, A. A. Volinsky, and N. D. Gallant, "Crosslinking effect on polydimethylsiloxane elastic modulus measured by custom-built compression instrument," *Journal of Applied Polymer Science*, vol. 131, no. 22, pp. n/a–n/a, 2014.

[11] D. Fuard, T. Tzvetkova-Chevolleau, S. Decossas, P. Tracqui, and P. Schiavone, "Optimization of poly-di-methyl-siloxane (pdms) substrates for studying cellular adhesion and motility," *Microelectron. Eng.*, vol. 85, pp. 1289–1293, May 2008.

[12] A. R. Abate, D. Lee, T. Do, C. Holtze, and D. A. Weitz, "Glass coating for pdms microfluidic channels by sol–gel methods," *Lab on a Chip*, vol. 8, no. 4, pp. 516–518, 2008.

Chapter 4

Surface chemical functionalization for robust and selective detection

As described in Chapter 1, most applications of ring resonators rely on the detection and quantification of binding events between target biomolecular species and biorecognition elements attached to the sensor surface. Typical interactions include the high affinity binding of antigens to antibodies, complementary DNA strands to each other, or aptamers to target molecules. A crucial step in achieving robust and reliable biosensing is the chemical modification of the sensor surface so as to bind the biorecognition molecules through covalent bonds. The surface of the ring resonator is silicon nitride that forms a native silicon dioxide layer with available hydroxyl (-OH) bonds. Self-assembled monolayers (SAMs) are promising candidates for generating a linker layer to which a large number of capture molecules can attach. Commonly used SAMs are densely packed and well-ordered layers formed by crosslinked organosilanes. In the first half of this chapter we investigate chemical protocols aimed at depositing monolayers of aminosilane-based SAMs on silicon nitride. In the second half of the chapter we focus on achieving high selectivity for an array of sensors such that each sensor targets a different species. We present a newly synthesized molecule, a coumarin derivative, designed to selectively functionalize individual resonators. The work presented in this chapter was done in collaboration with C.J. Yu.

4.1 Aminosilane monolayer deposition

Organosilanes are silane derivatives that contain a carbon chain with a functional, reactive group at one end, and a Si atom bound to alkoxy groups, at the other end. The functional group can be chosen based on the specific application: for metal adhesion thiol groups (-SH) are employed, while for biomolecular attachment, amine ($-NH_2$) groups are used. The alkoxy head group adsorbs to the

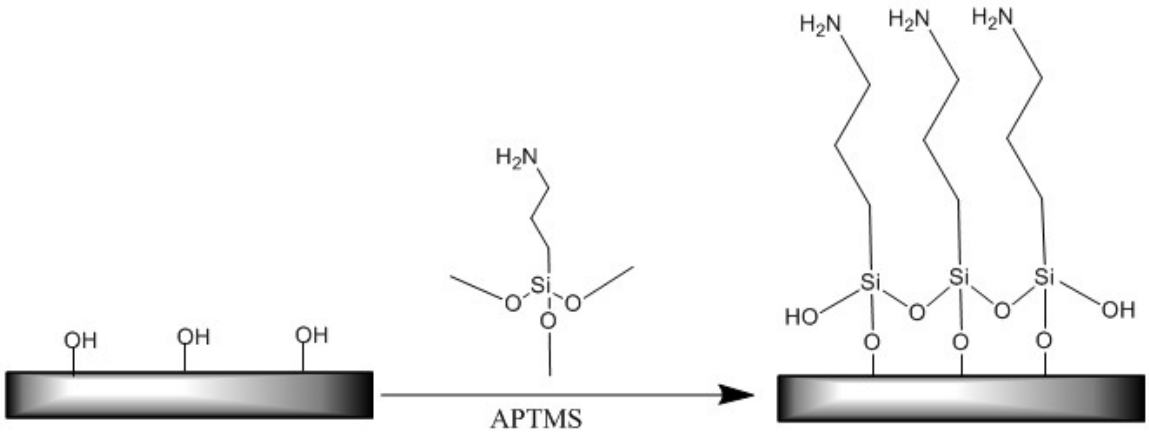

Figure 4.1: Silanization step in which an aminosilane first forms covalent siloxane bonds to the surface, then crosslinks to adjacent aminosilane molecules

surface, leaving the reactive tail group free to interact with the capture biomolecules. Aminosilanes bind covalenty to hydroxyl groups -OH present on the surface. To enhance the number of hydroxyl groups on the surface of the resonator, the silicon nitride surface is first cleaned in piranha, a highly corrosive solution made of 3:1 sulfuric acid (H_2SO_4) and hydrogen peroxide (H_2O_2). The piranha solution oxidizes the surface, which then further reacts with the atmospheric oxygen to create a native silicon oxide layer of a few nanometers thickness.

The formation of SAMs proceeds in two steps. First, the silanol groups Si-OH undergo a condensation reaction with surface -OH groups, forming siloxane groups Si-O-Si. Second, adjacent organosilanes crosslink and then undergo a long range organization of the tail groups, giving rise to a dense well-ordered monolayer (see Figure 4.1). A critical factor in the formation of aligned monolayers is the presence of water. Sung *et al.* [1] argue that the alkyl-siloxane monolayer formation on the surface of silicon nitride or on other oxidized silicon surfaces is due to a water layer formed on the surface. This hypothesis is corroborated by the formation of SAMs on gold or mica substrates that lack hydroxyl groups [2]. Hydrophobic surfaces, which are not expected to have a layer of water, do not generate good monolayers [3]. However, an excess of water can lead to aggregation of silane molecules and formation of polysiloxane particles [4].

A densely packed layer of reactive tail groups enables the deposition of a high concentration of capture molecules, thereby potentially enhancing sensor response. Dense layers of SAMs facilitate the reproducible deposition of capture molecules and control of the subsequent binding steps. The functional tail group can be selected to tailor the surface properties for a specific application. The physics of the sensing technology places constraints on the molecules that can be used, however. For ring resonators, the length of the aminosilane molecule and that of the subsequent binding

molecule must be short enough that bound analyte biomolecules are within the evanescent tail of the optical mode. Reliable deposition of a monolayer of aminosilanes ensures that further interactions of biomolecular species with the mode do not vary across experiments or sensors.

The conditions for monolayer deposition and the water concentration must be precisely controlled; moreover, high temperatures or vigorous agitation are required to prevent unwanted interactions of the terminal amine with the proton on the silanol oxygen, or formation of multilayers due to vertical stacking. After deposition, several rinsing steps are required to remove weakly physisorbed silanes. Most studies of SAMs of aminosilanes have focused on silicon dioxide surfaces [5], with only a few studies probing SAM formation on silicon nitride surfaces.

In the present study we employ aminopropyltrimethoxysilane (APTMS), an aminosilane with a three-atom carbon chain and three methoxy ($-CH_3$) groups linked to the Si atom. APTMS is a promising candidate due to its short carbon chain that should place the binding molecule in the the evanescent field. Two methods for depositing aminosilanes on a surface are commonly used: (i) solution-phase, or (ii) vapor-phase deposition. Hamlett *et al.* argue that 60 min immersion of silicon nitride substrates in a solution of 0.5 mM APTMS in anhydrous ethanol leads to the formation of a single uniform monolayer [6]. Zhang *et al.* have shown that low, micromolar range, concentrations of silanes are desirable since they are not conductive to polysiloxane aggregate formation [7]. Therefore, we choose to perform the deposition of APTMS in solution-phase, at low concentrations of APTMS, and use anhydrous solvents with trace amounts of water.

To determine the conditions for which SAMs form on silicon nitride, we test a number of conditions and solvents. All samples are prepared in a modified Schlenk line under nitrogen. The two solvents tested are anhydrous ethanol and anhydrous toluene; agitaion methods explored include sonication and shaking. We tested 1 mM and 2 mM APTMS solutions in either ethanol or toluene, with either sonication or shaking for a duration of 30 min. Ice was added to the water bath during sonication to keep the temperature from rising.

To determine if a monolayer of APTMS has formed, we employ a number of surface characterization methods. Atomic-force microscopy (AFM) is used to determine the surface roughness of the silane layer. The roughness should decrease after the formation of SAMs compared to the roughness of the bare silicon nitride. Ellipsometry, which has Ångström resolution, measures the thickness of the thin film. X-Ray Photoelectron Spectroscopy (XPS) probes the chemical composition of the top few nanometers at the surface, and measures the characteristic binding energies of the electrons in this region. Lastly, fluorescent microscopy is used to qualitatively test the presence and uniformity of the monolayer.

4.1.1 Surface characterization using AFM, ellipsometry, XPS, and fluorescence measurements

AFM maps the topography of the sensor. This microscopy technique probes the surface of the sample by measuring the forces between a sharp tip attached to a cantilever and the surface. A laser beam reflected by the cantilever measures its position, and piezoresistive elements close the feedback loop. The cantilever can be operated either in contact or tapping mode. In contact mode, the force between the cantilever and surface is kept constant, as the surface is scanned by the tip. In tapping mode, the cantilever oscillates at its resonant frequency; any interaction between the tip and the surface leads to the damping of the oscillations. AFM scans were performed with a MFP-3D^{TM} Asylum Research AFM located in the Atwater group at California Institute of Technology. The data was analyzed using Gwyddion Software [8]

The topography of the silicon nitride surface after a 10 min piranha cleaning step is shown in Figure 4.2. The roughness of the surface is described in terms of two parameters: the root-mean-square surface roughness R_q, and the average roughness R_a. Following the piranha cleaning, R_a=0.186 nm and R_q=0.235 nm. First we test the need for anhydrous solvents and silanization under a nitrogen atmosphere, by depositing 40 mM (1%) APTES in ethanol for 30 min outside of the Schlenk line. The samples are shown in Figure 4.3. Polysiloxane particles as large as 10 nm diameter are detected. This test further emphasizes the need for robust protocols in generating silane monolayers.

Figure 4.4 shows topographies of representative samples exposed to solutions of 1 mM APTMS in anhydrous ethanol and anhydrous toluene. The surface exposed to ethanol appears uniform, with R_a = 0.178 nm and R_q = 0.230 nm. We expect the silane monolayer to decrease the roughness of the surface, via the so-called "carpet effect" [6]. Although the roughness is not significatly lower

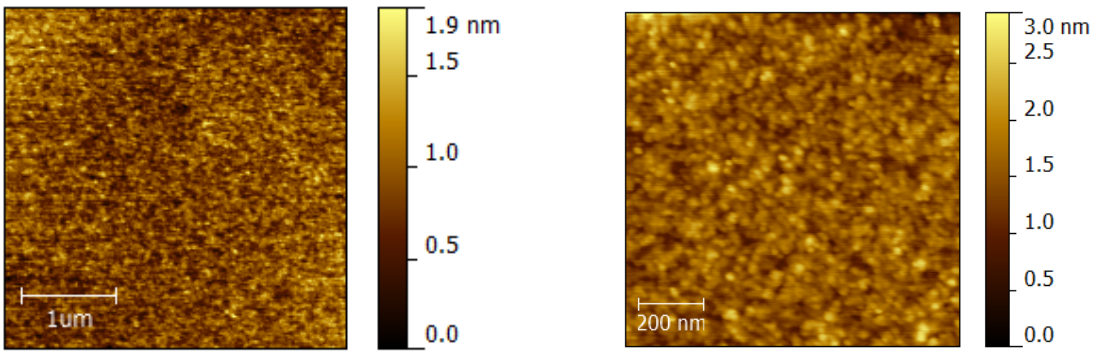

Figure 4.2: a) AFM measurement of piranha cleaned chip. b) Detailed scan of the piranha cleaned chip.

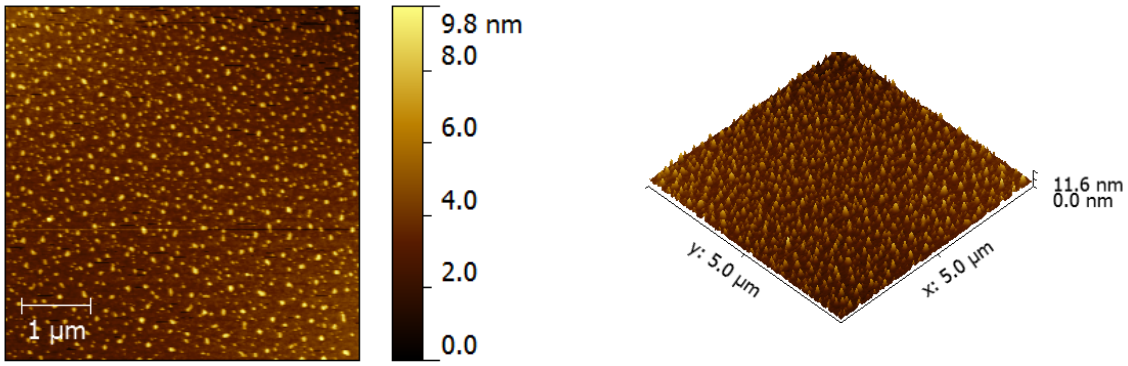

Figure 4.3: a) AFM measurement of deposition of 40 mM APTES, which forms polysiloxane particles. b) 3D model of the same sample.

than on the piranha cleaned sample, the measured values is consistent with monolayer deposition. The surface exposed to toluene shows many polysiloxane particles, in this case, $R_{\mathrm{a}} = 0.58\,\mathrm{nm}$ and $R_{\mathrm{q}} = 1.08\,\mathrm{nm}$.

AFM images of other samples processed at 0.5 mM, 1 mM, and 2 mM reveal some experiment-to-experiment variations, but the most consistent monolayer development was obtained using anhydrous ethanol and sonication.

To measure the chemical composition of the surface of a sample we employed X-ray Photoelectron Spectroscopy (XPS). This method involves irradiating the surface with high energy X-rays. The X-rays excite core-level electrons that are ejected from the atom; the energies of the emitted electrons reveal the composition of the surface atoms. Using conservation of energy, we can write:

$$h\nu = E_{\mathrm{binding}} + E_{\mathrm{kinetic}} + \Phi,$$

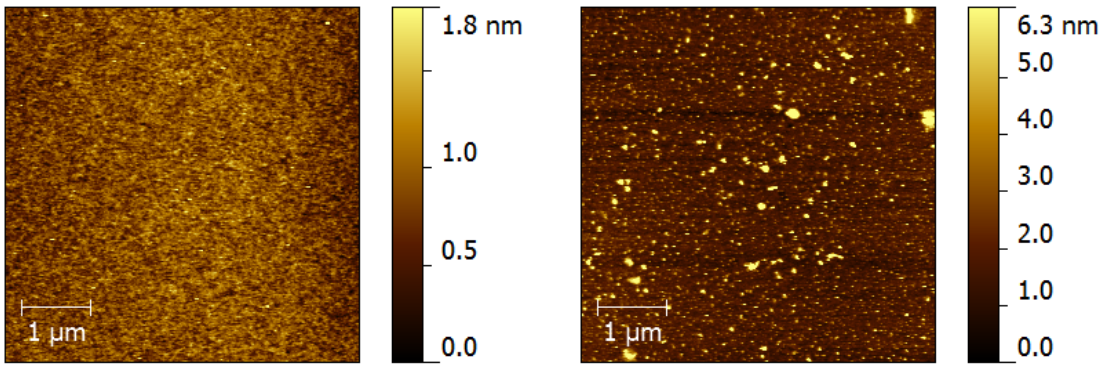

Figure 4.4: a) AFM measurement of APTMS deposited at a 1 mM concentration in anhydrous ethanol, with 30 min sonication. b)AFM measurement of APTMS deposited at a 1 mM concentration in anhydrous toluene, with 30 min sonication.

where $h\nu$ is the energy of the incident X-ray, and Φ is the work function of the material. E_{binding} represents the characteristic orbital energy of the electrons to the atoms. XPS requires ultra high vacuum systems to prevent the interaction of the X-rays and electrons with gas molecules; it is sensitive to the chemical composition of only the first 1-10 nm of the surface, since those electrons are able to escape more easily than the electrons from the bulk of the sample.

We analyze the surface chemistry of the samples after three steps: piranha cleaning, silane deposition, and biotin attachment to the silane layer. XPS spectra were recorded using Surface Science M-Probe ESCA/XPS. Research was in part carried out at the Molecular Materials Research Center of the Beckman Institute of the California Institute of Technology. The analysis was done using the CasaXPS software. The XPS spectra, shown in Figure 4.5, display silicon (Si), nitrogen (N), oxygen (O), and carbon (C) peaks for all three conditions. Due to the silicon nitride substrate, all spectra contain Si(2s), Si(2p), N(1s) peaks, located at 151 eV, 100 eV, and 399 eV respectively. The O(1s) peak, located at 530 eV is due to the native oxide layer formed by the oxidation of the silicon nitride surface, and the C(1s) peak, located at 285 eV, is associated with both volatile organic compounds that have been adsorbed on the surface and the aminosilane layer.

Integrating the regions under the transition peaks provides a quantitative estimate of the percentage atomic concentrations of the elements (see Figure 4.1). The carbon concentration in the silane sample is greater than that in the piranha sample, as expected following the deposition of an organic molecule, such as APTMS. The oxygen concentration is also higher in the silane sample compared to the piranha sample, indicating the formation of siloxane bonds between the APTMS molecules. Although APTMS contains nitrogen, the overall nitrogen percentage has decreased, however, because the silicon nitride surface is now buried under the organic layer, reducing its contribution to the signal. The silicon signal has decreased for the same reason. In the biotin sample, we expect a sulfur peak located at 230 eV, but it was not detected, because its concentration is much lower than the concentrations of the other elements.

XPS data is suggestive of deposition of silane, but it does not give information on the quality of the monolayer. We conclude that XPS is more useful for confirming the presence of silane on the sample rather than for discriminating between different protocols.

Sample	Carbon Percentage	Oxygen Percentage	Nitrogen Percentage	Silicon Percentage
Piranha	9.22	20.04	33.50	37.25
Silane	20.24	26.27	25.86	27.63
Biotin	21.90	22.04	25.84	30.21

Table 4.1: Percentage atomic concentration for the detected elements in three sample with different chemistries.

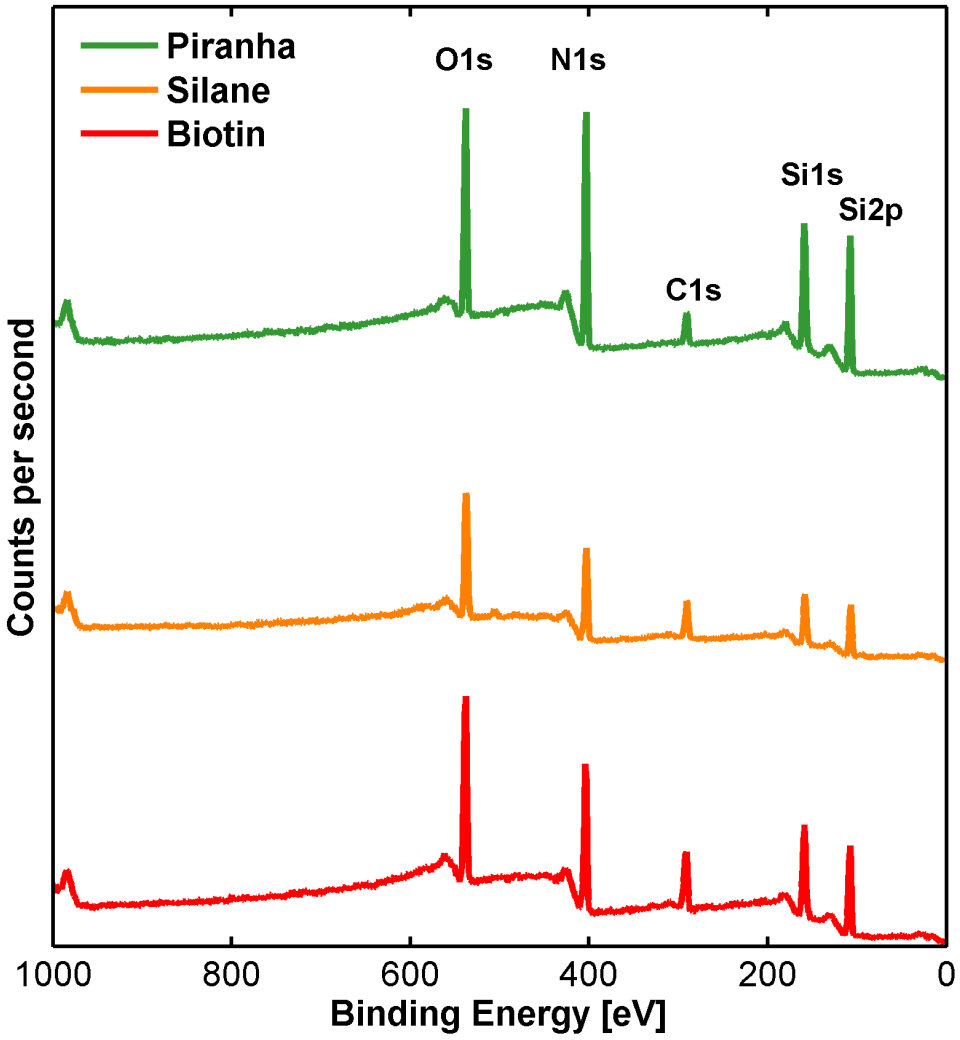

Figure 4.5: XPS Survery Spectrum of three samples: after piranha cleaning, after silane deposition, and after biotin attachment

Ellipsometry is a very sensitive method for determining the thickness of a thin film. It analyzes changes in the polarization of light after it is reflected from the surface. Reflection of monochromatic polarized light from the sample surface produces an elliptically polarized wave. The ratio of the p-polarized and s-polarized components is:

$$\rho = \frac{r_p}{r_s} = tan(\Psi)e^{i\Delta}.$$

This signal contains both the intensity and phase shift information, since $\tan\Psi$ represents the ratio of the amplitudes, and Δ the phase delay between the two waves.

Ellipsometry data was recorded using an ellipsometer located in the Lewis group, and was analyzed using the CompleteEASE software. Data taken after piranha cleaning establish the thickness

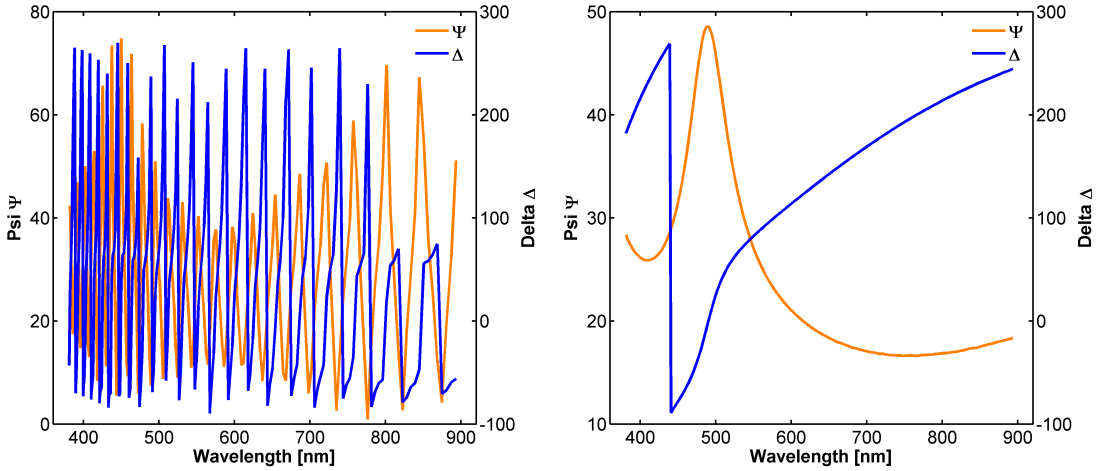

Figure 4.6: a) Ellipsometry data recorded with samples containing a 6 µm layer of silicon dioxide, which causes interferemece in the spectrum. b) Ellipsometry data recorded with samples without the silicon dioxide layer.

of the silicon nitride and that of the native oxide thickness. The organic layer was modeled as a Cauchy layer. The wafers used for resonator fabrication contain a SiO_2 layer in between the silicon nitride and the silicon substrate. Due to this layer, the ellipsometry spectrum is crowded with interference patterns that make fitting the data to the model difficult. Therefore, we prepared different samples without the SiO_2 layer to probe the organic layer thickness. As seen in Figure 4.6, their spectrum is much cleaner than the previous samples.

Solvent	Method of agitation	Thickness
Ethanol	Shaking	25 ± 9 Å
Ethanol	Sonication	10 ± 3 Å
Toluene	Shaking	30 ± 2 Å
Toluene	Sonication	50 ± 6 Å

Table 4.2: Thickness of silane layers for four different deposition conditions for a solution of 1 mM APTMS.

The ellipsometry data was the most quantitative compared to the other characterization techniques employed in this study in discriminating between monolayer deposition conditions. Samples were measured for conditions of 1 mM APTMS in either anhydrous ethanol or toluene with sonication or shaking. The ellipsometry data was taken at three angles for each sample: 65°,70°, and 75°, and in two different locations. The data are summarized in Figure 4.2. Since the expected thickness of the APTMS monolayer is ≈ 7 Å, we conclude that anhydrous ethanol is a better solvent than toluene, and that sonication leads to more uniform monolayers than shaking, for ethanol. The condition that seems most promising is 1 mM APTMS in anhydrous ethanol with sonication. Since

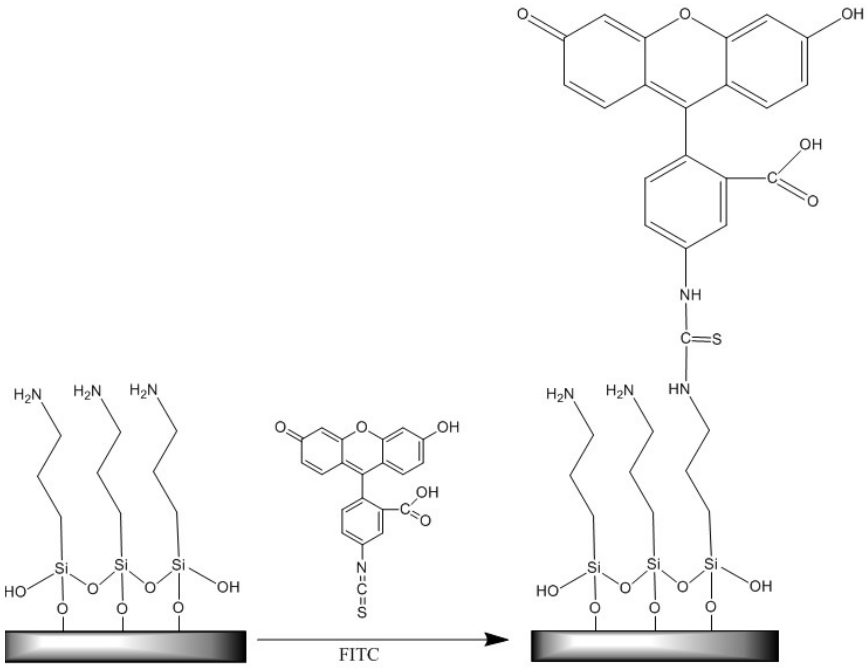

Figure 4.7: Chemistry of FITC addition

the AFM data for the same condition corroborates the formation of a monolayer, we will adopt it for subsequent chemistry steps.

To check the uniformity of the monolayer, we use fluorescence microscopy to monitor the attachment of a fluorescent dye, fluorescein isothiocyanate (FITC), that has a reactive -N=C=S group that binds to amine groups. Fluorescence data were taken using Zeiss LSM microscopes at the Biological Imaging Center at California Insitute of Technology. The chemistry behind the attachment of the FITC dye is depicted in Figure 4.7. The procedure for attaching FITC to the silane monolayer involves adding FITC to a DMSO solution containing triethyl amine. The vial was wrapped with aluminum foil and shaken overnight. The chips were transferred into another vial containing DMSO, and shaken for an additional 15 min. The chips were then washed three times with DMSO, and three times with ethanol. The chips were then dried under flowing nitrogen.

The excitation spectrum of FITC has a peak around 495 nm; the emission spectrum has a peak around 519 nm. To image the FITC dye, we excite the sample with the 488 nm line of a 30 mW Argon laser at 2% power; the fluorescence image of the sample was observed through a bandpass filter 505 nm-530 nm. Figure 4.8 shows the fluorescence spectrum of three samples. For the first sample, after a piranha cleaning step, we attach FITC overnight. Only background intensity is present, indicating that FITC does not attach to silicon nitride without a linker layer. The second image shows a sample to which APTMS has been added. This condition demonstrates that there is no autofluorescence of the APTMS. The third sample, in which an APTMS coated sample has been

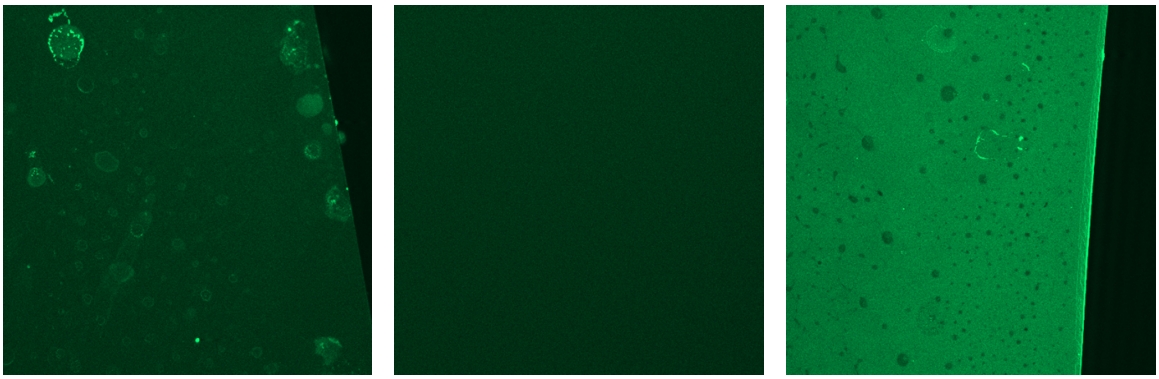

Figure 4.8: Fluorescence image showing the attachment of FITC to APTMS. In the left figure we show a blank wafer to which FITC has been added. The intensity is very low, indicating that FITC has not attached to the substrate in the absence of a linker layer. In the center image, APTMS has been added to the nitride, but again there is no fluorescence. In the left image, FITC has been added to the APTMS-coated nitride, resulting in a high intensity fluorescence signal. This indicates that FITC only binds to the substrate in the presence of APTMS.

exposed to FITC shows a large fluorescent signal. This proves that FITC only binds to the surface of our samples in the presence of APTMS.

The fluorescence tests confirmed the uniformity of silane deposition by sonicating of a solution of 1 mM APTMS in anhydrous ethanol under nitrogen. However, this protocol is not compatible with the on-chip valve PDMS device fabrication. The bonding between the PDMS and silicon nitride is performed after both substrates are exposed to an oxygen plasma atmosphere, which would degrade the silane monolayer. Oxygen plasma is required to enhance the hydroxyl bonds on the both surfaces, which would increase the binding strength. Therefore, we resorted to introducing a two-chip platform, which was presented in Chapter 3. In this platform we can perform the bonding of the control chip under plasma, since the pressures applied to the control lines in this chip require high bonding strengths. The resonator chip can be bonded at room temperature, and withstands up to 52 kPa (6 psi) of fluid pressure, which is compatible with our flow rates. In addition, the two-chip platform has added benefits in device density integration.

4.2 Photocaging chemistry for local functionalization of resonator

To increase the selectivity of the resonators and be able to have a multiplexed platform with different resonators targeting specific molecules in solution, we explore the use of photoremovable protecting groups. The first step is to pattern the entire bottom surface of the channel with a passivating layer, to which molecules cannot bind. Then, we remove the protective layer only the resonator surface, revealing the reactive amine groups. This would enable us to attach a specific antibody to

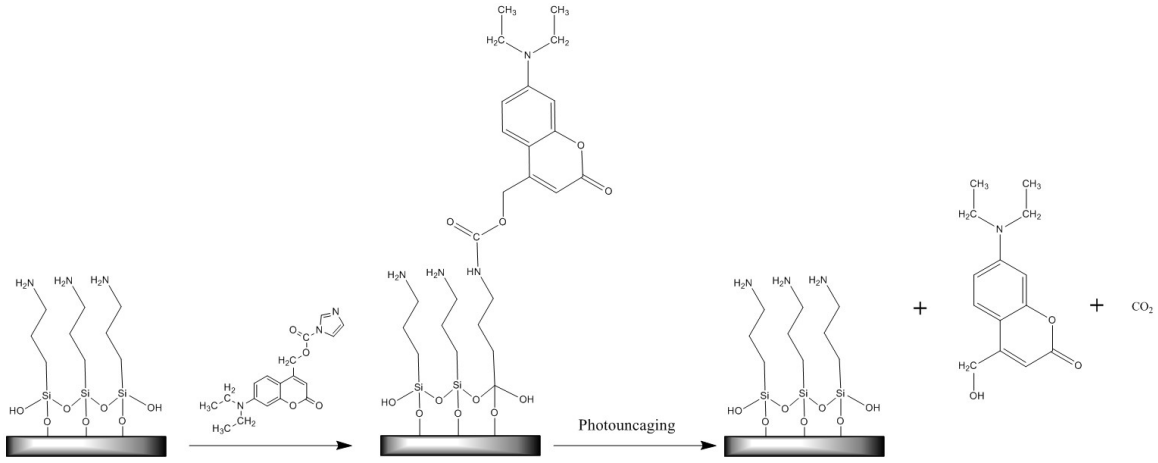

Figure 4.9: Chemistry of coumarin addition and photouncaging.

one resonator, then repeat the same process for the next resonator. In the end, each resonator is functionalized to bind a different target antigen. In addition, the rest of the channel is passivated, and there is no loss of antigens to the walls. Furthermore, the mass transport to each resonator is enhanced due to small depletion boundary layers. Similar protocols have been developed for polymer WGM sensors by Beck *et al.* , using protecting groups based on benzophenon [9]. This method would be an alternative to microcontact printing or inkjet spotting.

Inspired by the work of Vishakha *et al.* that uses an aminocoumarin derivative to cage carboxylic acids, we decided to synthesize a new coumarin derivative that binds to reactive amine groups at one end, and is passive at the other end [10]. The synthesis of this molecule was performed by C.J. Yu. The chemistry of coumarin addition to silane monolayers is displayed in Figure 4.9. Upon exposure to 405 nm laser light, the coumarin unbinds from the silane, leaving the reactive amine groups exposed.

To deposit coumarin on APTMS silanized chips, we add 10 µM of activated coumarin in a DMF solution, and wrap the glass vial in aluminum foil. The glass vial is shaken for 3 days. The chips are then transferred into another vial containing DMF, and placed on a shaker for 10 min. The chips are then washed three times with DMF and three times with ethanol, and dried under nitrogen.

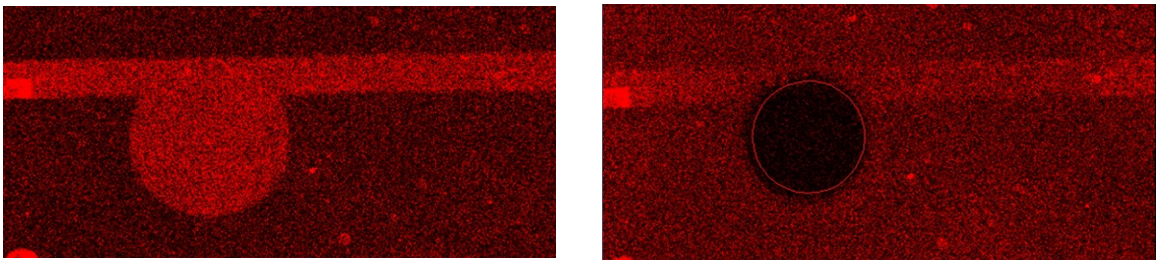

Figure 4.10: The left image shows the sample with coumarin attached. The right image shows that coumarin has been selectively removed from the resonator surface

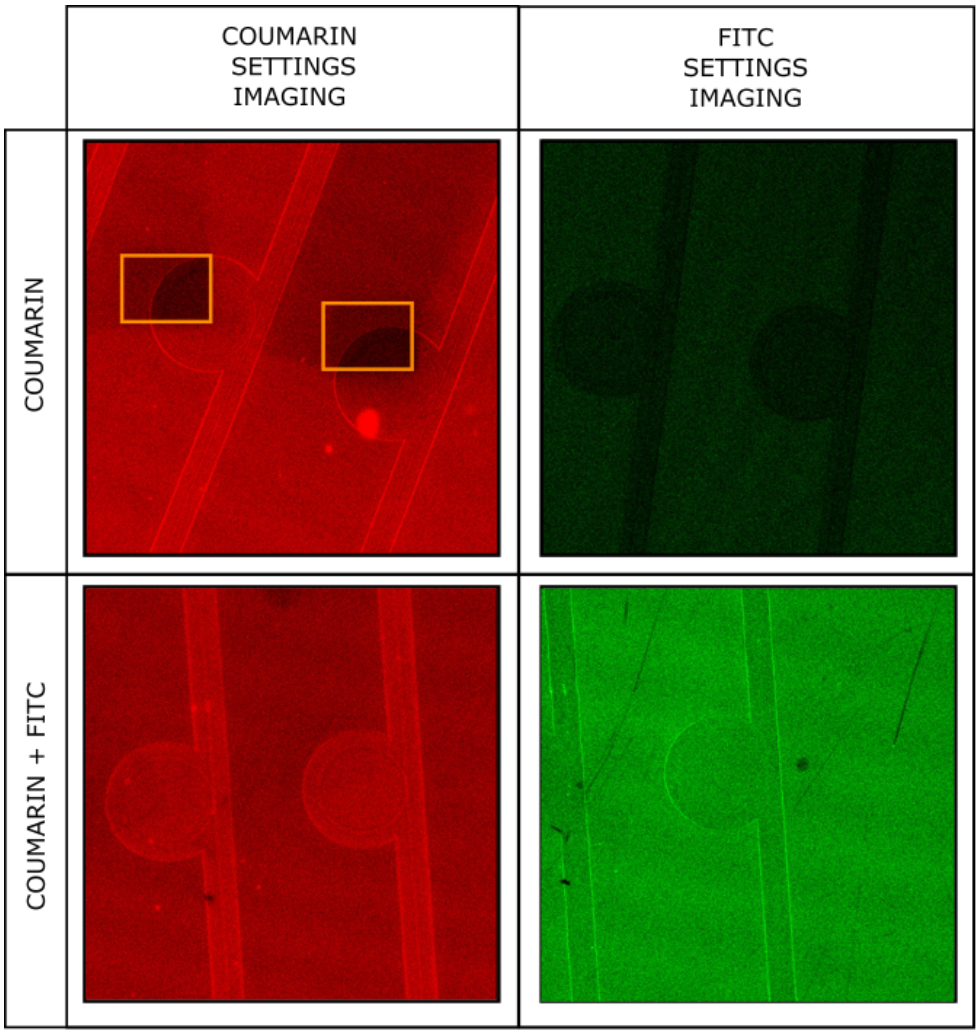

Figure 4.11: The top row shows the sample after coumarin was deposited. The left panel shows the fluorescence under settings for coumarin detection (left) and under settings for FITC detection (right). The bottom row shows the same area on the same sample after FITC has been deposited.

Figure 4.10 shows the selective removal of coumarin from the resonator surface (also known as photouncaging). We note that the fluorescence intensity on the etched area around the resonator is higher than in other areas. One possible explanation is that the etch is deep enough to reach to the underlying oxide layer, and the silane layer has a higher density of available amines than the silicon nitride.

To test whether the selective removal of the coumarin leaves the reactive amine groups available for further binding, we again add FITC to the sample. Ideally, the FITC would only attach locally on the resonator surface. However, as shown in Figure 4.11, the FITC attaches everywhere. The top row of the same figure shows a sample with only coumarin attached. We detect the presence of the coumarin, and the lack of an FITC signal. Two rectangular regions are photouncaged on the sample. The bottom row shows the same sample, after the next step, the addition of FITC. We

notice that the FITC signal is uniform across the surface of the wafer. This means that either the coumarin did not block the attachment of FITC, or that FITC was able to outcompete the coumarin for the amine bonds.

We test a different fluorescent dye that reacts with amines, Texas Red, with similar results. Another attempt to troubleshoot the coumarin chemistry assumes that the coumarin molecules do not bind all available amine groups, and there are still reactive amine groups left to interact with the FITC. To test this hypothesis, we use blocking agents, and add 0.5 mL of acetic anhydride and 0.5 mL of triethyl amine to the coumarin solution. These molecules are smaller in size than coumarin, so they should passivate all the amine groups, and not allow the attachment of FITC. However, the experiments show that the results do not change, and FITC is able to bind uniformly over the surface of the chip. In the end, we decided that the coumarin chemistry, despite its potential benefits, does not look promising for silicon nitride resonators.

Bibliography

[1] M. M. Sung, G. J. Kluth, and R. Maboudian, "Formation of alkylsiloxane self-assembled monolayers on Si_3N_4," *Journal of Vacuum Science and Technology A*, vol. 17, no. 2, pp. 540–544, 1999.

[2] S. Gilles, "Chemical modification of silicon surfaces for the application in soft lithography," diplom (univ.), Univ. Freiberg, Jülich, 2007.

[3] C. A. E. Hamlett, *Utilization of nanostructured surfaces for sensing applications and the use of nanoentities for the fabrication of new materials.* PhD thesis, University of Birmingham, December 2008.

[4] B. C. Bunker, R. W. Carpick, R. A. Assink, M. L. Thomas, M. G. Hankins, J. A. Voigt, D. Sipola, M. P. de Boer, , and G. L. Gulley, "The impact of solution agglomeration on the deposition of self-assembled monolayers," *Langmuir*, vol. 16, no. 20, pp. 7742–7751, 2000.

[5] H. K. Hunt, C. Soteropulos, and A. M. Armani, "Bioconjugation strategies for microtoroidal optical resonators," *Sensors*, vol. 10, no. 10, p. 9317, 2010.

[6] C. A. Hamlett, K. Critchley, M. Gorzny, S. D. Evans, P. D. Prewett, and J. A. Preece, "Vapour phase formation of amino functionalised Si_3N_4 surfaces," *Surface Science*, vol. 602, no. 16, pp. 2724 – 2733, 2008.

[7] F. Zhang, , and M. P. Srinivasan*, "Self-assembled molecular films of aminosilanes and their immobilization capacities," *Langmuir*, vol. 20, no. 6, pp. 2309–2314, 2004.

[8] D. Neas and P. Klapetek, "Gwyddion: an open-source software for SPM data analysis," *Central European Journal of Physics*, vol. 10, pp. 181–188, 2012.

[9] T. Beck, M. Mai, T. Grossmann, T. Wienhold, M. Hauser, T. Mappes, and H. Kalt, "High-Q polymer resonators with spatially controlled photo-functionalization for biosensing applications," *Applied Physics Letters*, vol. 102, no. 12, 2013.

[10] V. R. Shembekar, Y. Chen, B. K. Carpenter, , and G. P. Hess, "A protecting group for carboxylic acids that can be photolyzed by visible light," *Biochemistry*, vol. 44, no. 19, pp. 7107–7114, 2005.

Chapter 5

Enhancement of mass transport

Biosensing platforms employ sample delivery systems to transport fresh analyte to the reactive surface of the sensor. In most platforms the sensor is located on the bottom surface of a microfluidic channel. Due to the small size of the channel and the driving pressures typically used, the flow is laminar, and viscous effects dominate over inertial effects. As target molecules adsorb to the surface of the sensor, a depletion boundary layer forms near the sensor which increases the resistance to mass transport to the sensor. Because the sensor is located near the bottom of the channel, where the slip-velocity is zero, convection mechanisms cannot replenish the depleted analyte; hence, the only mechanism for target molecules to reach the sensor is through diffusion. In Figure 5.1 we depict the three main mechanisms undergone by target molecules inside the channel: convection, diffusion and reaction [1]. Target molecules are swept downstream, where they diffuse to and can adsorb onto reactive surfaces; after binding, they may also desorb. The general behavior of the fluid and molecular species can be characterized by a few non-dimensional numbers that relate the importance of the different mechanisms. These are:

- Reynolds number (Re): quantifies the importance of the inertial forces relative to viscous forces. The Reynolds number is defined as $Re = \frac{\rho U L}{\mu}$, where U is the average flow velocity in the channel, L is the characteristic length of the flow, and μ is the dynamic viscosity of the fluid. A Reynolds number below 2000 indicates that the fluid flow in a cylindrical tube of diameter L is laminar, that there is no mixing between fluid layers, and no turbulence. To describe the flow in the rectangular channel of our microfluidic device, the hydraulic diameter D_h is used, which was described in Chapter 3.

- Péclet number (Pe): quantifies the importance of convection relative to diffusion. It is defined as $Pe = \frac{UL}{D}$, where D is the diffusivity of the species. A high Peclet number indicates that convection dominates over diffusion, and target molecules are swept downstream before they have time to diffuse to the walls.

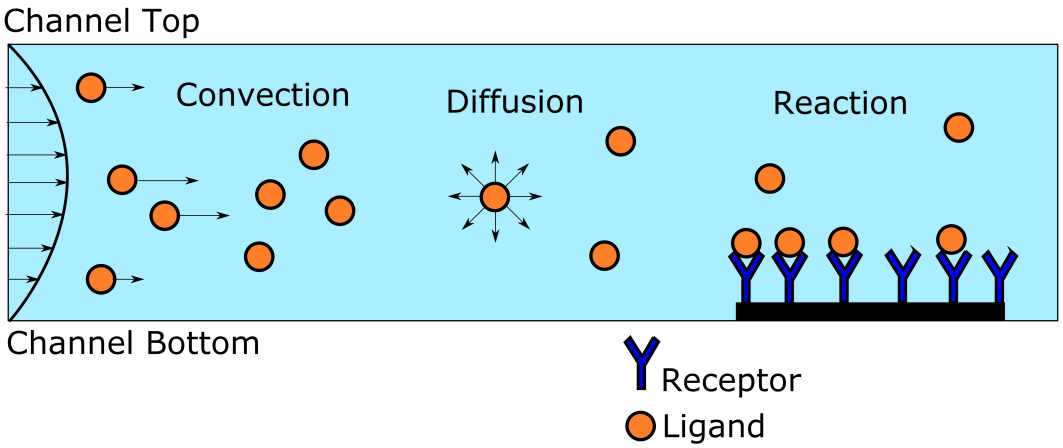

Figure 5.1: Schematic of the three mechanisms involved in delivering the analyte to the sensor surface: convection, diffusion, and reaction.

- Damkhöler number (Da): quantifies the relative importance of reaction versus diffusion. It is defined as $Da = \frac{k_{\text{on}}\Gamma H}{D}$, where k_{on} is the adsorption binding rate, Γ is the density of available binding sites on the reactive surface. A high Damkhöler number indicates that the adsorption of molecules to the sensor proceeds faster than the diffusion mechanism can supply new target molecules for binding.

- Sherwood number (Sh): quantifies the contribution of mass transfer relative to diffusion, and it is defined as the ratio of the concentration gradient at the wall to the concentration difference between the bulk and the wall. $Sh = k_{\text{m}} D_{\text{h}}/D$ where k_{m} is the mass transfer coefficient.

In our case, as shown in Chapter 3, we operate at low Reynolds numbers, high Peclet numbers, and high Damköhler numbers.

5.1 Overview

A few ways to overcome the slow mass transport and replenish the analyte near the reactive surface have been explored in the past. Many solutions use active methods (such as peristaltic pumping and magnetic beads), but these methods add complexity and cost to the biosensing platform. In 2002, Strook *et al.* introduced grooved surfaces for engineering flows in long and narrow microfluidic channels [2] [3]. A perturbation analysis was performed to compare the flow to that of a lid driven cavity model [4]. A herringbone arrangement of the grooves was shown to enhance mixing inside microfluidic channels by stretching and folding the fluid streamlines to create two counter-rotating, spiral flows. In addition, it also enhances the transverse velocity into the bottom surface, which helps deliver fresh analyte to the sensor. We propose using a the herringbone channel structure to

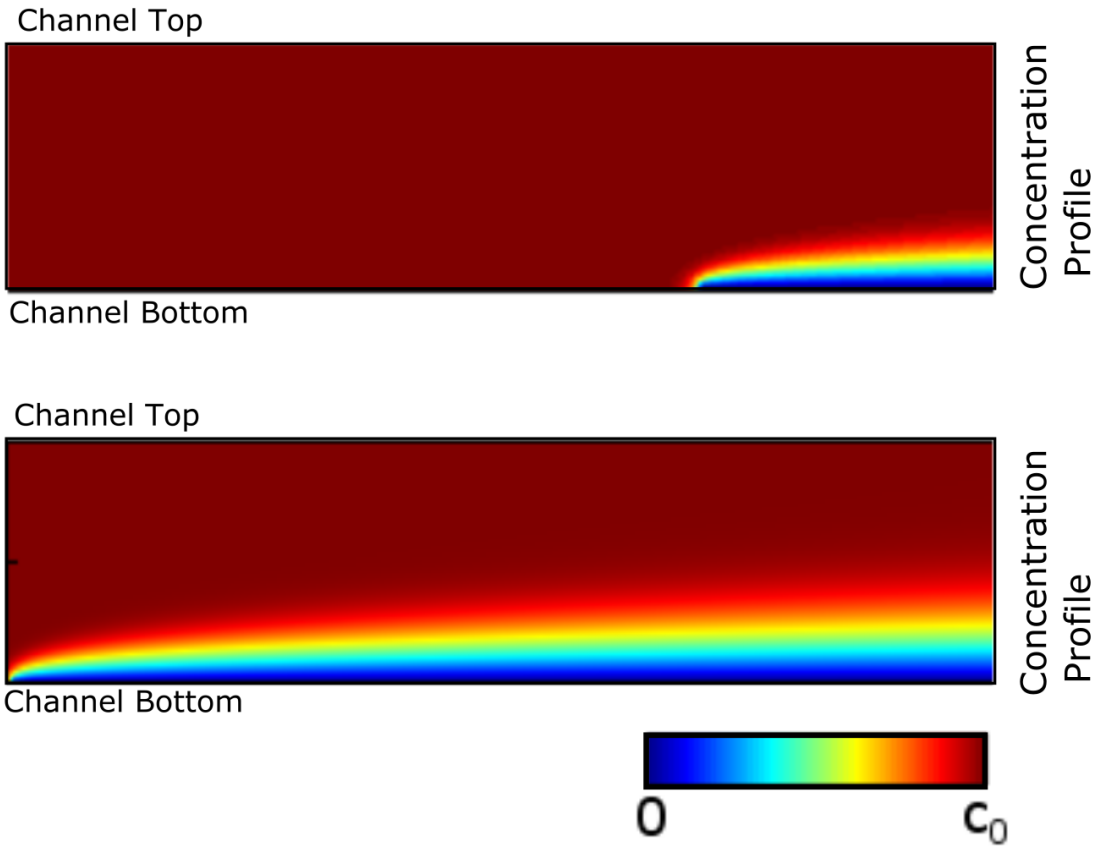

Figure 5.2: a) Development of the concentration boundary layer if the entire bottom surface of the channel is reactive. b) Development of the concentration boundary layer if only the resonator surface is reactive.

increase the flux to the resonator.

Some other groups have tested the herringbone mixer for enhancing surface delivery of analyte, either SPR response [5] or dielectrophoretic microconcentrator performance [6]. However, both groups were mainly interested in increasing the binding over the entire bottom surface of the channel, not at a specific location as needed for the microresonator. Foley *et al.* calculated the spatially averaged binding of streptavidin to the channel bottom, and noticed no improvement over a straight rectangular microchannel [5]. However, they did notice an increase in binding close to the channel midline, and a reduction in binding next to the channel sidewalls. Lee *et al.* modeled the motion of particles subject to helical flow generated by the herringbone, and exposed to the electric field generated by interdigitated electrodes [6]. They concluded that the optimal shape of the herringbone for achieving higher trapping of particles on IDEs is different that the shape used for enhanced mixing. In our platform, since the surface area of the resonator is smaller than the width of the channel, we predict localized flux enhancement to the sensor. In terms of localized flux enhancement, Lynn *et al.* studied the effect of a semiloop structure, but found only modest enhancement factors

[7].

In this chapter we focus on optimizing the localized flux to the resonator by a herringbone structure. At first we study a one-groove geometry, and derive intuition on the parameters that influence the performance of the groove. Next, we make small changes to the shape in order to further increase the flux. Lastly, we test a multiple-groove geometry with both straight chevrons and modified chevrons.

5.2 Governing equations and boundary conditions

In this section, we review the governing equations and their respective boundary conditions. Initially we derive the velocity and pressure fields in steady state, by solving the steady-state Navier Stokes equation in the low-Reynolds number laminar-flow regime. The momentum conservation equation (Navier-Stokes) reads:

$$\rho(\frac{\partial \mathbf{u}}{\partial t} + \mathbf{u} \cdot \nabla \mathbf{u}) = -\nabla p + \mu \nabla^2 \mathbf{u}.$$

The total mass conservation (continuity equation) for an incompressible fluid reads:

$$\nabla \cdot \mathbf{u} = 0.$$

The flow of the fluid is assumed to be unaffected by the concentration of solute, allowing us to independently solve for the flow profile. The fluid carries along the solute, which obeys the convection-diffusion equation:

$$\frac{\partial c}{\partial t} = D\nabla^2 c - \mathbf{u} \cdot \nabla c.$$

We will solve the convection-diffusion equation in two regimes: (i) assuming perfect collection at the resonator surface or wall, and (ii) including finite-rate reaction kinetics. In the perfect collection case, we set $c = 0$ at the resonator or wall, and solve the steady-state convection-diffusion equation to obtain the flux corresponding to infinite-rate binding kinetics. In the finite-rate kinetics case, we assume that at the surface of the resonator the adsorption of the analyte obeys first order Langmuir kinetics:

$$\frac{\partial c_\mathrm{s}}{\partial t} = k_\mathrm{on} c|_\mathrm{wall}(\Gamma - c_\mathrm{s}) - k_\mathrm{off} c_\mathrm{s},$$

where c_s is the surface concentration of target molecules bound to the sensor surface, k_on and k_off are the binding and unbinding rate constants, Γ is the density of available binding sites, and $c|_\mathrm{wall}$ the fluid-phase concentration of the analyte evaluated at the reactive wall. The first term accounts for the binding of molecules to the sensor, which depends on the concentration in solution near the wall and the number of unoccupied binding sites. The second term accounts for the unbinding of previously adsorbed molecules, which depends on the surface concentration and the unbinding rate

constant. If the transport were reaction-limited ($Da \ll 1$), the loss of solute to the surfaces does not significantly deplete the fluid phase. In this case, we can approximate $c|_{\text{wall}} \approx c_0$. The Langmuir equation can thus be solved to yield:

$$c_{\text{s}}(t) = \Gamma \left(\frac{c_0/K_{\text{D}}}{1 + c_0/K_{\text{D}}} \right) \left(1 - e^{-(k_{\text{on}} c_0 + k_{\text{off}})t} \right),$$

where $K_{\text{D}} = k_{\text{off}}/k_{\text{on}}$ is, by detailed balance, the equilibrium constant for the desorption reaction. We notice that a concentration $c_0 \gg K_{\text{D}}$ will saturate the sensor in steady state, whereas a low concentration $c_o \ll K_{\text{D}}$ leaves unoccupied receptors at steady state. The initial slope of the binding curve can be used to extract the bulk concentration if the binding rate constant is known [8]. Assuming the resonator response is proportional to the bound concentration:

$$\frac{dS}{dt} = \alpha k_{\text{on}} c_0 e^{-(k_{\text{on}} c_0 + k_{\text{off}})t},$$

$$lim_{t \to 0} \frac{dS}{dt} = \alpha k_{\text{on}} c_0,$$

where α is the proportionality constant between the sensor response and the surface bound concentration, and can be determined from calibration experiments using known concentrations of the target analyte.

As in [5], we will use the streptavidin-biotin interaction, with $k_{\text{on}} = 4 \times 10^7 \text{M}^{-1}\,\text{s}^{-1}$ and $k_{\text{off}} = 3 \times 10^{-6} \text{s}^{-1}$ which gives an equilibrium constant of $K_{\text{D}} = 77\,\text{fM}$. So for concentrations $c_0 \gg 77\,\text{fM}$, the resonator surface will be fully saturated at steady state, but for lower concentrations, only a fraction c_0/K_{D} will be bound. Using the rate constant, we derive a Damkóhler number $Da = 532$, which indicates that we are operating in the diffusion-limited regime.

Next, we review the boundary conditions used for both the Navier-Stokes equation and the convection-diffusion equation. In the case of the Navier-Stokes equation, we assume the flow into the channel to be a fully developed laminar flow with a set average velocity. The outlet condition is set to reflect no viscous stress ($p = 0$), and the walls are set to be no-slip boundaries ($v = 0$). The convection-diffusion equation is solved in the case of infinite-rate kinetics with a fixed concentration $c = c_0$ at the inlet boundary. The reactive surfaces are set to $c = 0$, and the non-reactive surfaces are set to be insulating (zero normal flux). In the case of Langmuir kinetics, to avoid inconsistent solutions, we ramp the inlet concentration from 0 to c_0 using a smoothed step function over a $\Delta t = 2\,\text{s}$. The reactive surfaces are set to have a normal flux proportional to Langmuir binding rates presented above.

5.3 COMSOL Simulations

5.3.1 Convergence considerations: Mesh size and time step

To determine the flux to the reactive surfaces, we numerically solve the Navier-Stokes and convection-diffusion equations using COMSOL. When setting up the simulations, we must be careful about the Cell Péclet number. Similarly to the Péclet number for the overall channel flow, the Cell Péclet number expresses the relative importance of convection versus diffusion, but with the velocity, and length scale determined within the computational cell. In order for the convection-diffusion equation to be numerically stable, $\mathrm{Pe}_{\mathrm{cell}}$ should be smaller than 2. This imposes a constraint on the grid size. To increase stability, we also included streamline and crosswind stabilization methods.

The meshes employed for solving the Navier-Stokes and for solving the Convection-Diffusion-Reaction modules must be refined in the regions where the gradients are largest. In the case of the fluid profile, we increase the mesh density close to the walls, where the velocity gradient is highest. The mesh for the Convection-Diffusion-Reaction module is finer than the one used to compute the flow profile, and is refined close to the adsorbing surface. In both modules we scale the shorter dimension by a factor of 5 to add proportionally more grid nodes per unit length in that direction compared to the other directions, since the aspect ratio of the channel is 1:10 and we require a dense mesh throughout the geometry. In the case of time-dependent Convection-Diffusion-Reaction, we optimize the time step of the solver to achieve numerical stability.

In order to gain confidence in the solutions given, we perform mesh-independence tests, which support the validity of the results. The simulations were performed in COMSOL Multiphysics$^{\mathrm{TM}}$, on a server with 32 64-bit AMD processsors and 256 GB DDR-2 RAM. The simulation parameters were sent to COMSOL via Matlab Livelink through a Matlab script, and the solutions were recorded in Matlab as well.

We summarize the boundary conditions described above, and show their formulation in COMSOL. Table 5.1 shows the boundary conditions required to solve the Navier-Stokes equation.

Parameter	Boundary Condition	Description
Inlet	$L_{\mathrm{entr}}\nabla_t \cdot [-p\mathbf{I} + \mu(\nabla_t \mathbf{u} + (\nabla_t \mathbf{u})^T = p_{\mathrm{entr}}\mathbf{n}$	Laminar Inflow
Outlet	$[-p\mathbf{I} + \mu(\nabla \mathbf{u} + (\nabla \mathbf{u})^T)]\mathbf{n} = -\hat{p_0}\mathbf{n}, \hat{p_0} \leq p_0$	p=0
Wall	$\mathbf{u} = 0$	No slip

Table 5.1: Boundary conditions for the steady state laminar flow equations.

The boundary conditions for solving the finite-rate convection-diffusion equation are shown in Table 5.2, where $\mathbf{N} = -D\nabla c + \mathbf{u} \cdot c$.

To insure that the boundary conditions at time $t = 0$ do not generate infinite gradients, we ramp the inlet concentration using a smoothed Heaviside function with a continuous second derivative without overshoot, represented by the function $flc2hs$ in COMSOL.

Parameter	Boundary Condition	Description
Inlet	$c = c_0 \cdot \text{flc2hs}(t - t_o, t_o)$ with $t_o = 2s$	Inflow
Outlet	$-\mathbf{n} \cdot D\nabla c = 0$	Outflow
Wall	$\mathbf{n} \cdot \mathbf{N} = 0$	No flux
Reactive Wall	$\mathbf{n} \cdot \mathbf{N} = -k_{\text{on}} c\|_{\text{wall}} c_s - k_{\text{off}} c_s$	Flux to Surface

Table 5.2: Convection-diffusion boundary conditions

5.3.2 Geometry parameters

Figure 5.3 shows a typical geometry of the herringbone structure. The channel has height H and width W; the groove has depth d and width a. The angle of the chevron is denoted by θ. If multiple grooves are used, the spacing between adjacent grooves is denoted by b, and their number by N. Table 5.3 summarized the ranges of the parameters used in the simulations.

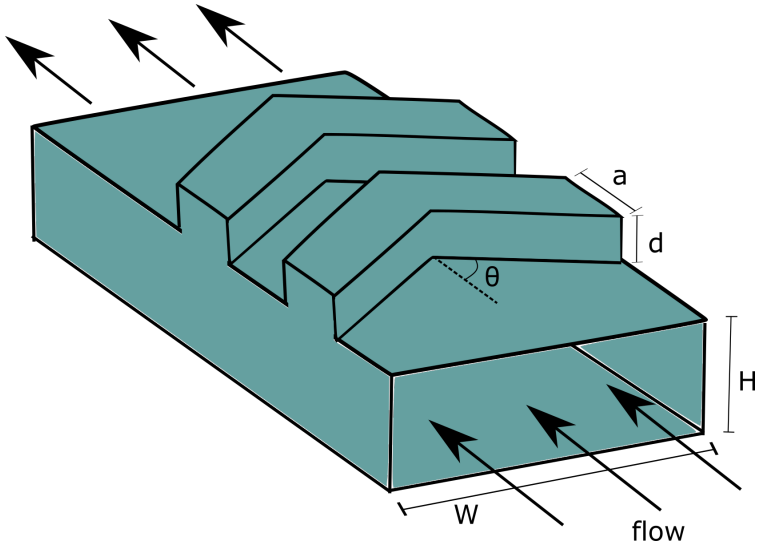

Figure 5.3: Schematic geometry of channel with two chevrons.

Parameter	Description	Value Range
H	Height of channel	20, 40 µm
W	Width of channel	400 µm
a	Width of groove	60-300 µm
d	Depth of groove	20-160 µm
θ	Groove angle	30-90^o
L_o	Starting position of groove	20-200µm
b	Groove pitch	40-400 µm
N	Number of grooves	1-10
v_{avg}	Average inlet velocity	0.2-10 mm s^{-1}

Table 5.3: List of parameters and their ranges used in this study.

5.3.3 Theorical calculations of flux in 2D

First, we theoretically determine the species flux to a reactive surface located at the bottom of a parallel plate channel. We assume perfect collection at the reactive surface, which translates into the boundary condition $c = 0$ at $x = 0$. For the fluid profile, we use a fully developed Poiseuille flow with parabolic velocity profile $u = 6U\frac{x(H-x)}{H^2}$, where U is the average velocity of the flow and H the height of the channel. A concentration $c = c_0$ is introduced at the left inlet of parallel plate channel, located at $z = 0$. To determine the flux to the bottom surface, we solve the steady-state convection-diffusion equation:

$$\vec{u} \cdot \vec{\nabla} c = D\nabla^2 c.$$

To non-dimensionalize the coordinates, we define $X = x/H$ and $Z = z/(H\mathrm{Pe})$ where $\mathrm{Pe} = UH/D$. We also define a non-dimensional concentration $\Theta = c/c_0$. The convection-diffusion equation becomes:

$$6X(1-X)\frac{\partial \Theta}{\partial Z} = \frac{\partial^2 \Theta}{\partial X} + \frac{1}{Pe^2}\frac{\partial^2 \Theta}{\partial Z^2}.$$

Typical parameters used in the simulations are $H = 20\,\mu\mathrm{m}$ and $U = 1\,\mathrm{mm\,s^{-1}}$, so the Péclet number in the case of streptavidin flow is $\mathrm{Pe} \approx 270$. Since the Péclet number is $\mathrm{Pe} \gg 1$, we can ignore the $1/Pe^2$ term. Therefore:

$$\frac{\partial \Theta}{\partial Z} = \frac{1}{6X(1-X)}\frac{\partial^2 \Theta}{\partial X^2}.$$

We assume that the boundary layer is much smaller than the height of the channel H. In the boundary layer region, which is close to the wall at $X = 0$, the velocity can be approximated as a linear function in X, so we can ignore the $1 - X$ term. Thus,

$$\frac{\partial \Theta}{\partial Z} = \frac{1}{6X}\frac{\partial^2 \Theta}{\partial X^2}.$$

A similarity solution $\Theta(X, Z) = F(\eta)$ exists, where $\eta = X/f(Z)$. For this system, $f(Z) = Z^{1/3}$, and the similarity parameter becomes $\eta = X/Z^{1/3}$, yielding the solution

$$F(\eta) = \left(\frac{2}{3}\right)^{1/3} \frac{1}{\Gamma(\frac{4}{3})} \int_0^\eta \exp(-2\eta^3/3) d\eta.$$

The flux to bottom wall, $J(z) = -D(\partial C/\partial x)$, is then found to be

$$J(z) = \frac{DC_o}{\Gamma(\frac{4}{3})} \cdot \left(\frac{2U}{3DH}\right)^{1/3} z^{-1/3}.$$

This formula for the flux shows the importance of placing the resonator as close to the inlet as possible, to keep z small. Furthermore, it shows a difference between the perfect collection and Langmuir kinetics case. In the perfect collection case, the flux does not change over time. In the

Langmuir kinetics case, as the upstream binding sites are occupied and the surface saturates, the "perfect collection" front shifts downstream over time, such that $z' = z - v_{\text{front}}t$ defines the moving front. The calculated Sherwood number for this case of perfect collection is:

$$Sh(z) = \left(\frac{z}{PeH}\right)^{1/3}.$$

Further theoretical analysis can be found in [9] [1] [10] [11] [12].

5.3.4 Effect of chevron on streamlines and flux to bottom surface

The chevron has been introduced as a way to stretch and fold the fluid streamlines in order to achieve better mixing. In Figure 5.4 we exemplify the effect of a single chevron on the fluid streamlines, depending on their distance from the grooved surface. The streamlines located $H/4$ from the grooved surface are affected more than the ones located $H/2$ and $3H/4$ away. The streamlines closest to the side walls experience higher lateral displacement compared to streamlines closer to the midline of the channel.

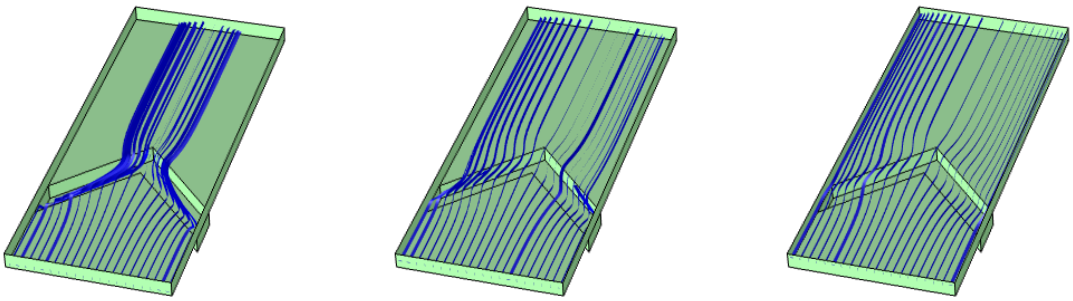

Figure 5.4: (a) Streamlines closes to the top of the channel are deflected most by the groove. (b) Streamlines in the middle of the channel are deflected. (c) Streamlines close to the bottom of the channel are not deflected.

Figure 5.5 shows the total flux to the midline of the channel bottom surface for a straight rectangular channel and a channel with one groove. The flux to the surface around the position of the tip of the chevron (the chevron is located on the top surface of the channel) was enhanced by about a factor of 2.5. For the rest of the simulations, we will focus on the maximum flux to the bottom surface midline, as a measure of the performance of the groove.

From the theoretical flux equation, we can infer that the flux is proportional to $U^{1/3}$ and inversely proportional to $H^{1/3}$, therefore to achieve the greatest flux improvement, we should reduce the channel height and increase the fluid velocity. This is possible up to a limit: too high of a velocity and pressure might lead to delaminate the PDMS from the substrate, and too small a height could lead to channel collapse or clogging. Therefore, for a given velocity and height of channel, the herringbone can enhance the mass transport. We will investigate the influence of velocity and channel height

as well, in order to understand the conditions under which the herringbone is most effective, and to identify conditions that would maximize the enhancement at low velocities. Furthermore, to compare the effect of different herringbone structures, we will reference the maximum flux in the patterned geometry to the flux in a channel without grooves. This referencing helps us achieve fair comparisons between different geometries of grooved channels. In the case of one groove, the referencing is straightforward. In the case of multiple grooves, another issues arises. By placing the sensor farther downstream, the reference flux is reduced, so the relative influence of the herringbone will change depending on its location. To exemplify this, Figure 5.6 shows the enhancement for the same groove structure of $a = 120\,\mu\text{m}$ and $d = 40\,\mu\text{m}$ as the groove tip is shifted downstream in increments of $100\,\mu\text{m}$. At a location of $0.5\,\text{mm}$, the enhancement factor is 2.6 whereas at a location $0.8\,\text{mm}$, it is 2.8. This effect is due to the fact that the reference flux decreases faster than the groove effect.

5.3.5 Geometrical parameter sweep for single groove

Even for a single chevron groove, there are a number of parameters that can influence its effect on the enhancement of the mass transport, including channel geometry parameters, groove geometry parameters, or fluid flow parameters. The main channel parameters are the channel height H and the channel width W. In all the simulations we use $W = 400\,\mu\text{m}$, and we test two channel heights: $H = 20\,\mu\text{m}$ and $H = 40\,\mu\text{m}$. As we saw in the $\text{Re} = 0$ case in 2D, the flux to the bottom surface is expected to vary as $H^{1/3}$, so the channel height has a large influence on the flux. Therefore, to achieve a fair comparison between different geometries, we reference the flux to the bottom of the

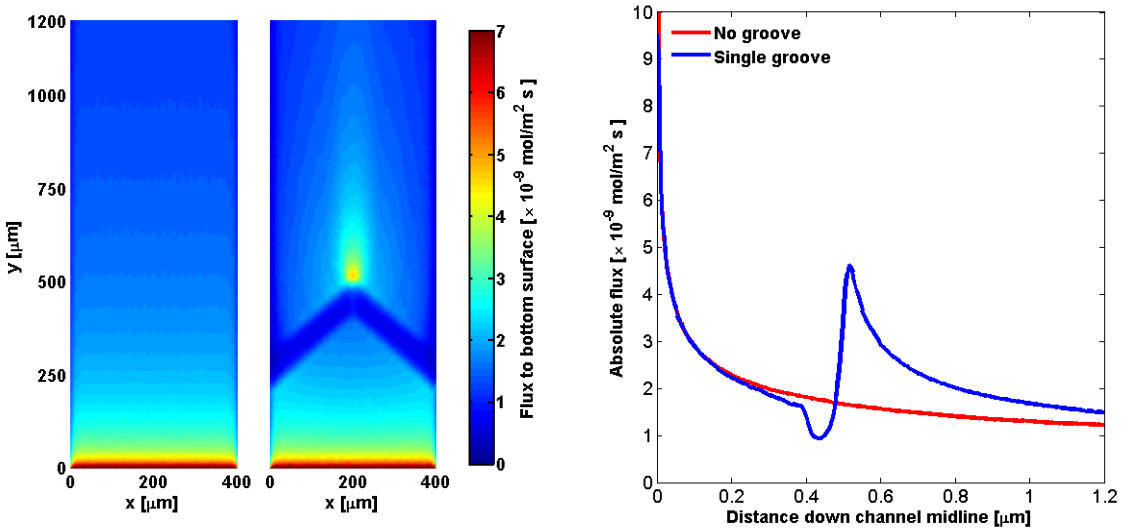

Figure 5.5: Effect of one groove on the flux along the midline of the channel.

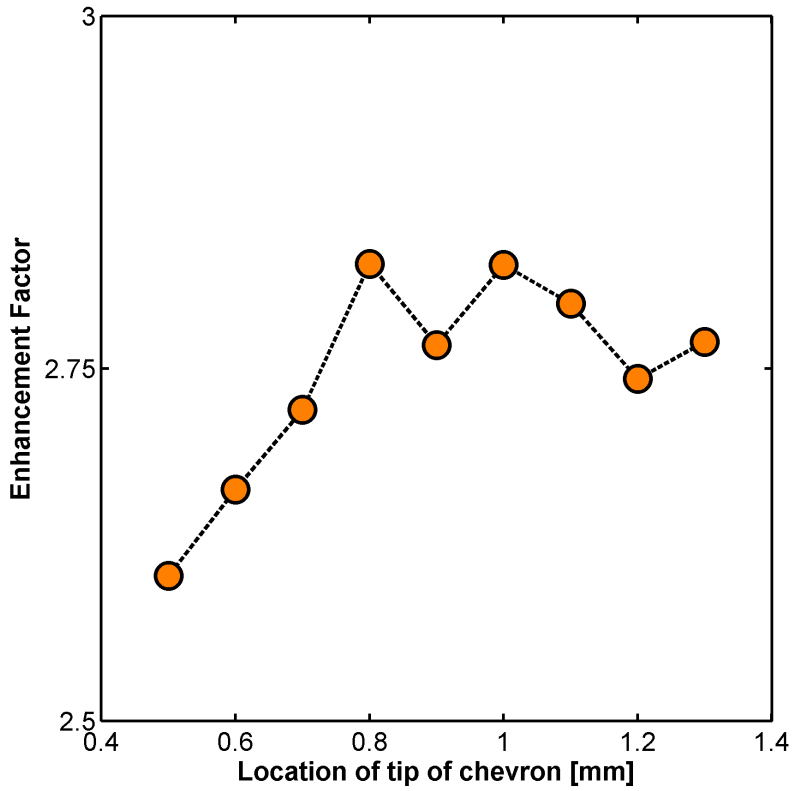

Figure 5.6: a) Flux enhancement factor for a groove of width $a = 120\,\mu\text{m}$ as the groove is shifted downstream.

surface to that in the case of a rectangular channel of the same height H, width W and average inlet fluid velocity U. All simulations are conducted at $c_0 = 1\,\text{nM}$.

To test the effect of a single groove on mass transport enhancement, we test geometries with one chevron located on the channel top with its tip fixed at a location $500\,\mu\text{m}$ downstream from the channel inlet. Since we are interested in enhancement factor of the chevron over a straight rectangular channel, we divide the maximum flux to the bottom surface in the single chevron case by the flux at the same location in a straight channel. The maximum flux in the case of the chevron is located very closely to the tip position, with slight variations. By keeping the tip of the chevron fixed, we insure that all referencing is to roughly the same value, which enables a fair comparison. Ideally, we should also fix the overall footprint of the chevron. However, in the case of a single chevron this is not possible. For a chevron of width a and angle θ, the footprint is $L_t = a + W/(2\tan(\theta))$. For multiple-groove geometries, we can keep the overall footprint fixed by compensating changes in one parameter to changes in other parameters.

First we examine the effect of the inlet velocity on the mass transport enhancement factor for a single chevron. Figure 5.7 shows enhancement factors for two different groove widths located in a

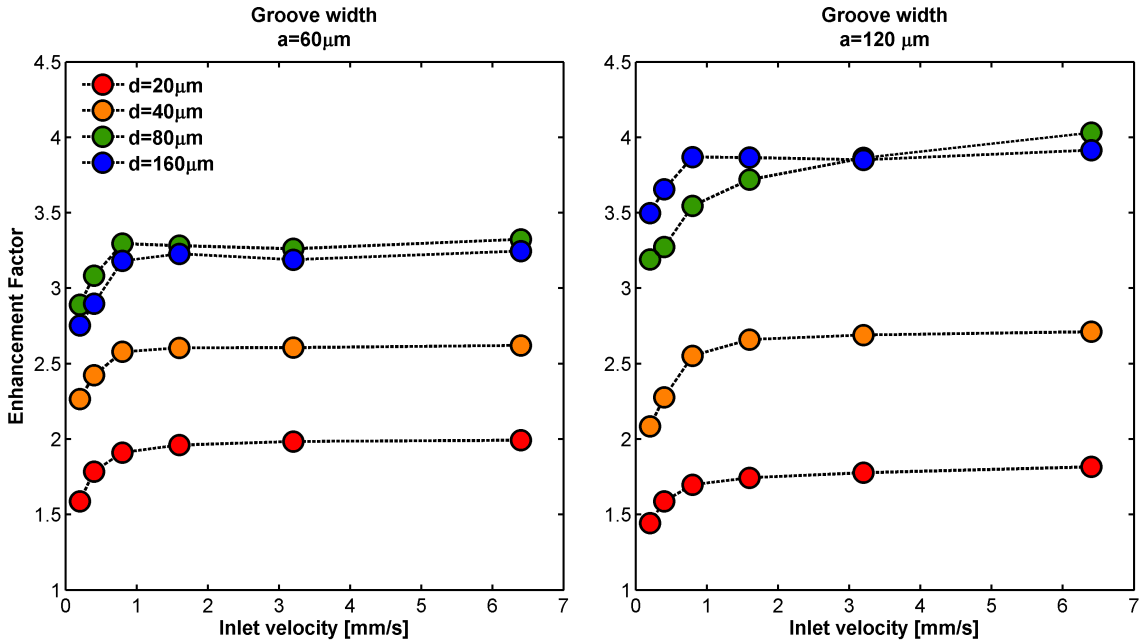

Figure 5.7: a) Flux enhancement factor for a groove of width $a = 60\,\mu\text{m}$ for four different groove depths as a function on inlet velocity. b) Flux enhancement factor for a groove of width $a = 120\,\mu\text{m}$ for four different groove depths as a function on inlet velocity.)

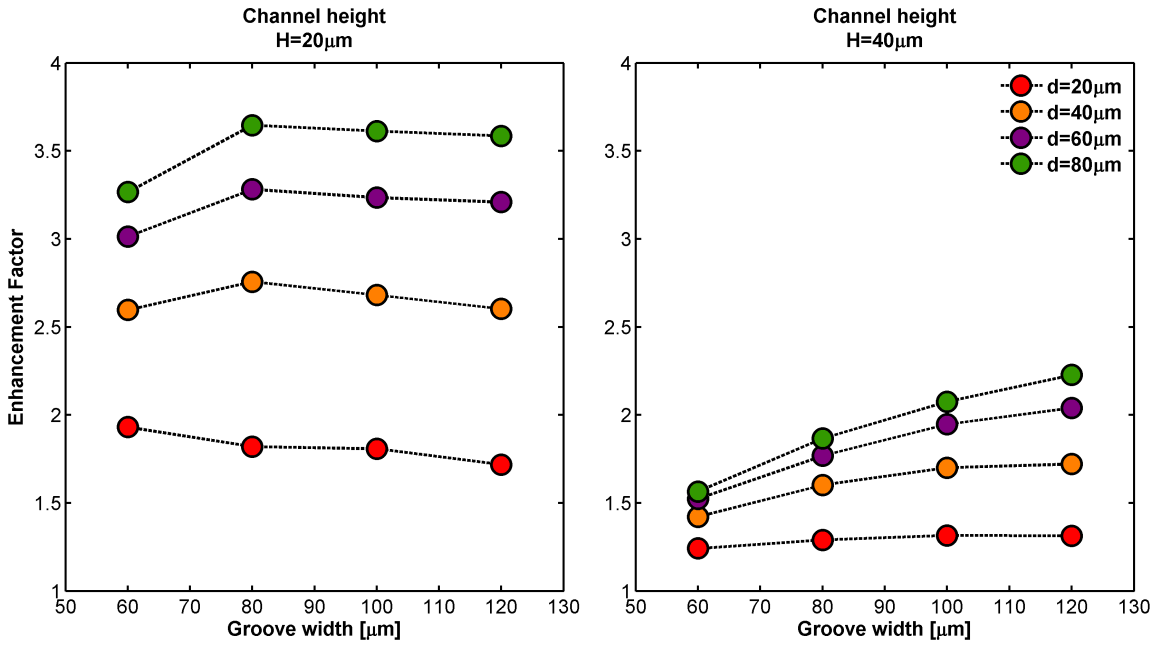

Figure 5.8: Flux enhancement factor as a function of groove width a for four different groove depths. The left plot is for a channel height $H = 20\,\mu\text{m}$, and the right plot for a channel height of $H = 40\,\mu\text{m}$

channel of height $H = 20\,\mu\text{m}$. All enhancement factors are referenced to the straight channel fluxes at the respective velocities. We set the width groove to be $a = 60\,\mu\text{m}$, and calculate the maximum flux to the bottom surface for four different groove depths: $20\,\mu\text{m}$, $40\,\mu\text{m}$, $80\,\mu\text{m}$, and $160\,\mu\text{m}$. We

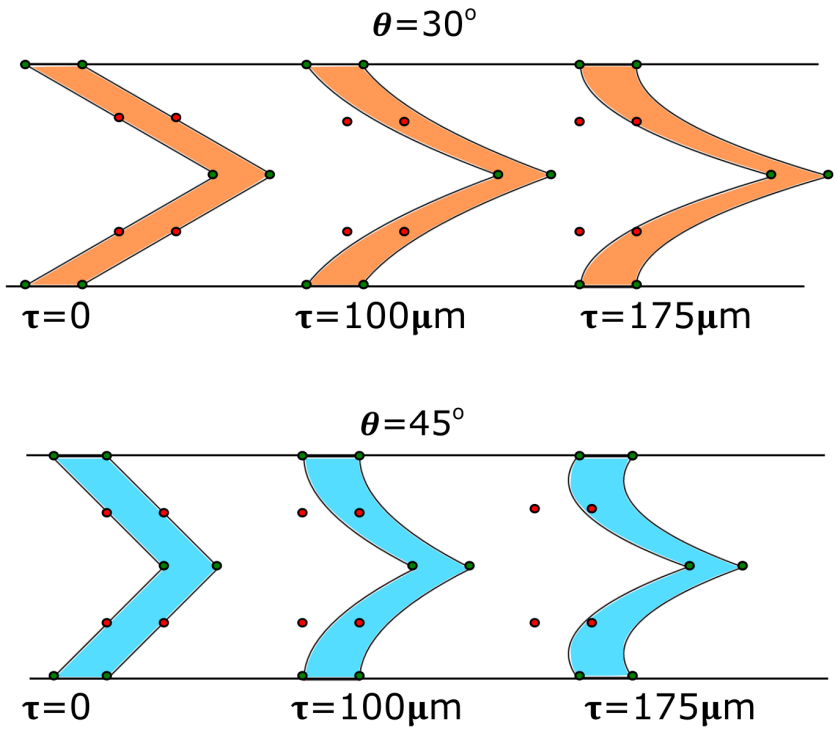

Figure 5.9: Bezier curves for defining new chevron shapes.

notice that as the groove depth increases, the effect of the groove and thus the enhancement factor also increases. However, past a depth of $d = 80\,\mu\text{m}$, the enhancement factor levels off. This behavior is to be expected, since the fluid streamlines will not penetrate that deep into the groove. A groove depth of $160\,\mu\text{m}$ for a channel height $H = 20\,\mu\text{m}$ gives an aspect ratio of $8:1$, which would be difficult to fabricate from PDMS, but we explored it to confirm our intuition that the enhancement levels off after a certain groove depth. We will continue to test groove depths from $20\,\mu\text{m}$ to $80\,\mu\text{m}$ in our simulations, but given similar enhancement factors, we will prefer the geometries with a shallower grooves, $20\,\mu\text{m}$ and $40\,\mu\text{m}$, due to ease of fabrication.

In the same figure, we test a different groove width, $a = 120\,\mu\text{m}$, which presents a similar trend as the groove with $a = 60\,\mu\text{m}$. Beyond a groove depth of $d = 80\,\mu\text{m}$ the enhancement levels off, but at a higher value than in the shorter groove. Our next observation is that past a velocity of $U = 1\,\text{mm}\,\text{s}^{-1}$, the enhancement levels off. In simulations that follow we will keep the average inlet velocity at $U = 1\,\text{mm}\,\text{s}^{-1}$ for this reason. For a channel height $H = 20\,\mu\text{m}$, the reference flux at this velocity is $J = 7.1 \times 10^{-10}\text{mol}\,\text{m}^{-2}\,\text{s}^{-1}$. We expect that increasing the velocity beyond a critical value will reduce the enhancement because the flow will not have enough time to interact with the grooves. Next we focus on the geometrical parameters of the chevron, namely the width a, and the depth d. Figure 5.8 shows the influence of chevron parameters on the enhancement factor for

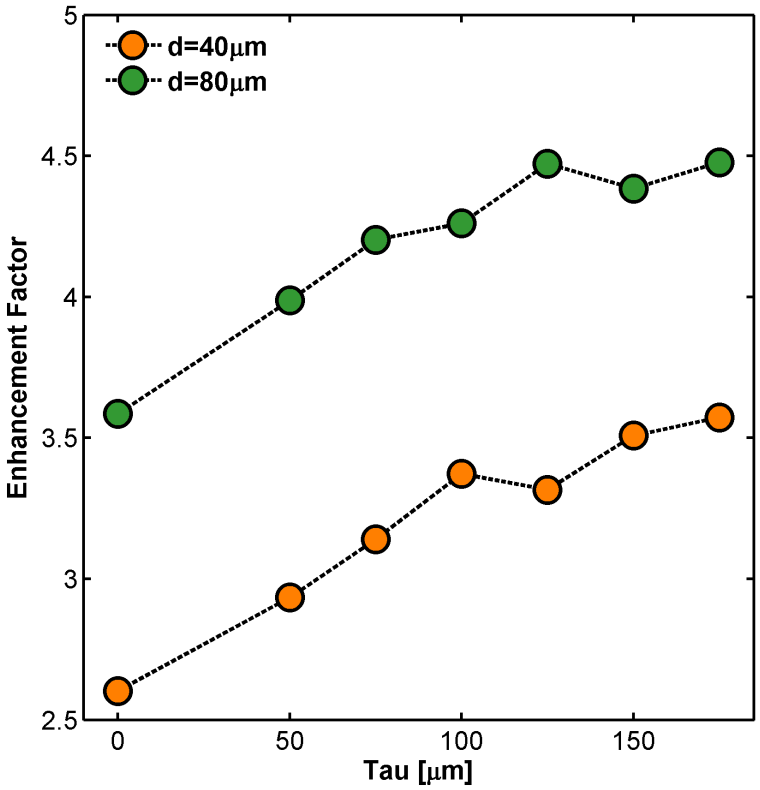

Figure 5.10: Improvement as function of depth of groove

two channel heights: $H = 20\,\mu m$ and $H = 40\,\mu m$. The first observation is that the smaller channel height leads to higher enhancement factors than observed for the taller channel, *i.e.*, the influence of the groove is higher when it is closer to the bottom surface. In both figures, as the depth d increases, so does the enhancement factor. As the width of the groove increases, the enhancement factor also grows, but it also levels off for the smaller channel height. We conclude that, for a single groove, there is an increase in the maximum flux enhancement to the bottom surface as we increase the groove depth and width, but only up to a certain point. We now explore the influence of the shape of the herringbone. Instead of a straight line that defines the chevron shape, we tried a Bezier curve with three control points, fixing the control points at the sides, since we want to fix the overall footprint of the chevron. We allow the middle control point to be moved upstream by a distance τ. Figure 5.9 shows the shapes of grooves as the control points are moved upstream by a distance τ, in the case of a groove with angle $\theta = 30^o$ and $\theta = 45^o$. The τ values shown are for $\tau = 0$, $\tau = 100\mu m$, and $\tau = 175\mu m$. We restrict the values of τ to this range because larger τs would change the footprint of the chevron.

The influence of the change in chevron shape is shown in Figure 5.10 for a groove of width $a = 120\,\mu m$, angle $\theta = 45^o$, and depths $d = 40\,\mu m$ and $d = 80\,\mu m$, for τ varying from 0 to $175\,\mu m$. As τ increases, so does the flux to the sensor. In the case of the groove with $d = 40\,\mu m$, the

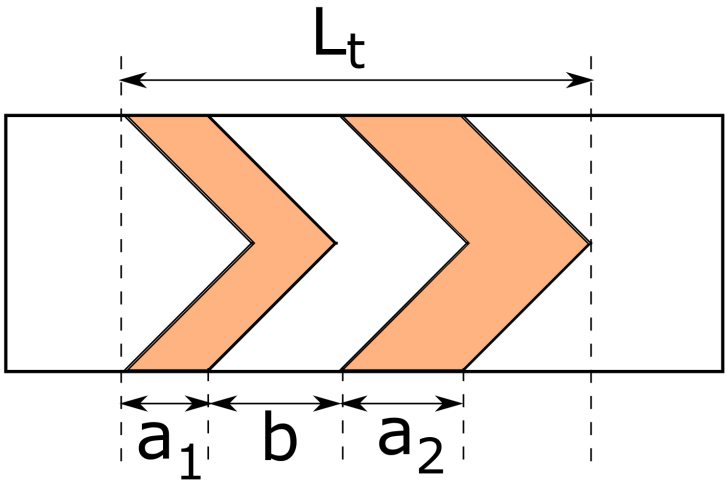

Figure 5.11: Schematic of two-groove herringbone, showing the overall footprint of the structure

enhancement increases from a factor of 2.5 to 3.5 and in the case of $d = 80\,\mu\text{m}$ from a factor of 3.5 to 4.5.

5.3.6 Optimization of two-chevron geometry

For a single chevron, the depth d, the width a, the angle, θ and the Bezier parameter τ influence the transverse velocity to the bottom surface. After deriving some intuition for a single groove, we test multiple groove geometries, which introduce additional parameters: the spacing b between the grooves and number of grooves N.

We investigate the enhancement of the flux to the sensor by the addition of a second groove. We define $L_\text{a} = a_1 + a_2$ where a_1 and a_2 are the widths of the first and second groove, and b the spacing between the two grooves. Figure 5.11 shows the footprint of the structure, which is $L_t = a + b$. In trying to achieve a fair comparison, we keep L_t constant, while varying the spacing and width of the grooves. The location of the tip of the last groove is 900 µm downstream from the channel inlet. In a rectangular channel with $H = 20\,\mu\text{m}$, $U = 1\,\text{mm}\,\text{s}^{-1}$, and inlet concentration of $c = 1\,\text{nM}$, the flux to the bottom surface at this location would be $J = 5.52 \times 10^{-10}\text{mol}\,\text{m}^{-2}\,\text{s}^{-1}$. We first keep the spacing b between the grooves the same, while increasing the width of the first groove at the expense of the second groove.

First, we look at different angles θ of the grooves. In Figure 5.12 we plot the maximum flux as a function of the last groove width a_2 for three different angles: $\theta = 30^o$, $\theta = 45^o$, and $\theta = 60^o$. The width of the last groove has the largest effect on the flux compared to the other grooves. The depth of the grooves is $d = 20\,\mu\text{m}$. We notice an increase in the flux as the angle is decreased. The largest

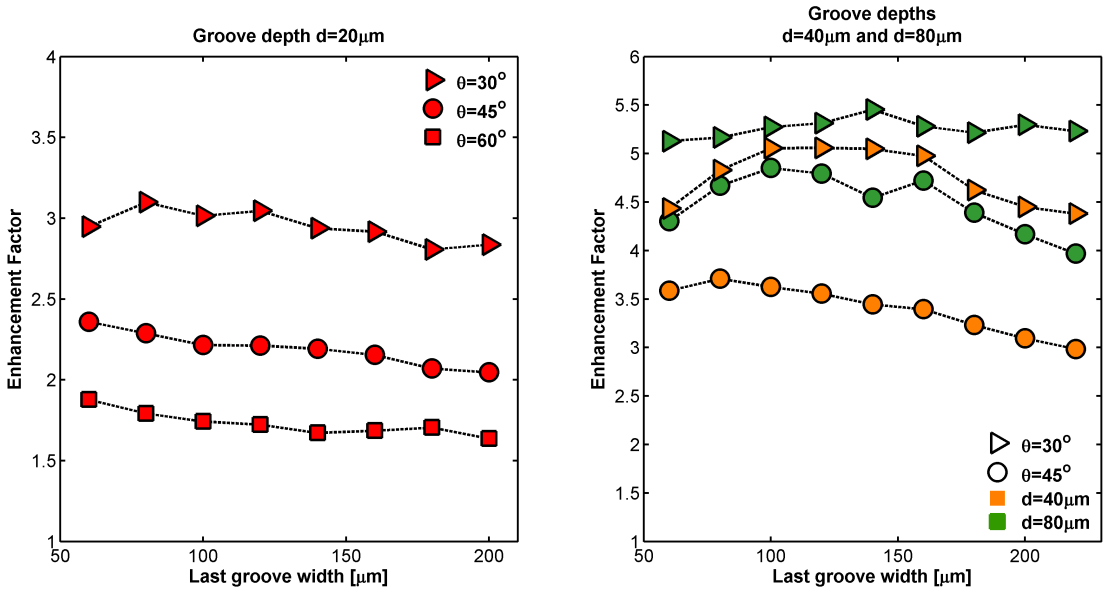

Figure 5.12: Flux improvement for a two-groove geometry with $d = 20\,\mu\text{m}$, $d = 40\,\mu\text{m}$, and $d = 80\,\mu\text{m}$.

flux enhancement is for $\theta = 30^o$, compared to $\theta = 45^o$ and $\theta = 60^o$. However, the enhancement factor seems to be insensitive to the width of the groove.

The same figure shows the enhancement factor for the same geometry with two grooves, but with groove depths $d = 40\,\mu\text{m}$, and $d = 80\,\mu\text{m}$, which lead to higher overall enhancement factors than in the $d = 20\,\mu\text{m}$ case. The angle $\theta = 30^o$ leads to the highest flux enhancement. Surprisingly, the

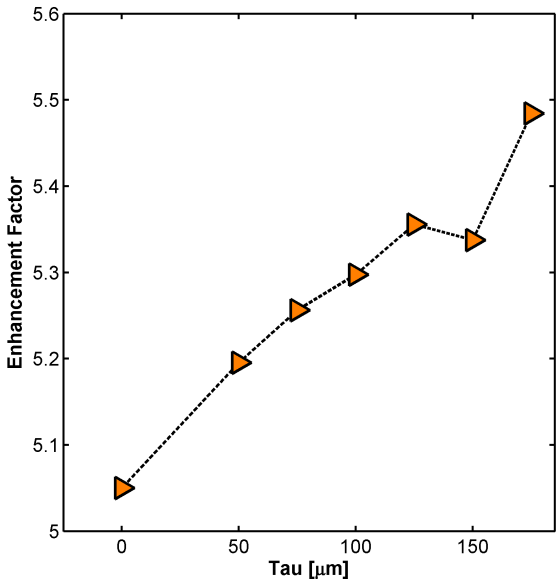

Figure 5.13: Flux improvement for a two-groove geometry with Bezier shape.

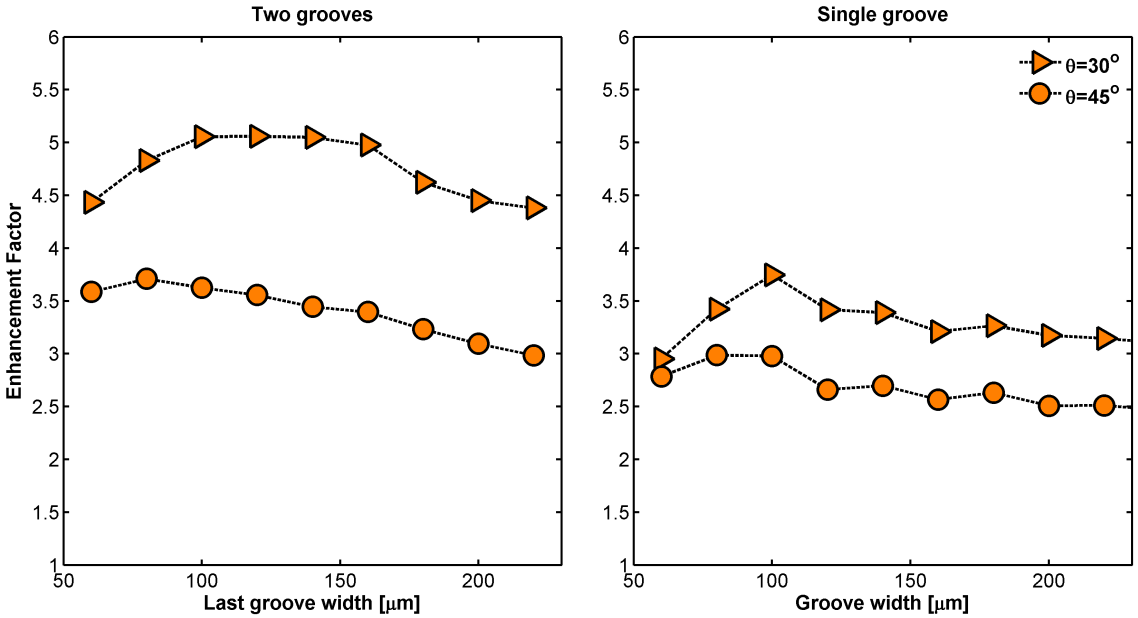

Figure 5.14: Flux improvement for a two groove geometry compared to a one groove geometry composed of only the last groove.

groove with angle $\theta = 30^o$ and depth $d = 40\,\mu m$ leads to higher enhancement than the grooves with $\theta = 45^o$ and $d = 80\,\mu m$, suggesting that a reduction in angle contributes more to the enhancement factor than a doubling of the groove depth. We explore the geometry with $\theta = 30^o$ and $d = 40\,\mu m$, since it is more feasible for fabrication than the $d = 80\,\mu m$ geometries. We focus on the optimal enhancement for this condition, which results in grooves widths of $a_1 = a_2 = 140\,\mu m$. The enhancement factor obtained in this case is 5.05. We also note that changing the angle θ while keeping the footprint of the two-groove structure fixed implies that the spacing b between the grooves changes.

Next we optimize the shape of the grooves by using the same Bezier curve for each groove. Figure 5.13 shows the enhancement variation as τ changes in steps of $25\,\mu m$ from $50\,\mu m$ to $175\,\mu m$. We notice an increase in the enhancement factor from 5.05 to 5.5, about a 10% improvement.

We also want to show the added enhancement due to the addition of a second groove, as opposed to just placing a single groove at the same location. To this end, we show enhancement factors in a geometry where only the last groove of the previously described two groove herringbone is employed. Figure 5.14 shows the enhancement that results from the concerted folding and stretching of the flow due to the two grooves. The two conditions studied are for $d = 40\,\mu m$, and angles $\theta = 30^o$ and $\theta = 45^o$. The enhancement increases by 50% for some conditions.

Lastly, we test a three-groove geometry with equal spacing and widths of grooves $a_1 = a_2 = a_3 = b_1 = b_2 = 100\,\mu m$, with angle $\theta = 45^o$. The results are shown in Figure 5.15. We slightly modify

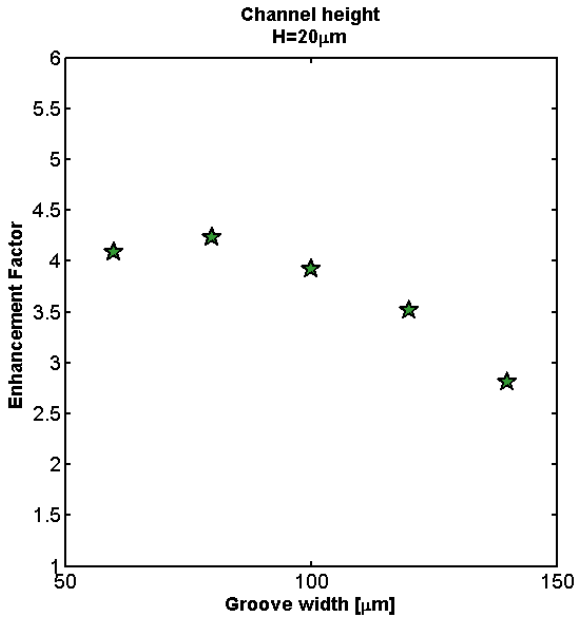

Figure 5.15: Flux improvement for a three-groove geometry as we vary the last groove width.

the width of the last groove to observe any trends in the enhancement factor. The three-groove geometry shows better enhancement than the two-groove geometry with the same angle, but still poorer performance than the two-grooved Bezier geometry.

5.3.7 Optimization of four-chevron geometry

Next we look at a geometry with four chevrons where $a = a_1+a_2+a_3+a_4 = 820$µm and $b = b_1+b_2+b_3 = 120$µm, for a total footprint of the structure $L_t = L_a + L_b = 940$ µm. First we vary the widths of the grooves and test four conditions: (i) the groove widths are equal $a_1 = a_2 = a_3 = a_4 = 160$ µm; (ii) the groove widths increase slowly progressively: $a_1 = 100$ µm, $a_2 = 140$ µm, $a_3 = 180$ µm, and $a_4 = 220$ µm; (iii) the groove widths increase fast progressively $a_1 = 40$ µm, $a_2 = 120$ µm, $a_3 = 200$ µm, and $a_4 = 280$ µm; (iv) the groove widths decrease slow progressively: $a_1 = 220$ µm, $a_2 = 180$ µm, $a_3 = 140$ µm, and $a_4 = 100$ µm; and (v) the groove widths decrease fast progressively $a_1 = 280$ µm, $a_2 = 200$ µm, $a_3 = 120$ µm, and $a_4 = 40$ µm. For each of these conditions we study three conditions on the spacings b_1, b_2, and b_3: (i) the spacings are equal $b_1 = b_2 = b_3 = 100$ µm; (ii) the groove spacings decrease progressively: $b_1 = 140$ µm, $b_2 = 100$ µm, and $b_3 = 60$ µm; and (iii) the groove widths increase progressively $b_1 = 60$ µm, $b_2 = 100$ µm, and $b_3 = 140$ µm. Figure 5.16 displays the results for all fifteen conditions. In terms of groove widths, the conditions with equal grooves have higher enhancement factors than the ones where the grooves vary in size. In addition, the condition where the groove spacings decrease gives higher enhancement than in the cases where they are constant or increase progressively.

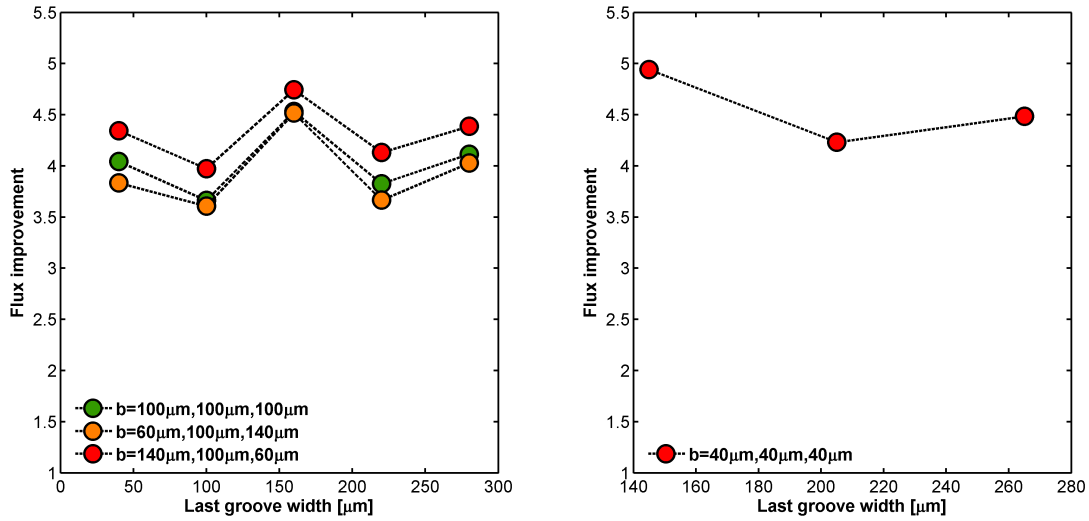

Figure 5.16: Four-groove geometry flux as a function of groove width and spacing.

We also simulate a four-groove structure with the some overall footprint $L_t = 940\mu$m, but where $L_a = 820\mu$m and $L_b = 120\mu$m. The conditions for the groove widths are (i) the widths are equal $a_1 = a_2 = a_3 = a_4 = 205\,\mu$m; (ii) the groove widths decrease progressively $a_1 = 265\,\mu$m, $a_2 = 225\,\mu$m, $a_3 = 185\,\mu$m, and $a_4 = 145\,\mu$m; and (iii) the grooves increase progressively $a_1 = 145\,\mu$m,$a_2 = 185\,\mu$m, $a_3 = 225\,\mu$m, and $a_4 = 265\,\mu$m. The spacing between the grooves is constant $b_1 = b_2 = b_3 = 40\,\mu$m. We do not use smaller spacings since that would require changing the mesh size. Figure 5.16 shows the simulated enhancement factors. The higher enhancement is obtained when the widths of the grooves are progressively decreasing.

Lastly, we study the influence of groove shape on the four-groove geometries. Figure 5.17 shows that further enhancement can be obtained by using Bezier curves with $\tau = 175\,\mu$m for a condition with $L_t = 640\,\mu$m and $L_t = 800\,\mu$m.

5.3.8 Time-dependent studies

In the previous sections we have focused on instantaneous kinetics by setting the boundary condition on the adsorbing surface to $c = 0$. A more complete study includes modelling the binding kinetics of the analyte to the receptor surface using Langmuir kinetics. In our case, we investigate the binding of streptavidin as it flows over an adsorbing surface that has been coated with biotin. The interaction between streptavidin and biotin is characterized by the binding rates $k_{\text{on}} = 4 \times 10^7 \text{M}^{-1}\,\text{s}^{-1}$ and $k_{\text{off}} = 3 \times 10^{-6}\text{s}^{-1}$. We assume a surface density of binding sites $\Gamma = 4 \times 10^8 \text{mol}\,\text{m}^{-2}$. Since the Damköhler number is our case is large ≈ 500, the transport is diffusion-limited. In Figure 5.18 we show the time evolution of the flux at a location 500 μm downstream along the midline of the channel,

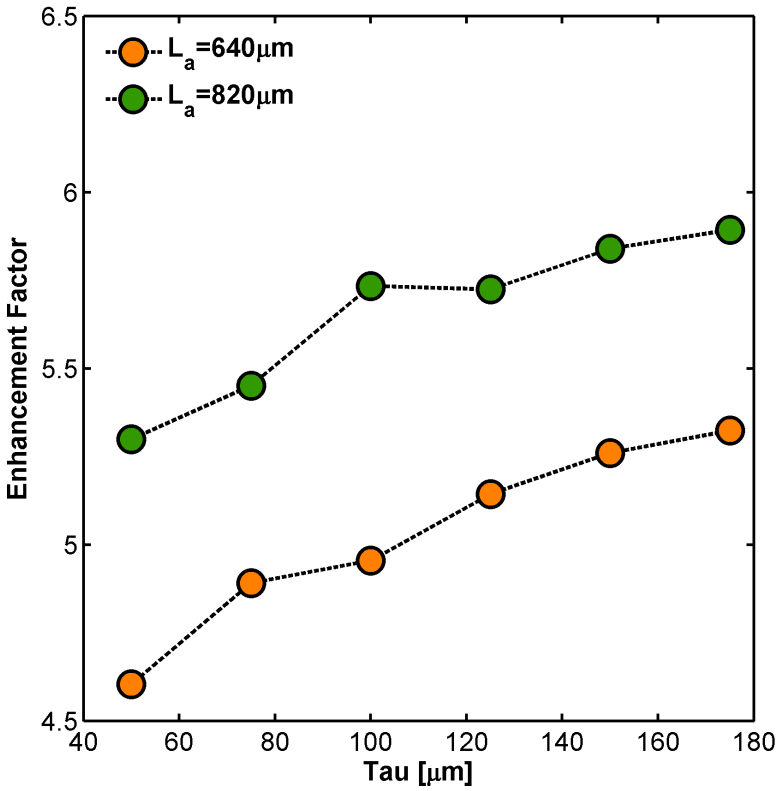

Figure 5.17: Influence of shape of herringbone in four-groove geometry.

for a channel heights $H = 20\,\mu\text{m}$ and $H = 40\,\mu\text{m}$. As the analyte in introduced in the channel, the flux quickly reaches a steady state. This steady state is the one simulated in the previous section by setting $c = 0$ at the sensor surface, because the surface is far from being saturated. The steady-state flux in the case of $H = 20\,\mu\text{m}$ is the same as the one derived in the perfect collection case, namely $J = 7.1 \times 10^{-10} \text{mol}\,\text{m}^{-2}\,\text{s}^{-1}$. As the upstream surface of the channel saturates, the depletion boundary layer moves downstream. This increases the flux into the sensor, which quickly rises from its steady state value. Once all the receptors on the the sensor surface are bound, the flux drops quickly to a value of 0. The surface concentration of the bound analyte is found by integrating the flux as a function of time, and it is displayed in the same figure.

Since the Damköhler number is large, we found agreement between the Langmuir kinetics simulations and perfect collection cases.

5.3.9 Transport to resonator if rest of channel passivated

In this section we investigate the flux to the sensor in the case that only the resonator adsorbs the molecules of interest. Since the depletion zone begins the edge of the resonator, the flux at

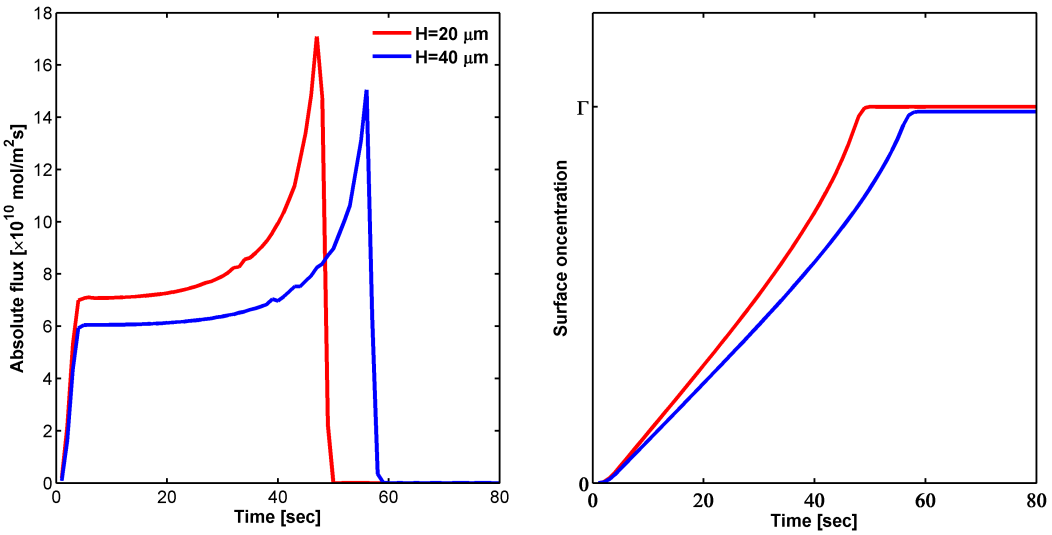

Figure 5.18: Time evolution of the flux and surface concentration in a simple channel with $H = 40\,\mu\text{m}$.

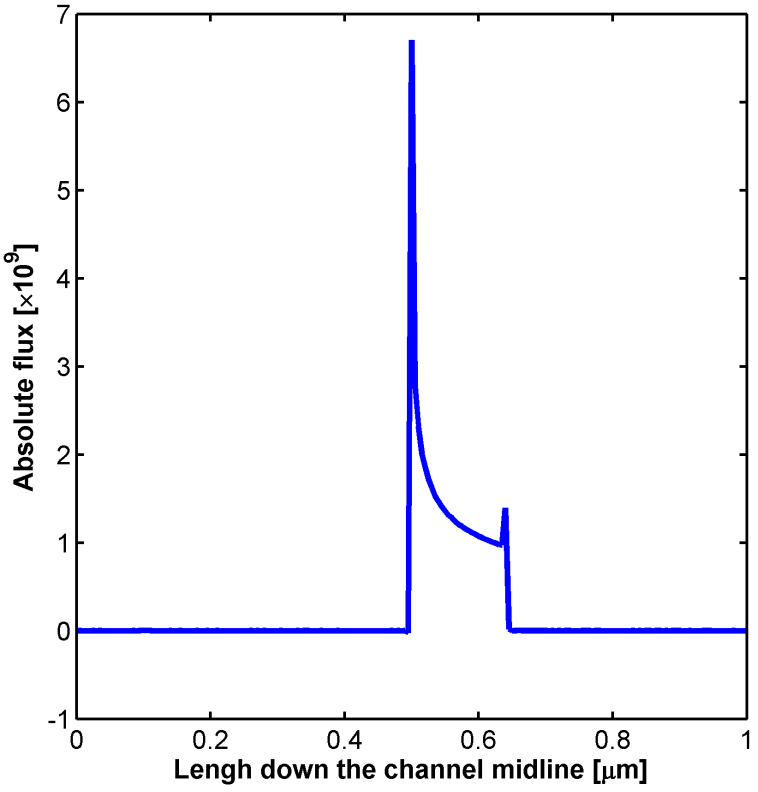

Figure 5.19: Steady state flux if only the resonator is passivated in $H = 40\,\mu\text{m}$.

the leading edge of the resonator is very large. Leyden *et al.* demonstrated that blocking the binding sites upstream of a FET biosensor increased the flux to the surface by a factor of 2.5, with a theoretical upper bound of 8.3 [13]. Indeed, this strategy is very promising, and we have explored chemical studies for passivation in Chapter 4. Figure 5.19 shows the flux to the resonator in the case that the rest of the channel is passivated. The leading edge of the resonator experiences the largest flux increase, and the trailing edge experiences a smaller increase. We propose that the herringbone would also increase the flux in this scenario.

5.3.10 Conclusions

We have shown that a herringbone structure has an enhanced effect on the mass transport to a point on the opposite channel surface. We have consistently obtained enhancement factors of around 5 for two- and four-groove geometries with Bezier shapes. Unfortunately, integrating the flux enhancement over the entire sensor surface leads to reduced enhancement factors. However, our conclusions can be applied with higher success to other biosensing platforms that have smaller sensors, either nanowires or photonic crystals, in which the wire or defect is on the nanometer size range.

Bibliography

[1] T. M. Squires, R. J. Messinger, and S. R. Manalis, "Making it stick: convection, reaction and diffusion in surface-based biosensors," *Nature biotechnology*, vol. 26, no. 4, pp. 417–426, 2008.

[2] A. D. Stroock, S. K. Dertinger, G. M. Whitesides, and A. Ajdari, "Patterning flows using grooved surfaces," *Analytical Chemistry*, vol. 74, no. 20, pp. 5306–5312, 2002.

[3] A. D. Stroock, S. K. Dertinger, A. Ajdari, I. Mezić, H. A. Stone, and G. M. Whitesides, "Chaotic mixer for microchannels," *Science*, vol. 295, no. 5555, pp. 647–651, 2002.

[4] A. D. Stroock and G. J. McGraw, "Investigation of the staggered herringbone mixer with a simple analytical model," *Philosophical Transactions of the Royal Society of London. Series A: Mathematical, Physical and Engineering Sciences*, vol. 362, no. 1818, pp. 971–986, 2004.

[5] J. O. Foley, A. Mashadi-Hossein, E. Fu, B. A. Finlayson, and P. Yager, "Experimental and model investigation of the time-dependent 2-dimensional distribution of binding in a herringbone microchannel," *Lab on a Chip*, vol. 8, no. 4, pp. 557–564, 2008.

[6] H.-Y. Lee and J. Voldman, "Optimizing micromixer design for enhancing dielectrophoretic microconcentrator performance," *Analytical chemistry*, vol. 79, no. 5, pp. 1833–1839, 2007.

[7] N. S. Lynn, J.-I. Martínez-López, M. Bocková, P. Adam, V. Coello, H. R. Siller, and J. Homola, "Biosensing enhancement using passive mixing structures for microarray-based sensors," *Biosensors and Bioelectronics*, vol. 54, pp. 506–514, 2014.

[8] A. L. Washburn, L. C. Gunn, and R. C. Bailey, "Label-free quantitation of a cancer biomarker in complex media using silicon photonic microring resonators," *Analytical Chemistry*, vol. 81, no. 22, pp. 9499–9506, 2009.

[9] J. Kirtland, *Interfacial Mass Transfer In Microfluidic Systems: Existence And Persistence Of The Modified Graetz Behavior*. PhD thesis, Cornell Univesity, August 2010.

[10] T. Gervais and K. F. Jensen, "Mass transport and surface reactions in microfluidic systems," *Chemical engineering science*, vol. 61, no. 4, pp. 1102–1121, 2006.

[11] J. D. Kirtland, G. J. McGraw, and A. D. Stroock, "Mass transfer to reactive boundaries from steady three-dimensional flows in microchannels," *Physics of Fluids (1994-present)*, vol. 18, no. 7, p. 073602, 2006.

[12] J. D. Kirtland, C. R. Siegel, and A. D. Stroock, "Interfacial mass transport in steady three-dimensional flows in microchannels," *New Journal of Physics*, vol. 11, no. 7, p. 075028, 2009.

[13] M. R. Leyden, R. J. Messinger, C. Schuman, T. Sharf, V. T. Remcho, T. M. Squires, and E. D. Minot, "Increasing the detection speed of an all-electronic real-time biosensor," *Lab Chip*, vol. 12, pp. 954–959, 2012.

Chapter 6

Conclusions and future directions

Ring resonator sensors show great potential for integration into multiplexed, rapid and robust platforms. This thesis has shown the benefits of a dual laminar flow platform consisting of a sensing and reference resonator for reducing environmental noises. The close spacing of the two resonators leads to minimal fabrication variations between the two sensors that results in their similar sensitivities to target analyte concentrations and to noise sources. We have characterized the response of the resonators through simulations and experiments, and demonstrated that their differential signal is insensitive to external perturbations.

By employing flow switching schemes that reduce the dead volume within the fluidic system, the transient response time of the platform has been greatly reduced. Two microfludic designs that use PDMS elastomeric valves have been presented and tested, one tailored to bulk sensing experiments, and the other to surface binding assays. The bulk sensing platform contains on-chip valves, and has a response time of seconds. The second platform, tailored for surface binding assays, consists of two chips with different roles, and also shows excellent response time. To develop the binding assay platform, we explored different surface functionalization protocols, and determined optimal conditions for depositing a monolayer of a linker silane layer. We also explored chemistries aimed at achieving selective functionalization of the sensor surface, which would enable multiplexing and enhanced mass transport to the sensor.

The initial version of the microfluidic platform, which employed on-chip valves, exhibited long term drift that was attributed to PDMS elasticity. Pressure calibration experiments supported this hypothesis that, while PDMS is a material excellent for rapid prototyping, it deforms under the applied pressure of the fluid flow. For platforms with only one sensing resonator or with a reference resonator covered by a polymer layer, the pressure transients are significant, but unaccounted for. Other groups note the presence of the drifting baseline, with similar trends as the pressure drifts presented in Chapter 3. Washburn *et al.* observe a drifting baseline in a platform with covered

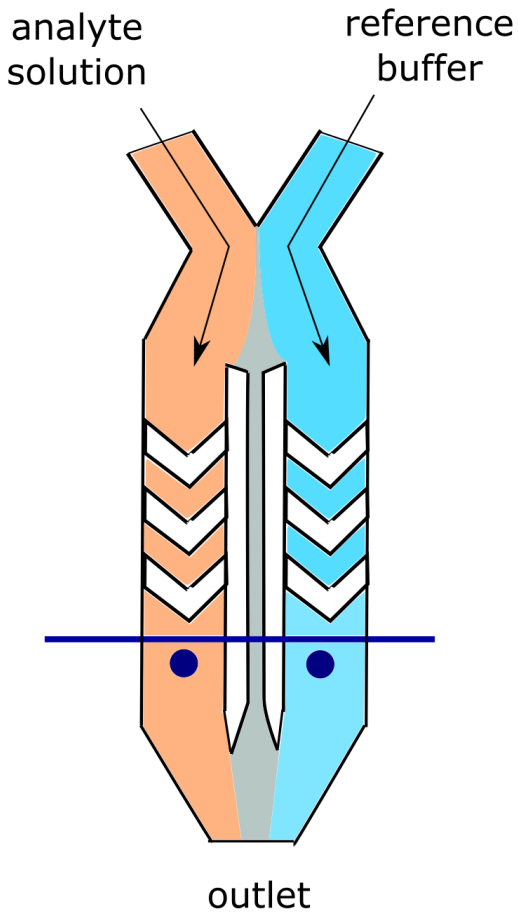

Figure 6.1: A dual laminar flow platform with herringbone grooves for enhanced mass transport to the sensors.

reference resonators. The drift initially exhibits a linear slope after the flow switch that decreases over time [1]. A dual laminar-flow platform in which a reference resonator was immersed in a reference fluid within the same laminar flow as the sensing resonator greatly reduced these transients.

Chapter 5 investigated the enhancement in mass transport to the sensing resonator due to a grooved herringbone structure at the top of the microfluidic channel. Figure 6.1 shows a design that integrates the herringbone structure into the dual laminar flow platform. If a dual herringbone structure were implemented in a single flow channel, it would increase lateral mixing between the co-laminar streams, in addition to enhancing the transverse fluid velocity into the bottom surface of the channel. To prevent the contamination of the streams by mixing, the two grooved channels encapsulating the resonators must be separated by a wall. To achieve pressure and temperature equilibration, we employ a stream contact zone of optimized length upstream of the herringbone-

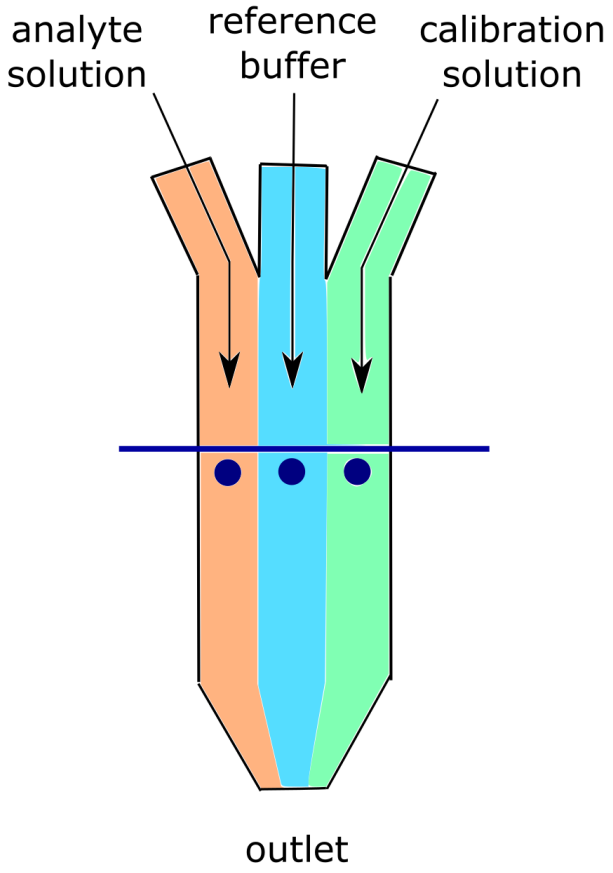

Figure 6.2: A laminar flow plaform with three streams flowing side-by-side to the sensing, reference and calibration resonators.

patterned portion of the channels. The temperature and pressure of the two streams containing the analyte and reference buffer equilibrate as they traverse this contact zone. The small diffusion zone that forms in this contact region would be mixed with the primary sample and reference flows if fluid within that zone were allowed to flow through either of the primary flow channels. This cross-contamination between the two streams is eliminated through a narrow microfluidic channel that bypasses the resonator channels directly to the outlet zone.

A possible extension of the laminar flow platform is to introduce a third resonator into the common microfluidic channel shared by the sensing and reference resonators (see Figure 6.2). The new resonator will be exposed to a third co-laminar fluid stream with a known concentration of solute, thereby serving as a calibration device. Performing the calibration step simultaneously to the measurement step would further reduce sensing times and enhance pressure and temperature noise reduction.

The microfluidic control system used in the experiments consists of bulky pressure controllers, electrical control boxes and tubing lines. To achieve device portability, we suggest the use of on-chip flow control systems. Begolo *et al.* describe an equipment-free pumping device that can be used to generate co-laminar flows without the need for bulky microfluidic controllers [2]. They demonstrate the laminar flow of three parallel streams with stability of 2.75 h. In addition, this platform is compatible with herringbone grooves, since they are passive structures which do not require active pressure control.

This thesis developed an optofluidic ring resonator platform and demonstrated its benefits for robust and rapid sensing. Future applications of this biosensor platform involve surface detection of biomolecular interactions for diagnostic applications of interest. The desired chemistries will initially be tested using the two-chip platform presented in Chapter 3. In subsequent experiments the laminar flow platform can be multiplexed using multiple microfluidic channels and a single reference flow. A laser scanning each pair of resonators needs to be developed to allow multiplexed interrogation. Furthermore, depending on the analyte, the reference resonator could be employed to eliminate bulk sensing effects by employing a reference flow with a similar index of refraction as the sensing flow.

Bibliography

[1] A. L. Washburn, L. C. Gunn, and R. C. Bailey, "Label-free quantitation of a cancer biomarker in complex media using silicon photonic microring resonators," *Analytical Chemistry*, vol. 81, no. 22, pp. 9499–9506, 2009.

[2] S. Begolo, D. V. Zhukov, D. A. Selck, L. Li, and R. F. Ismagilov, "The pumping lid: investigating multi-material 3D printing for equipment-free, programmable generation of positive and negative pressures for microfluidic applications," *Lab Chip*, vol. 14, pp. 4616–4628, 2014.

Appendices

.1 PDMS Fabrication Protocol

.1.1 Control Chip Protocol

1. Devices are made from Sylgard 184 (Dow Corning/Ellensworth). There are two parts: the oligomer mixture and the cross-linking agent, which are mixed together.

2. **Control Layer**

   - Pour 30 g Part A: 6 g Part B for a 5:1 ratio in a plastic cup. Spin in a HM-501 hybrid mixer (Keyence, Long Beach, CA), with settings: 2 min mixing, 2 min defoaming.
   - Line a Petri dish with Al foil and flatten, making sure there are no tears in the foil (PDMS could leak in and the mold would be hard to remove). Place the SU-8 master on the foil.
   - Put the control mold in a plastic container with a few drops of chlorotrimethylsilane, 98% (Alfa Aesar) for 5 min. This step creates a hydrophobic surface of the SU-8 master and prevents the PDMS from sticking to the mold when released.
   - Pour the 30 g of mixed PDMS on the SU8 control layer master, and place is a vacuum desiccator chamber, for 30 min. In the beginning, many bubbles will form, so vent the chamber to remove them and prevent the PDMS from spilling over.

3. **Flow Layer**

   - When there are no more visible bubbles in the control layer PDMS, start preparing the flow layer. Pour 20 g Part A: 1 g Part B for a 20:1 ratio in a vial. Mix/defoam 2 min/2 min. Line Petri dish with Al foil, put SU-8 Master in it, after 10 min of chlorotrimethylsilane.
   - PDMS mixture is spun using a programmable spin coater SCS P6700 (Speciality Coating Systems Inc) at 2200 rpm.

4. Both control and flow layers are put in an 80 °C oven at the same time. Ensure that both masters are flat.

5. **Bonding and Alignment**

   - After 35-40 min, both layers are removed from the oven. This time is very important, because the layers need to be partially cured, so that they can be easily handled, but not completely cured so that interlayer diffusion will promote the bonding. The control layer is peeled off the SU-8 master and diced.
   - Using a stereomicroscope, the control layer is aligned over the flow layer such that the valves are aligned, and the overhang is $> 10\,\mu m$.

The chips are placed in the oven at 80 °C overnight. The bonded control and flow layers are removed from the oven and holes are punched using a Schmidt Manual Press using a 21 Gauge TiN puncher and a ejector pin (Syneoco,Texas)

.2 PDMS/Glass Oxygen Plasma Bonding

.2.1 Bonding

1. The plasma machine used is AutoGlow (Glow Research, AZ).

2. **Pre-conditioning the plasma chamber**

   - With a TexWipe containing IPA clean the walls of the chamber.
   - Run the default machine cleaning step for 10 min: 100 W RF Power and 0.2 sccp O_2. Initially the plasma has a pinkish color due to the presence of N_2, but then turns blue when only O_2 is present.

3. **Glass Preparation**

   - The glass slides are 3"x2". They are first cleaned in IPA, sonicated for 30 min. The Glass is then baked in the oven for 1-2 hours to dry.
   - Both glass and PDMS are set in the plasma chamber. The program is set for 50 W for 30 s, 0.2 sccp O_2.

4. **Bonding**

   - After the plasma treatment, the glass and PDMS are put into contact.

   The chips are placed in the oven at 80 °C overnight to further stabilize the bond. Chips bonded this way should withstand pressures of 30 psi.